

# Implementation of Compliant Motion Control Schemes on the Stewart Platform

Hybrid Position/Force Control and  
Position-based Impedance Control

Semester Thesis

an der Fakultät für Maschinenwesen der Technischen Universität München

**Betreut von** Univ.-Prof. dr.ir. Daniel J. Rixen  
Christina Insam, M.Sc.  
Chair of Applied Mechanics

**Eingereicht von** Jessica Peters  
Denninger Straße 96  
81925 München

**Eingereicht am** Garching, den 18. März 2019



## **Abstract**

Compliant motion control encompasses all control schemes that deal with tasks in which a robot interacts with its environment and pure motion control cannot guarantee a safe and robust behavior of the manipulator. Investigations on improving prosthetic feet with the help of Real-time Substructuring have arisen the need for compliant motion control for the Stewart platform at the Chair of Applied Mechanics at the Technical University of Munich. In the context of this thesis, a general overview of compliant motion control schemes most commonly found in literature is given and a hybrid position/force control as well as a position-based impedance control scheme are designed, implemented, tested, validated and compared on the Chair's Stewart Platform. The investigations show that position-based impedance control is especially suitable for control tasks which require compliant movement within a specified region of attraction because it controls the admittance behavior of the robot-environment interaction. While hybrid position/force control exhibits larger computational costs for parallel robots, it offers the ability to prescribe specific contact force/torque values. The findings gathered within this work can be further studied and applied on the Real-time Substructuring approach as well as on any tasks that require compliant motion control on the Chair's Stewart platform.

## **Zusammenfassung**

Unter dem englischen Begriff „compliant motion control“, zu Deutsch „nachgiebige Bewegungsregelung“, werden alle Regelungskonzepte zusammengefasst, welche zur Interaktion zwischen einem Roboter und seiner Umgebung eingesetzt werden, wenn eine klassische Bewegungsregelung kein sicheres und robustes Verhalten des Manipulators garantieren kann. Untersuchungen zur Verbesserung von prothetischen Füßen mithilfe der Real-time Substructuring Methode erfordern eine nachgiebige Bewegungsregelung am Hexapod des Lehrstuhls für Angewandte Mechanik an der Technischen Universität München. Diese Arbeit gibt einen allgemeinen Überblick über die in der Literatur häufig vorzufindenden Reglerformen der nachgiebigen Bewegungsregelung und es werden Konzepte für die hybride Kraft-/Positionsregelung sowie positionsbasierte Impedanzregelung am Hexapod des Lehrstuhls entwickelt, implementiert, getestet, validiert und verglichen. Es zeigt sich, dass sich die positionsbasierte Impedanzregelung insbesondere für nachgiebige Bewegungsaufgaben innerhalb eines vorgegebenen Einzugsgebietes eignet. Während die hybride Kraft-/Positionsregelung bei parallelen Robotern größere Rechenkosten hervorruft, ermöglicht sie es, dem System gezielt gewünschte Kontaktkräfte und -momente aufzuzwingen. Die Ergebnisse dieser Arbeit dienen als Grundlage weiterer Untersuchungen und können für die Real-time Substructuring Methode sowie für sämtliche Aufgaben, die eine nachgiebige Bewegungsregelung erfordern, am Hexapod des Lehrstuhls angewandt werden.



# Contents

<b>List of Figures</b>	<b>2</b>
<b>List of Tables</b>	<b>3</b>
<b>List of Symbols</b>	<b>5</b>
<b>1 Introduction</b>	<b>9</b>
1.1 Motivation and Aim of the Thesis . . . . .	9
1.2 Outline of the Thesis . . . . .	9
<b>2 State of the Art and State of Research</b>	<b>11</b>
2.1 Characteristics and Kinematics of a Stewart Platform . . . . .	11
2.2 Concepts of Robot-Environment Interaction Control . . . . .	12
2.2.1 Overview of Different Approaches . . . . .	12
2.2.2 Independent Joint Control of Manipulators . . . . .	19
2.2.3 Hybrid Position/Force Control of Manipulators . . . . .	20
2.2.4 Position-based Impedance Control of Manipulators . . . . .	22
2.3 System Structure and Functionalities of the Chair's Stewart Platform . . . . .	23
2.3.1 System Components . . . . .	23
2.3.2 Implemented Functionalities . . . . .	24
<b>3 Realization of Compliant Motion Control Schemes on the Stewart Platform</b>	<b>29</b>
3.1 Extension of the Experimental Setup . . . . .	29
3.2 Data Processing of the Force/Torque Sensor Signals . . . . .	30
3.3 Realization of Hybrid Position/Force Control . . . . .	34
3.4 Realization of Position-based Impedance Control . . . . .	37
3.5 Design and Implementation of Test Cases . . . . .	40
<b>4 Design of Controller Parameters, Testing and Validation</b>	<b>45</b>
4.1 Preliminary Investigations . . . . .	46
4.2 Testing on Hybrid Position/Force Control . . . . .	48
4.2.1 Design of Hybrid Position/Force Controller Parameters . . . . .	48
4.2.2 Testing on Switch between Position and Force Control . . . . .	52
4.3 Testing on Position-based Impedance Control . . . . .	59
4.3.1 Design of Position-based Impedance Controller Parameters . . . . .	59
4.3.2 Approach for an Alternative Position-based Impedance Control . . . . .	69
4.4 Comparative Test Cases and Validation . . . . .	71
4.4.1 Testing on Behavioral Differences . . . . .	72
4.4.2 Testing on Computational Costs . . . . .	77
4.4.3 Validation of both Control Schemes . . . . .	78

<b>5</b>	<b>Comparison of Compliant Motion Control Schemes</b>	<b>85</b>
5.1	Theoretical Comparison . . . . .	85
5.2	Implementation and Computational Costs . . . . .	86
5.3	Differences in Behavior . . . . .	86
<b>6</b>	<b>Conclusion and Outlook</b>	<b>89</b>
6.1	Conclusion . . . . .	89
6.2	Outlook . . . . .	90
	<b>Bibliography</b>	<b>91</b>

## List of Figures

2.1	Overview of robot-environment interaction control strategies . . . . .	13
2.2	Definition of an impedance and an admittance . . . . .	15
2.3	Position-based indirect force control scheme . . . . .	17
2.4	Force-based indirect force control scheme . . . . .	17
2.5	Joint space control scheme . . . . .	18
2.6	Workspace control scheme . . . . .	19
2.7	Cascade control scheme . . . . .	20
2.8	Hybrid position/force control scheme . . . . .	21
2.9	Position-based impedance control scheme . . . . .	22
2.10	Stewart platform at the Chair of Applied Mechanics . . . . .	24
2.11	Detailed view of the representation of the robot's environment . . . . .	25
2.12	Implementation of an independent joint controller based on the single-joint model in the form of a PPI-cascade . . . . .	26
3.1	Extension of the experimental setup . . . . .	30
3.2	Data processing steps . . . . .	30
3.3	Sensor and workspace coordinate frames . . . . .	31
3.4	Ignoring force values close to 0 . . . . .	33
3.5	Realization of a hybrid position/force controller on the Stewart platform . . . . .	34
3.6	Integration of hybrid position/force control onto the Stewart platform . . . . .	36
3.7	Realization and integration of position-based impedance control . . . . .	37
3.8	Interpretation of position-based impedance control . . . . .	38
3.9	Target position and force trajectories withing the test trajectory test case . . . . .	43
3.10	State chart of the test trajectory . . . . .	44
4.1	Measured force $F_z$ using the moving average approach with a window length equal to 3 . . . . .	47
4.2	Comparison of step responses applying independent joint control and hybrid position/force control in a non-contact task when varying $K_{p,p}$ . . . . .	51
4.3	Comparison of step responses applying independent joint control and hybrid position/force control in a contact task when varying $K_{p,F}$ . . . . .	53
4.4	Comparison of step responses applying independent joint control and hybrid position/force control when switching from a non-contact task to a contact task . . . . .	56
4.5	Comparison of step responses applying independent joint control and hybrid position/force control when switching from a contact task to a non-contact task . . . . .	57
4.6	Comparison of step responses for different values $K$ when applying position-based impedance control for $M = 1 \text{ kg (kg} \cdot \text{m}^2)$ and varying $D$ . . . . .	63
4.7	Comparison of step responses for different values $K$ when applying position-based impedance control for $D = 10 \frac{\text{N}\cdot\text{s}}{\text{m}}$ ( $\text{Nm} \cdot \text{s}$ ) and varying $M$ . . . . .	64
4.8	Comparison of step responses for different values $K$ when applying position-based impedance control for $D = 100 \frac{\text{N}\cdot\text{s}}{\text{m}}$ ( $\text{Nm} \cdot \text{s}$ ) and varying $M$ . . . . .	66

4.9	Comparison of step responses for different values $K$ when applying position-based impedance control for $D = 1000 \frac{\text{N}\cdot\text{s}}{\text{m}}$ (Nm · s) and varying $M$ . . . . .	67
4.10	Variation of pole placement in the target admittance behavior . . . . .	68
4.11	Variation of the parameter $K_{p,p}$ in independent joint control . . . . .	70
4.12	Comparison of step responses when applying the approach for an alternative position-based impedance control . . . . .	71
4.13	Comparison of independent joint control, position-based impedance control and hybrid position/force control regarding their step responses . . . . .	74
4.14	Comparison of independent joint control, position-based impedance control and hybrid position/force control regarding the test trajectory . . . . .	76
4.15	Comparison of independent joint control, position-based impedance control and hybrid position/force control regarding their turnaround time . . . . .	77
4.16	Measured forces $F_x$ and $F_z$ for increasing robot-environment interaction in $x$ -direction . . . . .	79
4.17	Comparison of independent joint control, position-based impedance control and hybrid position/force control regarding a Heaviside step function in $x$ -direction . . . . .	81
4.18	Comparison of independent joint control, position-based impedance control and hybrid position/force control regarding a Heaviside step function in $x$ - and $z$ -direction . . . . .	83



# List of Tables

- 4.1 Parameter values used during testing . . . . . 49
- 4.2 Control parameters of hybrid position/force control . . . . . 54
- 4.3 Control parameters of position-based impedance control . . . . . 69
  
- 5.1 Comparison of hybrid position/force control with position-based impedance control . . . . . 88



## List of Symbols

In general, bold letters represent vectors or matrices while normal letters represent scalars. Indexes in the lower right corner usually provide additional information. Indexes in the upper right corner commonly name the coordinate frame in which the variable is expressed. For derivatives with respect to time, the following notation is used:  $\dot{\square}$ .

### Minuscule

$b$	length of one of the Stewart platform's legs
$\mathbf{b}$	vector of the Stewart platform's leg lengths
$d$	disturbance signal
$f$	frequency
$\mathbf{f}$	mapping function
$k$	spring stiffness
$k_{\max}$	number of iterations in Newton's method
$n$	number of degrees of freedom (DOFs) or iteration step in Newton's method
$\mathbf{q}$	generalized coordinates
$s$	Laplace operator
$t$	time
$\mathbf{v}$	arbitrary variable
$x$	position of the TCP along the $x$ -axis or a general position value
$\mathbf{x}$	workspace coordinates, pose of the TCP expressed in the workspace coordinate frame
$d\mathbf{x}$	infinitesimal displacement of the TCP
$\Delta\mathbf{x}$	pose modification vector in the context of impedance and admittance control
$y$	position of the TCP along the $y$ -axis or arbitrary output variable
$z$	position of the TCP along the $z$ -axis or $z$ -transformation operator

**Majuscule**

$A$	amplitude
$C$	controller transfer function
$\mathbf{C}$	controller transfer function matrix
$\{C\}$	constraint frame
$D_i$	value on the diagonal of the damping matrix
$\mathbf{D}$	damping matrix
$F$	general force value
$F_x$	contact force at the TCP along the $x$ -axis
$F_y$	contact force at the TCP along the $y$ -axis
$F_z$	contact force at the TCP along the $z$ -axis
$\mathbf{F}$	vector of contact force and torque values, usually measured at the TCP and expressed in the workspace coordinate frame
$G$	general transfer function
$\mathbf{G}$	transfer function matrix
$\mathbf{I}$	identity matrix
$\mathbf{J}$	Jacobian matrix
$\{J\}$	joint space coordinate frame
$K$	coefficient of a P(I)-controller
$K_i$	value on the diagonal of the mass/inertia matrix
$\mathbf{K}$	stiffness matrix or matrix of coefficients of a P(I)-controller
$M_i$	value on the diagonal of the mass/inertia matrix
$M_x$	contact torque at the TCP about the $x$ -axis
$M_y$	contact torque at the TCP about the $y$ -axis
$M_z$	contact torque at the TCP about the $z$ -axis
$\mathbf{M}$	mass/inertia matrix
$P$	plant transfer function
$R$	radius
$\mathbf{R}$	rotation matrix
$\mathbf{S}$	compliance selection matrix
$\{S\}$	sensor coordinate frame
$T_s$	sample time
$V$	voltage value for the servomotor of one of the Stewart platform's legs
$\mathbf{V}$	vector of voltage values for the servomotors of the Stewart platform's legs
$dW$	infinitesimal mechanical work being exchanged between the manipulator and its environment
$\{W\}$	workspace coordinate frame
$X$	Laplace transform of $x$
$Y$	mechanical admittance
$Z$	mechanical impedance

**Small greek letters**

$\alpha$	rotation of the TCP about the $x$ -axis
$\beta$	rotation of the TCP about the $y$ -axis
$\gamma$	rotation of the TCP about the $z$ -axis
$\partial\bullet$	used for partial derivatives
$\epsilon$	approximation error in Newton's method
$\theta$	angle from sensor coordinate frame to workspace coordinate frame

**Indexes in lower right corner**

ad	admittance
approx	approximated
c	contact
contact	pose or force/torque vector for which the TCP is in contact with its environment
d	desired
e	error
end	end pose or force/torque vector of the target trajectory of the TCP
E	environment
forward	used to specify the mapping function in the context of forward kinematics
$F$	refers to force variable $F$
$\mathbf{F}$	force
$\mathbf{F}, \Delta \mathbf{x}$	used to specify that $\mathbf{F}$ is computed from $\Delta \mathbf{x}$ in the context of a transfer function matrix
i	inner
inverse	used to specify the mapping function in the context of inverse kinematics
I	integral (in the context of a PI-controller)
max	maximum
$n$	iteration step in Newton's method
o	outer
p	position
P	proportional (in the context of a P(I)-controller)
raw	indicates that the corresponding variable has not been modified
r	reference
safe	indicates that the corresponding variable has been modified by the safety functions module
start	start pose or force/torque vector of the target trajectory of the TCP
tol	tolerance, refers to the user-defined limit for the approximation error in Newton's method
v	velocity
$x$	refers to position variable $x$
$\mathbf{x}$	refers to the TCP's pose
$\Delta \mathbf{x}, \mathbf{F}$	used to specify that $\Delta \mathbf{x}$ is computed from $\mathbf{F}$ in the context of a transfer function matrix
$z$	refers to position variable $z$
0	to indicate the initial guess in Newton's method
1...	numbering of variables

**Indexes in upper right corner**

(C)	constraint frame
(J)	joint space coordinate frame
(S)	sensor coordinate frame
(W)	workspace coordinate frame
-1	inverse
T	transpose

**Abbreviations**

**DOF** degree of freedom

<b>DSP</b>	Digital Signal Processor
<b>FIR</b>	finite impulse response
<b>OS</b>	operating system
<b>RTS</b>	Real-time Substructuring
<b>SISO</b>	single-input single-output
<b>TCP</b>	tool center point
<b>UML</b>	Unified Modeling Language

# Chapter 1

## Introduction

### 1.1 Motivation and Aim of the Thesis

The most common way of controlling a manipulator is by pure motion control. There are multiple industrial applications for which this is an adequate approach, such as pick-and-place or spray painting. However, many control tasks require interaction of the robot with its environment. Typical examples are grinding, polishing and blending. In recent years, more and more medical robot applications, e.g. spine surgery and knee and hip joints replacement have gained in importance. [17] For all these tasks, pure motion control is not satisfying because already small inaccuracies in position control due to modeling errors may cause large contact forces, especially when dealing with rigid environments. Thus, especially in crucial situations, such as human-robot interaction or medical applications, force control is mandatory to guarantee a safe and robust behavior of the manipulator. [24, Chap. 9] We call the class of control methods dealing with tasks where a manipulator interacts with its environment *compliant motion control* [16]. Current research topics at the Chair of Applied Mechanics, in particular Christina Insam's investigations on improving prosthetic feet with the help of Real-time Substructuring (RTS) [11], have arisen the need for compliant motion control for the Chair's Stewart platform. A Stewart platform is a parallel robot which benefits from high rigidity and high positioning accuracy compared to serial robots because of its parallel structure. It is commonly applied for flight and driving simulators as well as high speed positioning tasks, but more recently also for medical applications [23, 24, Chap. 18]. Most scientific papers covering compliant motion control examine serial robots. However, parallel robots have to be treated differently, mainly because of differences concerning their kinematics. Besides, the Chair's Stewart platform is solely controlled by a pure motion controller at the moment. Thus, the aim of this thesis is to design control schemes for two representatives of compliant motion control, namely hybrid position/force control and an impedance control approach. In this regard, an appropriate impedance control scheme shall be chosen and both control schemes shall be implemented, tested, validated and compared on the existing Stewart platform. Overall, this thesis focuses on the control aspects rather than the kinematics and dynamics of the Stewart platform. Furthermore, it is meant to be an experimental approach to compliant motion. Thus, most results are based on experiments rather than theoretical derivations.

### 1.2 Outline of the Thesis

The thesis firstly wants its readers to become acquainted with some basic principles regarding the Stewart platform as well as manipulator control, summed up in chapter 2, *State of the Art*

*and State of Research.* It begins with a short description of a Stewart platform and its major characteristics. Furthermore, the chapter introduces the terms workspace and joint space coordinates as well as forward and inverse kinematics and defines them in particular for a Stewart platform. Besides, it gives a literature review of robot-environment interaction control and explains independent joint control, hybrid position/force control and position-based impedance control of manipulators more in detail. Finally, it presents the Stewart platform of the Chair of Applied Mechanics, describes its components and reveals its functionalities and implementations.

With this knowledge, we develop a concept to realize each hybrid position/force control and an impedance control scheme on the Stewart platform in chapter 3, *Realization of Compliant Motion Control Schemes on the Stewart Platform.* We extend the existing experimental setup and come up with required sensor data processing steps. Thereafter, we realize hybrid position/force control on the Stewart platform. Besides, we choose position-based impedance control within all impedance control approaches and also realize it on the Stewart platform. Additionally, we come up with a mechanical interpretation of position-based impedance control. Finally, we design two test cases suitable for testing, validation and comparison of the control schemes: step response analysis and a concrete test trajectory.

Next, in chapter 4, *Design of Controller Parameters, Testing and Validation,* we at first ensure that functionalities which directly influence the performance of control work accurate enough in order to not distort the later testing results. We begin with testing on hybrid position/force control. We tune its control parameters and investigate its performance for a particular problem. With the help of multiple tests, we thereafter determine suitable control parameters for position-based impedance control by applying two complementary approaches. We also explore the influence of different control parameter values on the system behavior. Finally, we run tests which compare the realizations of hybrid position/force control and position-based impedance control due to their different influences on the system behavior as well as their computational costs. Moreover, we validate both control schemes with the help of a control task which is not used during testing.

All results of the former chapters are discussed in chapter 5, *Comparison of Compliant Motion Control Schemes,* with focus on the comparison between hybrid position/force control and position-based impedance control in terms of their characteristics, implementation and computational costs as well as their influence on the system behavior.

Chapter 6, *Conclusion and Outlook,* completes the thesis with a short conclusion and an outlook to possible future investigations in the context of compliant motion control on the Stewart platform.



## Chapter 2

### State of the Art and State of Research

The following chapter gives a brief description of some fundamental prerequisites which are the basis for the concepts developed in the context of this thesis. Firstly, section 2.1 deals with the characteristics and kinematics of a Stewart platform in general. Secondly, section 2.2 gives an overview of common approaches to robot-environment interaction control and explains the ones that will be further discussed in chapter 3 more in detail. Finally, section 2.3 presents the existing Stewart platform that I have been working on during the last six months.

#### 2.1 Characteristics and Kinematics of a Stewart Platform

A Stewart platform, also known as Gough-Stewart-Platform, is a parallel robot which consists of a usually fixed base platform and an upper platform, both connected by six legs via rotational joints. The legs' lengths can be modified in order to move the upper platform along the robot's three translational and three rotational degrees of freedom (DOFs). [23]

Because of their parallel structure, Stewart platforms benefit from high rigidity and thereby high positioning accuracy. As forces are uniformly distributed on their six legs, their components can be constructed rather thin and thus the ratio of the mass of payload over the mass of the robot is much larger than for serial manipulators. However, their workspace is usually small compared to the one of a serial robot. Their industrial use ranges from flight and driving simulators as well as high speed positioning tasks to land-based telescopes and medical applications. [23, 24, Chap. 18]

When describing the kinematics of a robot, we distinguish between two different types of coordinate representations: *workspace* and *joint space coordinates*. For a Stewart platform, workspace coordinates  $\mathbf{x}$  are equal to the robot's generalized coordinates  $\mathbf{q}$  and characterize the pose, i.e. the position and orientation, of its tool center point (TCP) in Cartesian space [23, 26]:

$$\mathbf{x} = \mathbf{q} = \begin{pmatrix} x \\ y \\ z \\ \alpha \\ \beta \\ \gamma \end{pmatrix}. \quad (2.1)$$

Angles  $\alpha$ ,  $\beta$  and  $\gamma$  characterize rotation of the TCP about its  $x$ -,  $y$ - and  $z$ -axis. Usually, the TCP is located at the center of the top side of the upper platform. In the following, if no other

coordinate frame is specified, the vector  $\mathbf{x}$  generally represents the pose of the TCP expressed in the workspace coordinate frame as presented in eq. (2.1).

On the other hand, joint space coordinates  $\mathbf{b}$  define each of the Stewart platform's six leg lengths [23, 26]:

$$\mathbf{b} = \begin{pmatrix} b_1 \\ b_2 \\ b_3 \\ b_4 \\ b_5 \\ b_6 \end{pmatrix}. \quad (2.2)$$

To change between joint space and workspace representation, we apply *forward and inverse kinematics*. Forward kinematics generally describes a mapping from joint space to workspace coordinates. In case of a Stewart platform, the corresponding task is to determine the pose of the TCP  $\mathbf{x}$  for a given vector of leg lengths  $\mathbf{b}$  [24, Chap. 18]:

$$\mathbf{x} = \mathbf{f}_{\text{forward}}(\mathbf{b}). \quad (2.3)$$

In contrast to serial robots, analytically solving forward kinematics for parallel manipulators usually leads to ambiguous solutions. Thus, it is common practice to apply numerical approaches instead, such as *Newton's method*. [23]

The opposite is true for inverse kinematics. For parallel robots, it can be analytically solved using kinematic relationships while the solution for serial robots is based on numerical methods. In general, inverse kinematics map workspace coordinates on joint space. Correspondingly for a Stewart platform, it expresses how to compute the robot's leg lengths  $\mathbf{b}$  for a given pose of its TCP  $\mathbf{x}$  [24, Chap. 18]:

$$\mathbf{b} = \mathbf{f}_{\text{inverse}}(\mathbf{x}). \quad (2.4)$$

Joint space and workspace velocity correlate with each other through the Jacobian  $\mathbf{J}$ . The matrix is defined by the Stewart platform's geometry [23, 26]:

$$\dot{\mathbf{b}} = \mathbf{J}\dot{\mathbf{x}}. \quad (2.5)$$

## 2.2 Concepts of Robot-Environment Interaction Control

The following sections present some commonly used approaches to robot-environment interaction control. Before section 2.2.2, section 2.2.3 and section 2.2.4 explain the control schemes applied in the context of this thesis in detail, section 2.2.1 gives a short overview of robot-environment interaction control in general to help better classify them in the whole set of existing control concepts. All aspects mentioned in the following sections are kept general in order to hold true for serial as well as for parallel manipulators.

### 2.2.1 Overview of Different Approaches to Robot-Environment Interaction Control

In literature, there exist many attempts to classify approaches to robot-environment interaction control. Examples can be found in [5], [17], [24, Chap. 9], [27] and [29]. The terminology used by different researchers is not uniform, neither is their classification. Figure 2.1 gives an overview of the most commonly used concepts of robot-environment interaction

control in a way that seems to be most suitable for helping understand the following chapters of the thesis. Thus, the diagram is a trade-off among the categorizations in [5], [17] and [24, Chap. 9] while it tries to stick to a nomenclature that is based on the very first definitions of the terms used. Often for simplicity, we use the term *force* to refer to *force and torque* and accordingly *position* represents *position and orientation*.

The following explanations concerning fig. 2.1 are based on [17] if not marked otherwise.

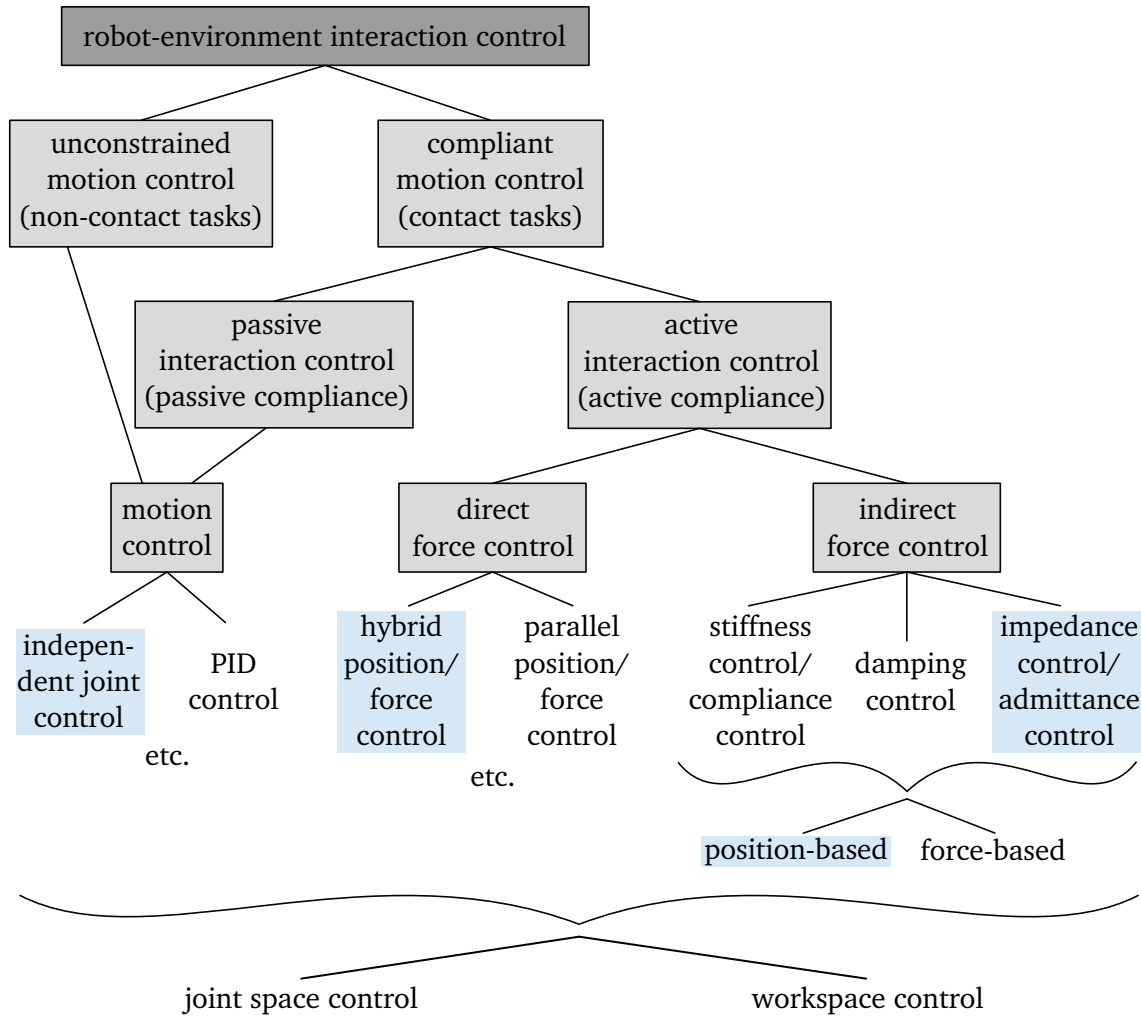


**Figure 2.1:** Overview of robot-environment interaction control strategies based on [5], [17] and [24, Chap. 9] (diagram inspired by [5])

### Unconstrained and Compliant Motion Control

The first possibility to categorize robot-environment interaction control is to distinguish between *contact tasks* and *non-contact tasks*. Non-contact tasks appear when the robot is not in contact with its environment and can move freely in space, such as in performing spray-painting. There, the manipulator's performance only depends on its own dynamics and is not influenced by the environment. In other words, the magnitude of the mechanical work being exchanged between the manipulator and its environment is zero because of non-existing interaction forces:  $dW = \mathbf{F} \cdot d\mathbf{x} = 0$  [8]. This type of control tasks is named *unconstrained motion control* and is accomplished by a pure motion controller. Some popular motion control concepts are *independent joint control*, *PID control*, *computed-torque control*, *tracking control*

schemes, such as *inverse dynamics control*, *feedback linearization* and *passivity-based control*, and some adaptive control and robust control schemes. These approaches are e.g. all explained in [24, Chap. 8].

In contrast, in contact tasks the interaction forces are unequal to zero ( $\mathbf{F} \neq \mathbf{0}$ ) as the environment sets constraints on the manipulator's motion. This circumstance is referred to as *compliant motion* [16] and requires *compliant motion control*.

### Compliant Motion Control: Passive and Active Interaction Control

Within compliant motion control, we also distinguish two classes. In *passive interaction control*, contact forces entirely adapt the trajectory of the TCP due to the inherent compliance of the robot, e.g. the compliance in the manipulator's structure or in the servos. So, apart from adjusting the robot's compliance to specific process requirements by usually attaching additional mechanical components to the TCP, interaction forces can be considered negligible ( $\mathbf{F} = \mathbf{0}$ ). This leads to negligible mechanical work  $dW = \mathbf{F} \cdot d\mathbf{x} = 0$  which allows the manipulator to be treated as an isolated system in terms of controller design, similar to the unconstrained motion control task [8]. Thus, a pure motion control method is used to handle the robot-environment interaction. Welding represents a practical industrial example of this kind of compliant motion control.

In *active interaction control*, interaction forces as well as exchanged mechanical work are generally not accepted to be negligible ( $\mathbf{F} \neq \mathbf{0}$ ,  $dW \neq 0$ ). Industrial applications for this case are for example drilling, reaming and grinding. As a result, a controller needs to actively regulate the compliance of the manipulator system by either directly controlling interaction forces applying *direct force control* or by shaping a desired compliant behavior utilizing *indirect force control*.

Compared to active interaction control, passive interaction control is faster, simpler and cheaper as there is no need for force/torque sensors and as the preprogrammed trajectory of the manipulator's TCP does not have to be adapted during execution. However, active interaction control is the more generalized approach, because it does not require additional compliant mechanical components individually designed for specific process requirements. Furthermore, it can better deal with deviations from the planned robot's trajectory. Above all, to a large extent, it can prevent critical interaction forces from occurring by measuring forces. Nevertheless, as it only reacts to the measured forces, it is better combined with a sort of passive compliance to completely keep interaction forces below an acceptable level. [24, Chap. 9]

### Active Interaction Control: Direct and Indirect Force Control

The main difference between direct and indirect force control is that in the former control strategy, both the robot's motion and the interaction forces between the manipulator and its environment are directly controlled to achieve a desired robot-environment interaction due to explicit closure of a force feedback loop, whereas in the latter concept, control of force or motion alone is considered inadequate. Thus, the relationship between interaction forces and motion of the robot is controlled to generate a desired compliant behavior. Popular representatives of direct force control are *hybrid position/force control* as well as *parallel position/force control*. These may be applied in industry for grinding and polishing.

### Indirect Force Control: Stiffness/Compliance Control, Damping Control and Impedance/Admittance Control

Indirect force control can further be subclassified into *stiffness control/compliance control*, *damping control* and *impedance control/admittance control*. In stiffness control and compliance control, only the static relationship between the contact forces and the displacement of the TCP's position from the desired position is taken into account. Note, that in this context, compliance describes the reciprocal of stiffness. In contrast, in damping control, the relationship between the contact forces and the linear and angular velocity of the TCP is used to shape a desired compliant behavior, whereas in impedance control and admittance control, the whole dynamic interaction between the manipulator and its environment is modified during control. So, stiffness/compliance control and damping control are special cases of impedance/admittance control. [5, 24, Chap. 9]

In literature, the terms impedance and admittance control are often used to describe the same control scheme. The analog trend appears relating to stiffness and compliance control [24, Chap. 9]. However, there is a clear difference between these concepts, which will be explained in the following paragraphs.

**Impedance and Admittance Control** A very first definition of the terms impedance and admittance can be found in [8]. The author makes use of the fact, that along each DOF, the product of two conjugate variables, that are called *effort* and *flow*, can describe the instantaneous power flow between any physical systems [19]. In case of robot-environment interaction, the manipulator itself and its environment each represent a physical system. They interact through contact forces as the effort variable and robot's velocity as the flow variable. In accordance with this consideration, an impedance is defined by accepting velocity as the input variable and responding with a force as the output variable. An admittance behaves the other way round. Figure 2.2 illustrates these relationships.

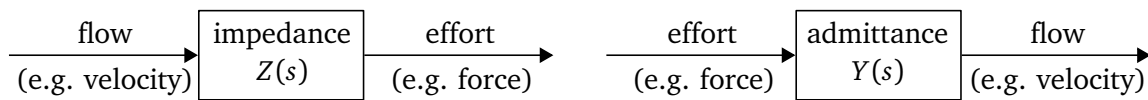


**Figure 2.2:** Definition of an impedance and an admittance according to [8]

The author of [8] emphasizes that effort and flow variables in robot-environment interaction may be linked in any arbitrary form. In this general case, the two concepts impedance and admittance are neither equivalent nor interchangeable representations of the system, i.e. it is not possible to simply convert one concept into the other one by inverting underlying equations. However, many researchers, for example [5] and [29], simplify the relation to a linear one. This leads to the following definition of an impedance in the Laplace domain:

$$Z(s) = \frac{F(s)}{\dot{X}(s)} = \frac{F(s)}{sX(s)}. \quad (2.6)$$

The same can be done for an admittance:

$$Y(s) = \frac{\dot{X}(s)}{F(s)} = \frac{sX(s)}{F(s)} = Z(s)^{-1}. \quad (2.7)$$

Herein, the Laplace transforms of the position variable  $x(t)$  and the robot's velocity  $\dot{x}(t)$  are denoted by  $X(s)$  and  $\dot{X}(s)$  respectively and the Laplace transform of the interaction force  $F(t)$  between the manipulator and its environment is  $F(s)$ . So, in the simple linear case, impedance is the inverse of admittance and vice versa.

This thesis focuses on the linear description of impedance and admittance. For more details on the theory, implementation and applications of the general concept, interested readers can have a look at [8], [9] and [10].

As the dynamics of a mass-spring-damper system is simple to understand, we can even go one step further and express the desired robot-environment interaction by a linear second-order differential equation of a  $n$ -dimensional mass-spring-damper system:

$$\mathbf{F} = \mathbf{M}(\ddot{\mathbf{x}} - \ddot{\mathbf{x}}_d) + \mathbf{D}(\dot{\mathbf{x}} - \dot{\mathbf{x}}_d) + \mathbf{K}(\mathbf{x} - \mathbf{x}_d) = \mathbf{M}\Delta\ddot{\mathbf{x}} + \mathbf{D}\Delta\dot{\mathbf{x}} + \mathbf{K}\Delta\mathbf{x}, \quad (2.8)$$

or in the Laplace-domain:

$$\mathbf{F}(s) = (\mathbf{M}s^2 + \mathbf{D}s + \mathbf{K})(\mathbf{X}(s) - \mathbf{X}_d(s)) = (\mathbf{M}s^2 + \mathbf{D}s + \mathbf{K})\Delta\mathbf{X}(s). \quad (2.9)$$

Herein, the manipulator's number of DOFs is denoted by  $n$ , the desired position trajectory corresponding to the equilibrium position of the mass-spring-damper system is  $\mathbf{x}_d$ , the actual position vector is referred to by  $\mathbf{x}$ , the position control error is  $\Delta\mathbf{x} = \mathbf{x} - \mathbf{x}_d$  and the vector of interaction forces is  $\mathbf{F}$ . By modifying the positive definite mass/inertia, damping and stiffness matrices  $\mathbf{M}$ ,  $\mathbf{D}$ ,  $\mathbf{K} \in \mathbb{R}^{n \times n}$ , we can shape any target impedance or admittance. The target robot impedance along all the  $n$  DOFs is described by:

$$\mathbf{Z}(s) = \mathbf{F}(s)(s\Delta\mathbf{X}(s))^{-1} = \frac{1}{s}(\mathbf{M}s^2 + \mathbf{D}s + \mathbf{K}). \quad (2.10)$$

Accordingly, for the target robot admittance, the following equation holds true:

$$\mathbf{Y}(s) = \mathbf{Z}(s)^{-1} = s\Delta\mathbf{X}(s)\mathbf{F}(s)^{-1} = s(\mathbf{M}s^2 + \mathbf{D}s + \mathbf{K})^{-1}. \quad (2.11)$$

Note, that the author of [17] defines the robot's impedance slightly differently. However, we want to stick to the definition from [8]. Often, also for simplicity, the mass-spring-damper system, describing the target impedance and admittance, is declared to be decoupled, which leads to diagonal matrices  $\mathbf{M}$ ,  $\mathbf{D}$  and  $\mathbf{K}$ .

**Stiffness/Compliance Control and Damping Control** As stiffness/compliance control and damping control are special cases of impedance/admittance control, we get the desired robot-environment interaction behavior for those control concepts by setting  $\mathbf{D} = \mathbf{0}$  for stiffness/compliance control,  $\mathbf{K} = \mathbf{0}$  for damping control and  $\mathbf{M} = \mathbf{0}$  for both of them.

Thus, eq. (2.8) turns to

$$\mathbf{F} = \mathbf{K}(\mathbf{x} - \mathbf{x}_d) = \mathbf{K}\Delta\mathbf{x} \quad (2.12)$$

for stiffness and compliance control and to

$$\mathbf{F} = \mathbf{D}(\dot{\mathbf{x}} - \dot{\mathbf{x}}_d) = \mathbf{D}\Delta\dot{\mathbf{x}} \quad (2.13)$$

for damping control.

Note, that the differentiation between stiffness and compliance control is equivalent to the one between impedance and admittance control.

### Indirect Force Control: Position- and Force-based Approaches

All the concepts of indirect force control that have been presented can also be categorized in *position-based* and *force-based* approaches [3, 12, 13]. Figure 2.3 and fig. 2.4 illustrate those two concepts. The aim of both control schemes is to fulfill a desired compliant behavior while following the target position trajectory  $\mathbf{x}_d$  during robot-environment interaction.

Position-based schemes are characterized by having an inner position control loop. The target compliant behavior is defined by the transfer function matrix  $\mathbf{G}_{\Delta\mathbf{x},\mathbf{F}}$ . It is used to compute a required modification in the TCP's position  $\Delta\mathbf{x}$  due to actual contact forces and torques  $\mathbf{F}$ . The resulting position modification signal is subtracted from the target position trajectory  $\mathbf{x}_d$  to receive a reference position trajectory  $\mathbf{x}_r$  as new input for the inner position control loop. The specific form of  $\mathbf{G}_{\Delta\mathbf{x},\mathbf{F}}$  depends on the type of indirect force control used.

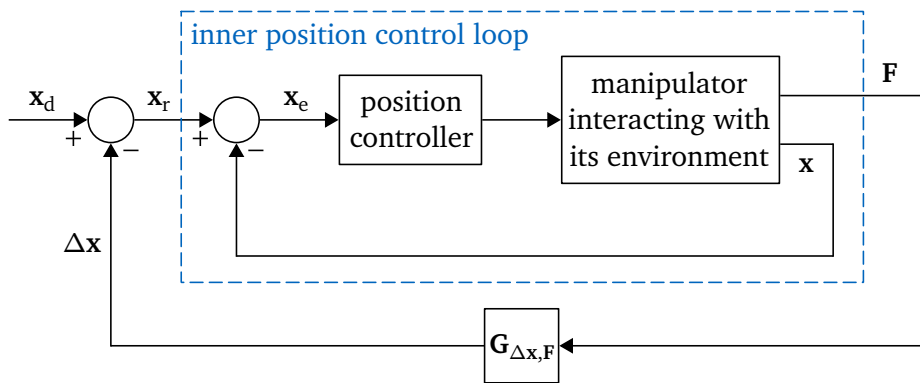


**Figure 2.3:** Position-based indirect force control scheme (figure inspired by [13])

In contrast, the inner control loop in a force-based control scheme is based on force control. A desired reference force  $\mathbf{F}_d$  is determined due to the derivation of the TCP's position  $\Delta\mathbf{x}$  from the desired trajectory  $\mathbf{x}_d$  and to satisfy the desired compliant behavior defined by a transfer function matrix  $\mathbf{G}_{\mathbf{F},\Delta\mathbf{x}}$ . This transfer function matrix is the inverse of  $\mathbf{G}_{\Delta\mathbf{x},\mathbf{F}}$  in the position-based scheme.

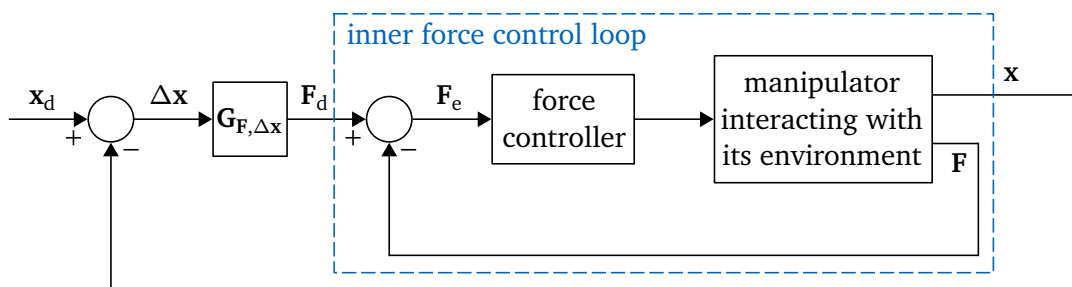


**Figure 2.4:** Force-based indirect force control scheme (figure inspired by [13])

For both approaches, the outer control loop usually takes place in workspace while the inner control loop can either be workspace or joint space control.

The definition displayed in fig. 2.2 inevitably leads to the fact that admittance control uses inner position control and outer force control as it only accepts forces as inputs and yields velocity as outputs. For impedance control, it is the other way round. [5] Thus, per definition,

admittance control schemes, as they have been presented here, can only be position-based concepts, whereas impedance control schemes are obligatory force-based. The same relation holds true for stiffness and compliance control schemes. Nevertheless, it is common practice to use the term *position-based impedance control*, if the transfer function matrix in fig. 2.3 is chosen to be

$$\mathbf{G}_{\Delta x, F}(s) = \frac{\mathbf{Y}(s)}{s} = (\mathbf{M}s^2 + \mathbf{D}s + \mathbf{K})^{-1} \quad (2.14)$$

and *force-based impedance control* for

$$\mathbf{G}_{F, \Delta x}(s) = s\mathbf{Z}(s) = \mathbf{M}s^2 + \mathbf{D}s + \mathbf{K} \quad (2.15)$$

in fig. 2.4. This thesis sticks to this naming convention. Additionally, section 2.2.4 explains position-based impedance control more in detail.

Because of the inner position control loop of the position-based approach, the control scheme reaches high accuracy in position. This is linked to a characteristically stiff behavior regarding the robot-environment interaction. Contrarily, the force-based approach can provide smaller impedance, stiffness and damping. Nevertheless, many industrial manipulators, which are controlled by any indirect force control scheme, are position-based to avoid modifications on the often implemented conventional position controller. The author of [12] investigates both schemes regarding stability boundaries. Overall, indirect force control becomes more and more important, especially for recent medical robot applications, such as neurosurgical and microsurgical operations as well as spine surgery. [17]

### Joint Space and Workspace Control

Another way of classification results from differentiating the coordinate representations used to specify a control scheme. On the one hand, control can take place in *joint space*, called *joint space control*. Figure 2.5 shows the characteristics of this control scheme for an arbitrary controlled variable  $\mathbf{v}$ , that might be for example position, velocity or force. Usually we can most easily provide the TCP's desired trajectory for the controlled variable  $\mathbf{v}_d^{(W)}$  in workspace, marked by the superscript (W). However, in this control concept, control and sensor measurements are performed in joint space. Thus, to get the desired variable  $\mathbf{v}_d^{(J)}$  in joint space, indicated by (J), we have to execute a coordinate transformation, e.g. inverse kinematics in case of position.

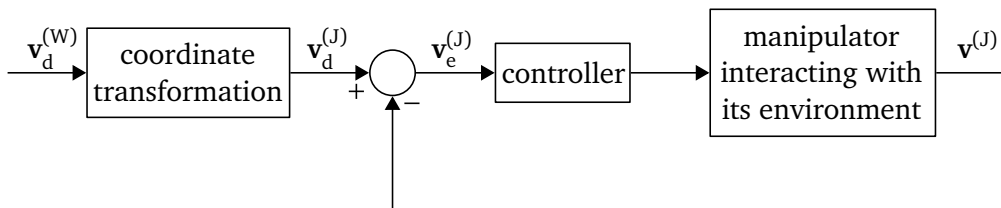


**Figure 2.5:** Joint space control scheme (figure inspired by [24, Chap. 8])

On the other hand, in *workspace control*, we can directly use the desired trajectory  $\mathbf{v}_d^{(W)}$  without any modifications, as the controller operates in workspace. Nevertheless, often the controlled variables can only be measured in joint space. This circumstance demands a coordinate transformation to calculate the measured variables in the workspace reference frame. For instance, in terms of position control this can be achieved by forward kinematics. Figure 2.6 illustrates this approach.



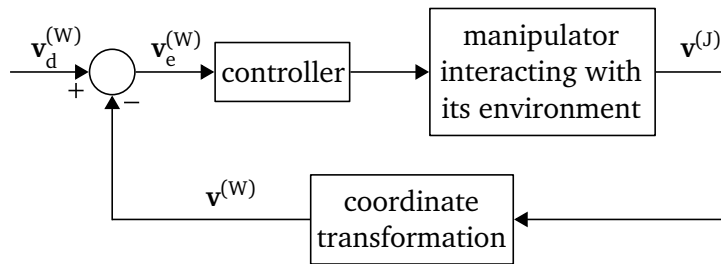


**Figure 2.6:** Workspace control scheme (figure inspired by [24, Chap. 8])

In principal, every control scheme discussed in fig. 2.1 can be implemented as workspace control as well as joint space control.

Section 2.2.1 only gives a brief overview of most commonly used approaches to robot-environment interaction control. Various researchers, such as of [5], [17], [24, Chap. 9], [27] and [29] present a more detailed classification or look at the topic from another point of view. Additionally, they give more examples and more insights in the advantages and drawbacks of the different control schemes. Moreover, they consider hybrid forms of the concepts mentioned and more advanced control schemes, such as *hybrid impedance control* [2] and *robot adaptive force control* (examples listed in [29]).

The following sections deal more in detail with the control concepts that are marked in blue in fig. 2.1. Furthermore, the advantages and drawbacks of hybrid position/force control and position-based impedance control are discussed in chapter 5.

## 2.2.2 Independent Joint Control of Manipulators

Due to its simple structure, an often implemented approach to motion control of manipulators is independent joint control. The following paragraph shortly summarizes the explanations given in [24, Chap. 8].

Independent joint control is a decentralized joint space control approach that is based on the assumption that each joint can be controlled separately. To make it even more simple, each joint axis can additionally be considered as a linear single-input single-output (SISO) system, also known as *single-joint model*, to receive a decentralized, decoupled, linear control concept. Coupling effects among joints are not considered within the dynamic model of the robot, but they are treated as disturbance input signals to make the model less complex. Often, a decoupled independent joint controller is implemented by designing a *PPI-cascade* for each joint. Figure 2.7 illustrates the general structure of a cascade control scheme according to [15]. It can be applied whenever it is possible to measure a second variable  $y_i$  in addition to the controlled variable  $y_o$  after splitting the plant into two parts  $P_1(s)$  and  $P_2(s)$ . This allows to construct a control structure that consists of two superimposing control loops. The inner control loop comprises the controller  $C_1(s)$  and the first part of the plant  $P_1(s)$ . It manipulates  $y_i$  based on the reference signal  $y_{i,d}$  which is computed by the second controller  $C_2(s)$  in the outer control loop. The outer control loop is responsible for controlling the plant's output  $y_o$  with reference to the desired signal  $y_{o,d}$ . Arbitrary disturbance signals  $d_1$  and  $d_2$  may appear. The inner control loop has to be stable by itself and faster than the outer one. Then, the cascade control scheme can manage to control the variable  $y_o$  quicker and more accurate than it would be feasible by using a conventional control scheme.

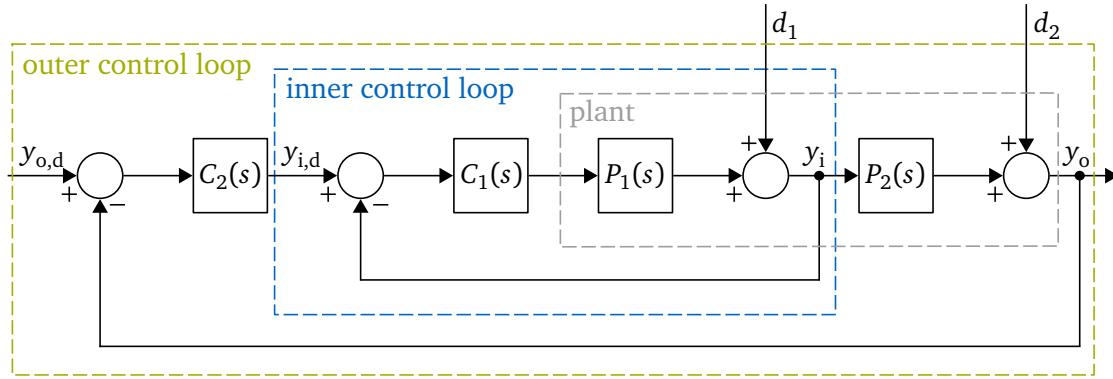


**Figure 2.7:** Cascade control scheme according to [15]

A PPI-cascade is a cascade control which implements a PI-controller for  $C_1(s)$  and a P-controller for  $C_2(s)$ . Furthermore, for motion control of manipulators, it is common practice to perform inner velocity and outer position control. The integral part of the PI-controller produces zero steady-state error in case of constant disturbance signals.

Instead of treating coupling effects among joints as disturbances, they can also be directly modeled within a complete dynamic model of the robot. This is the basis of the *multijoint model* approach. Interested readers can have a look at [24, Chap. 8] for further information.

### 2.2.3 Hybrid Position/Force Control of Manipulators

The concept of hybrid position/force control was developed in [6] and [20]. In contrast to indirect force control schemes, it is based on the assumption that although the manipulator is kinematically coupled to its environment, it does not dynamically interact with it, i.e. the mechanical work exchanged by the manipulator and its environment is equal to zero [8]. This allows us to control the robot-environment interaction by a pure position and a pure force controller, both acting separately. Imagine a robot that is supposed to clean a window. On the window's surface, the robot is supposed to move in horizontal and vertical direction in-plane ( $dx \neq 0$ ), without exerting force on the window in these directions ( $F = 0$ ). However, the robot may not move out-of-plane, i.e. through the window  $dx = 0$ , but it shall push against its environment, i.e. the window, with a certain amount of force  $F \neq 0$ . So, in both cases, the instantaneous mechanical work done is zero:  $dW = F \cdot dx = 0$  [8]. Polishing is another industrial example where hybrid position/force control can be applied.

As the window example demonstrates, a prerequisite for hybrid position/force control is being able to specify position and force constraints on the robot that is being controlled. The author of [16] presents a formalism to properly describe such constraints with the help of so-called *C-surfaces*. C-surfaces are smooth hypersurfaces with dimension  $n_p$ , that consist of all possible positions and orientations of a manipulator's TCP and only allow freedom of motion along their tangents and freedom of force along their normals. They are used to model robots' natural constraints which are given by the geometry and mechanical characteristics of the task configuration. This means that natural constraints split the robot's set of  $n$  DOFs into a subset of  $n_p$  DOFs along the C-surface's tangents which are position-controlled and into a subset of  $n_f = n - n_p$  DOFs along the C-surface's normals that are force-controlled. Any desired position or force trajectory is an artificial constraint and must be specified in accordance with the natural constraints. In the window-example above, an appropriate C-surface would

be the window's surface. So, the robot's motion in the horizontal and vertical direction on the window's surface is supposed to be position-controlled, whereas the motion normal to it has to be force-controlled. The paper [16] deals with several types of C-surfaces and gives adequate examples of corresponding manipulator tasks.

Figure 2.8 shows the hybrid position/force control scheme presented in [20]. It consists of a position control loop and a complementary force control loop, each with its own sensors and its own control law. Input to the control loops are a target position trajectory  $\mathbf{x}_d^{(C)}$  as well as a target force trajectory  $\mathbf{F}_d^{(C)}$  for the TCP, both expressed in the constraint frame  $\{C\}$ . This is a frame in which all natural and artificial constraints can be described according to [16]. Often it is a Cartesian frame that does not have to be equal to the workspace or joint space frame of the manipulator. The compliance selection matrix  $\mathbf{S} \in \mathbb{R}^{n \times n}$  is a diagonal matrix which only accepts binary values, i.e. 0 and 1, on its diagonal. An entry equal to 1 indicates that the corresponding DOF in the constraint frame  $\{C\}$  is force-controlled, whereas DOFs that are supposed to be position-controlled are marked by an entry equal to 0. In fig. 2.8,  $\mathbf{I}$  represents a  $n \times n$  identity matrix that swaps the binary entries for the position control loop. By the multiplication with  $\mathbf{S}$  and  $\mathbf{I}-\mathbf{S}$  respectively, each DOF in  $\{C\}$  is controlled by either a pure position controller or a pure force controller, but after appropriate coordinate transformations their outputs are added by superposition, so both control concepts are used together to control each manipulator joint. In the position control loop, the actual position of the TCP  $\mathbf{x}^{(S)}$  and in the force control loop, the actual contact forces at the end-effector  $\mathbf{F}^{(S)}$  are measured, each in its own sensor coordinate frame  $\{S\}$ . In a final step, the measured position and force signals have to be transformed into the constraint frame  $\{C\}$  by a coordinate transformation in order to be able to compare them with the target trajectories  $\mathbf{x}_d^{(C)}$  and  $\mathbf{F}_d^{(C)}$ .

One way of implementing hybrid position/force control on a serial robot is shown in [25].

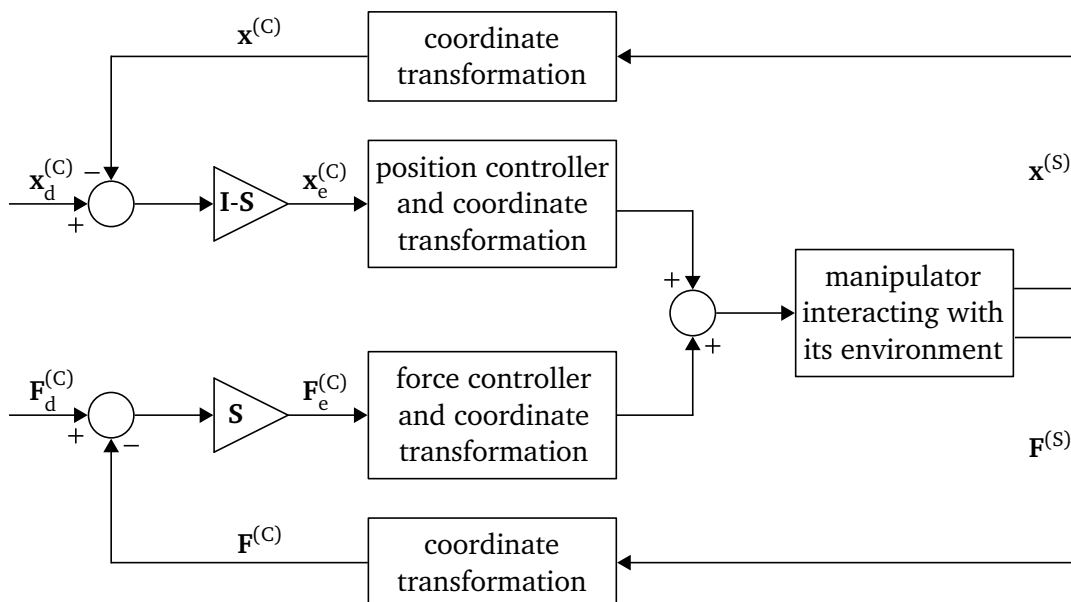


Figure 2.8: Hybrid position/force control scheme according to [20]

### 2.2.4 Position-based Impedance Control of Manipulators

Figure 2.9 shows a popular way of implementing indirect force control. The scheme represents a *position-based impedance control* and is presented in [17]. Like all position-based approaches, it consists of an inner position control loop, that can either be workspace or joint space control, surrounded by an outer loop that is usually implemented in workspace and is based on measuring interaction forces  $\mathbf{F}$ . This structure ensures that the outer loop only modifies the inner loop if the manipulator is in contact with the environment. Otherwise, the robot is controlled by a conventional position control concept.

The outer loop's purpose is to shape a desired dynamic relationship between the interaction forces  $\mathbf{F}$  and the resulting deviation in position  $\Delta\mathbf{x}$  from a target trajectory of the TCP  $\mathbf{x}_d$  due to the force feedback compensator  $\mathbf{G}_{\Delta\mathbf{x},\mathbf{F}} = (\mathbf{M}s^2 + \mathbf{D}s + \mathbf{K})^{-1}$  according to eq. (2.9). The shaping is performed by modifying the matrices  $\mathbf{M}$ ,  $\mathbf{D}$  and  $\mathbf{K}$  respectively.

The position modification  $\Delta\mathbf{x}$  is subtracted from the target position trajectory  $\mathbf{x}_d$ , resulting in the reference position  $\mathbf{x}_r$  as input for the inner position control loop whose task is to guarantee good tracking of  $\mathbf{x}_r$ . The input for the inner position controller is then:

$$\mathbf{x}_e = \mathbf{x}_r - \mathbf{x} = \mathbf{x}_d - \Delta\mathbf{x} - \mathbf{x} = \mathbf{x}_d - \mathbf{x} - \mathbf{G}_{\Delta\mathbf{x},\mathbf{F}}\mathbf{F}. \quad (2.16)$$

The equation describes the difference between the target admittance model and the real system behavior, also known as the *impedance control error* expressed by means of *position measure* [14]. By nullifying the control error  $\mathbf{x}_e$ , the inner position controller forces the actual position of the TCP  $\mathbf{x}$  to be:

$$\mathbf{x} = \mathbf{x}_d - \mathbf{G}_{\Delta\mathbf{x},\mathbf{F}}\mathbf{F}. \quad (2.17)$$

Thus, position-based impedance control aims at reaching an area close to the desired position  $\mathbf{x}_d$  and compliantly moving further in the desired direction according to the target admittance behavior specified by the force feedback compensator  $\mathbf{G}_{\Delta\mathbf{x},\mathbf{F}}$  [1].

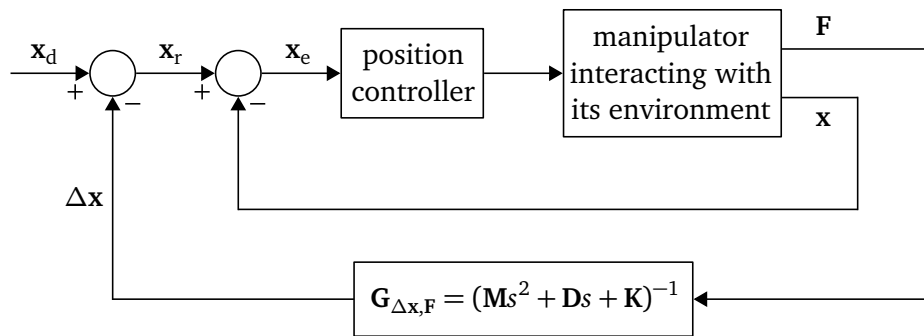


**Figure 2.9:** Position-based impedance control scheme according to [17, p. 25]

As already noted in section 2.2.1, the position-based impedance control scheme presented in fig. 2.9 is easy to implement because most of the manipulators used in industry are controlled by a conventional position controller. Furthermore, it achieves high positioning accuracy when using a stiff target admittance. On top of that, the position-based impedance control scheme manages to operate successfully in free space as well as in contact tasks [5].

One way of implementing a position-based impedance controller for a Hexapod walking robot is shown in [30].

## 2.3 System Structure and Functionalities of the Chair's Stewart Platform

The *Chair of Applied Mechanics* at the *Technical University of Munich* owns a Stewart platform whose control concepts have fundamentally been refined by Sandor Riebe during his dissertation [22, 23]. In the context of several Semester theses, students further worked on the Stewart platform [28] and derived a dynamic model of the system [26] as well as implemented an independent joint control [18] for pure motion control tasks. The following sections give an overview of the structure of the Stewart platform as well as of the currently implemented functionalities which I have used within the experimental part of this thesis.

### 2.3.1 System Components

The components of the overall system can be divided into mechanical components and electrical and software components. This section explains the components relevant for this work that have mostly been covered in [18] and [23].

#### Mechanical Components

Figure 2.10 shows the mechanical components of the Stewart platform at the Chair of Applied Mechanics. It consists of six legs that connect a fixed base platform with an upper platform through cardan joints. The upper platform can be moved by modifying the legs' lengths, which is done by actuating six AC servomotors to rotate the legs' spindles into or out of the cylinders. Upper and lower limit switches indicate the extreme positions of the spindles and a resolver inside the servomotor is used to detect the legs' actual lengths. [18]

A six axes force/torque sensor, type FTS, produced by *SCHUNK GmbH & Co. KG* [7] is mounted on the TCP. It can measure forces and torques along the three translational and three rotational DOFs of the Stewart platform using strain gauges. The environment is represented by two masses, a compression spring and a stiff metal plate, displayed more in detail in fig. 2.11. The lower mass is attached to the force/torque sensor and connected to the upper mass via the spring. The metal plate is mounted on the top. The compression spring is needed to model a flexible, compressible environment and the two masses serve as a support for the spring. The spring stiffness is set to  $k_E = 10000 \frac{\text{N}}{\text{m}}$ . The metal plate acts as a mechanical barrier against which the Stewart platform can exert forces and torques. This setup has been proposed in [11] and is equivalent to a structure where the mass-spring system is fixed to the upper metal plate, representing a compliant environment.

#### Electrical and Software Components

The analog measurement data of the force/torque sensor is transmitted to a FTS evaluation unit produced by *SCHUNK GmbH & Co. KG* [7] and further to a connector box to connect it to a real-time system. Additionally, the sensor signals of the resolver and the limit switches are relayed to the real-time system via a connector box which, in the other direction, transfers voltage signals generated by the real-time system to the servomotors of the Stewart platform via an electrical enclosure. Note, that each of the six servomotors are actuated by a servo amplifier which contains a current controller, so actually the voltage signals generated by the real-time system are used as target current input signals for the current controllers which ensure that these current signals are observed. The real-time system is composed of a Digital Signal Processor (DSP) (dSpace MicroLabBox ds1202) and a Host PC with the operating system (OS) *Windows 10* and the software *MATLAB®/Simulink®* (version R2016b) and *ControlDesk®* (version 6.0). All the algorithms that are explained in section 2.3.2 and

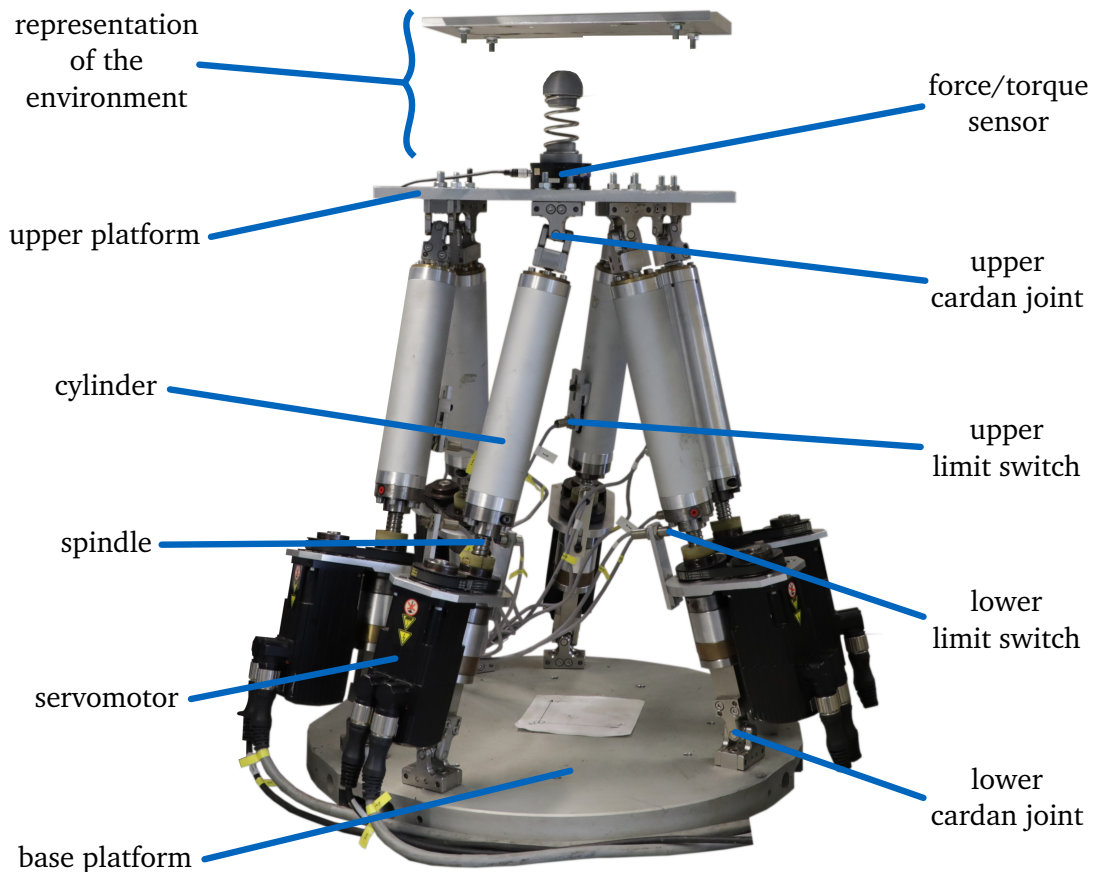


Figure 2.10: Stewart platform at the Chair of Applied Mechanics

chapter 3 are implemented in MATLAB<sup>®</sup>/Simulink<sup>®</sup>. The resulting Simulink<sup>®</sup>-model can be compiled, converted to C-code and loaded onto the DSP. ControlDesk<sup>®</sup> allows to change system parameters in real time and to record series of measurement. [18]

More details concerning the system components of the Stewart Platform can be found in [18] and [23].

### 2.3.2 Implemented Functionalities

The Simulink<sup>®</sup> model encompasses six major modules: referencing, safety functions, trajectory generation, forward and inverse kinematics and motion control [18].

#### Referencing

As the resolvers are only able to detect the position of the legs incrementally, i.e. in a relative manner, a referencing has to be executed before operating on the Stewart platform to determine the current position of each leg. The student thesis [18] gives some more information about the referencing.

#### Safety Functions

Except during referencing, all limit switches are directly connected to the servomotors on a hardware level via the electrical enclosure. So, in order to avoid damage on the Stewart

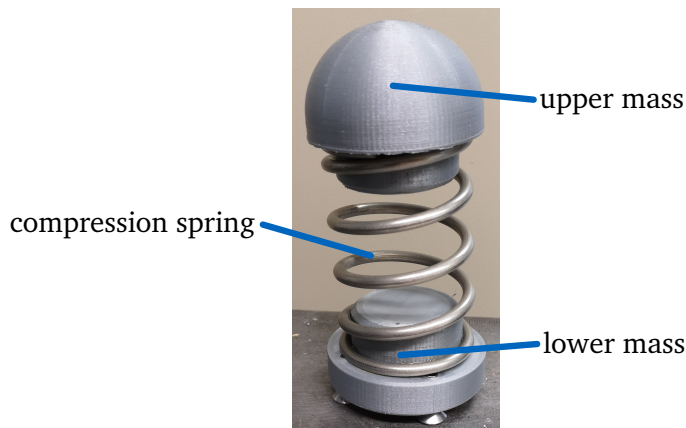


**Figure 2.11:** Detailed view of the representation of the robot's environment (excluding the metal plate)

platform, activating a limit switch by moving a leg too far upwards or downwards leads to immediate stoppage of the upper platform. On top of this hardware-based safety action, [18] implemented several software-based safety functions that are executed in real time. They are able to restrict joint velocity as well as voltage signals for the servomotors and can directly set the servomotors' input signals to zero in case of expected or actual violation of leg length limits and expected violation of cardan joint angle limits as well as whenever the distance to the limit switches falls below a critical value. Additionally, they register task overrun errors which appear whenever execution time of all tasks together exceed sample time. In the context of research for her dissertation, Christina Insam [11] also added implementations that consider actual violation of force and torque value limits and the possibility of the forward kinematics algorithm to be ill-conditioned.

### Trajectory Generation

The trajectory generation module permits the user to specify either a single desired pose or a target pose trajectory for the TCP to reach, both defined in workspace coordinates. After being transformed to joint space coordinates using inverse kinematics, they serve as input reference variables for the controller. [18]

### Forward Kinematics

The forward kinematics module implements Newton's method in order to approximate the actual pose  $\mathbf{x}$  of the Stewart platform's TCP for a given vector of its leg lengths  $\mathbf{b}$  according to [23]. The approach is based on the fact that inverse kinematics allows to algebraically determine  $\mathbf{b}$  from a given pose  $\mathbf{x}$  through a nonlinear, continuously differentiable mapping function  $\mathbf{f}_{\text{inverse}}$  according to eq. (2.4). Thus, we can express  $\mathbf{b}$  by means of a Taylor series about a vector  $\mathbf{x}_0$ . When only using the constant and linear term of the Taylor series, we get:

$$\mathbf{b} \approx \mathbf{f}_{\text{inverse}}(\mathbf{x}_0) + \frac{\partial \mathbf{f}_{\text{inverse}}(\mathbf{x}_0)}{\partial \mathbf{x}_0}(\mathbf{x} - \mathbf{x}_0) = \mathbf{f}_{\text{inverse}}(\mathbf{x}_0) + \mathbf{J}(\mathbf{x} - \mathbf{x}_0), \quad (2.18)$$

where the Jacobian matrix of the Stewart platform is denoted by  $\mathbf{J} = \frac{\partial \mathbf{f}_{\text{inverse}}(\mathbf{x}_0)}{\partial \mathbf{x}_0}$ . Rewriting eq. (2.18) in terms of  $\mathbf{x}$  and setting  $\mathbf{x}$  to  $\mathbf{x}_{n+1}$  and  $\mathbf{x}_0$  to  $\mathbf{x}_n$  leads to the iteration rule of iteration step  $n + 1$  of Newton's method:

$$\mathbf{x}_{n+1} = \mathbf{x}_n + \mathbf{J}^{-1}(\mathbf{b} - \mathbf{f}_{\text{inverse}}(\mathbf{x}_n)), \quad n = 0 \dots k_{\text{max}}. \quad (2.19)$$

It holds true for  $\det(\mathbf{J}) \neq 0$ , i.e. for every nonsingular configuration of the Stewart platform. Note, that in contrast to [23], we used a sum instead of a subtraction in eq. (2.19). This seems to be a mistake in [23].

The algorithm stops once the maximum approximation error  $\epsilon_{\max}$ , describing the maximum error between measured and approximated leg lengths, falls below a user-defined value  $\epsilon_{\text{tol}}$ :

$$\epsilon_{\max} = \max(|\mathbf{b} - \mathbf{f}_{\text{inverse}}(\mathbf{x}_n)|) < \epsilon_{\text{tol}}, \quad \epsilon_{\text{tol}} > 0, \quad (2.20)$$

or once the user-defined maximum number of iterations  $k_{\max}$  is reached. The algorithm quadratically converges to the right solution if the initial guess  $\mathbf{x}_0$  is close to the actual coordinates of the TCP.

The implementation in Simulink outputs the approximated pose of the TCP  $\mathbf{x}_{k_{\max}}$  as well as the actual Jacobian matrix  $\mathbf{J}$  for a given vector of leg lengths  $\mathbf{b}$ .  $k_{\max}$  is set to 5 and  $\epsilon_{\text{tol}}$  is limited to 23  $\mu\text{m}$  in accordance with the maximum positioning error of the spindles due to manufacturing tolerances [23]. It is important to ensure that the computation time for the Newton-iterations does not exceed the system's sample time of 1 ms.

### Inverse Kinematics

The inverse kinematics module computes leg lengths  $\mathbf{b}$  of the Stewart platform for a given pose of its TCP using the kinematic relationships described in [23].

### Motion Control

[18] has designed an independent joint controller based on the single-joint model in the form of a PPI-cascade, one for each leg. While section 2.2.2 has already explained the theory of such a control scheme, fig. 2.12 shows the current implementation on the Stewart platform. [18] also included an optional velocity feed-forward controller to be able to generate a target velocity  $\dot{b}_d$  for each leg.

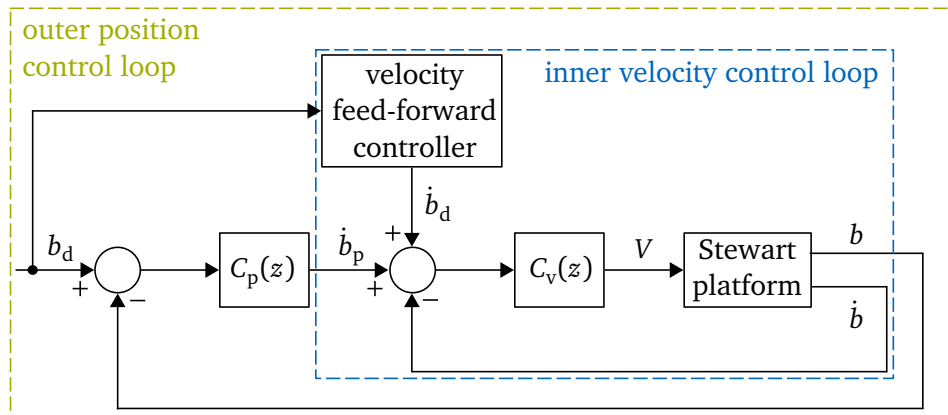


**Figure 2.12:** Implementation of an independent joint controller based on the single-joint model in the form of a PPI-cascade according to [18]

In an inner loop, the leg's velocity  $\dot{b}$  is controlled by a discrete-time PI-controller

$$C_v(z) = K_{p,v} + K_{I,v} \cdot T_s \frac{1}{z-1}, \quad (2.21)$$

while the outer loop aims at controlling the leg's length  $b$  with a discrete-time P-controller

$$C_p(z) = K_{p,p}. \quad (2.22)$$



$T_s$  is the sample time of the controller and is set to 1 ms. [18] has tuned the control parameters based on an identification of the system according to [18] and [23]. The following values are used:  $K_{p,p} = 20 \frac{1}{s}$ ,  $K_{p,v} = 0.2 \frac{Vs}{mm}$  and  $K_{I,v} = 1 \frac{V}{mm}$ . The output of the P-controller  $\dot{b}_p$  is considered to be a velocity, while the inputs for the Stewart platform computed by the PI-controller are the servomotors' voltage values  $V$  of each leg. The velocity resulting from the sum of the output signals of the P-controller and the velocity feed-forward controller as well as the voltage input signal for the Stewart platform can be limited to a defined value  $\dot{b}_{max}$  and  $i_{max}$  respectively. This is part of the safety functions described above. Note, that the restriction of the voltage signal is named  $i_{max}$  because of the former explained fact that the signal is actually used as an input for the current controllers of the servo amplifiers. The actual leg length  $b$  is measured by the resolver, while the actual leg velocity  $\dot{b}$  is computed by differentiating the leg length with respect to time and smoothing the resulting signal with a finite impulse response (FIR) filter. The desired reference length for each leg  $b_d$  is computed from the user's target specification in the trajectory generation module using indirect kinematics.

Within the following sections of this thesis, I use the term *independent joint control* for simplicity to describe the implemented control scheme displayed in fig. 2.12. The velocity feed-forward control has been disabled for all experiments in the context of this work.



## Chapter 3

# Realization of Compliant Motion Control Schemes on the Stewart Platform

The currently implemented system contains an independent joint controller for pure motion control tasks. In order to be able to also perform contact tasks on the Stewart platform, the aim of this thesis is to design, implement and test an approach to indirect as well as direct force control and compare those two. On the one hand, hybrid position/force control is chosen because it is a very common and simple representative of direct force control. On the other hand, position-based impedance control shall be realized as impedance/admittance control is the most general concept of indirect force control and because the existing independent joint controller can be reused for the position-based approach. The following chapter describes all necessary steps to realize both control schemes. Firstly, section 3.1 deals with the extension of the experimental setup and section 3.2 explains how data generated by the force/torque sensor has to be adapted before being used by the controllers. Thereafter, section 3.3 and section 3.4 present the realization of both control concepts on the Stewart platform. Finally, section 3.5 proposes some test cases for testing, validation and comparison of the implementations.

### 3.1 Extension of the Experimental Setup

The existing experimental setup shown in fig. 2.10 only allows to properly execute tests where interaction forces in vertical direction appear because the upper metal plate is the only flat contact surface. Thus, another small metal plate is installed to enable validation of the compliant motion control schemes in horizontal direction. As it is only needed for two tests, the small plate is fixed with Gaffer tape as a workaround. Figure 3.1 shows a picture of the extended experimental setup. There, the lower mass of the support for the spring is different from the one in fig. 2.10 and fig. 2.11 due to further development on the support that took place parallel to the experiments in the context of this thesis. However, the new lower mass was only used for three experiments and does not change the behavior of the robot-environment interaction in comparison to the old one.

The two metal plates are the only contact surfaces where robot-environment interaction takes place in this setup. As they lie in the  $xy$ - and  $yz$ -plane of the workspace coordinate system, it is reasonable to choose the constraint frame  $\{C\}$ , that has been theoretically introduced in section 2.2.3, to be equal to the manipulator's workspace coordinate frame  $\{W\}$ .



**Figure 3.1:** Extension of the experimental setup

### 3.2 Data Processing of the Force/Torque Sensor Signals

Both hybrid position/force control and position-based impedance control require force and torque measuring. However, the output signals of the force/torque sensor have to be adapted before being used for control purposes. Data processing comprises the steps displayed in fig. 3.2, which have to be performed one after another.

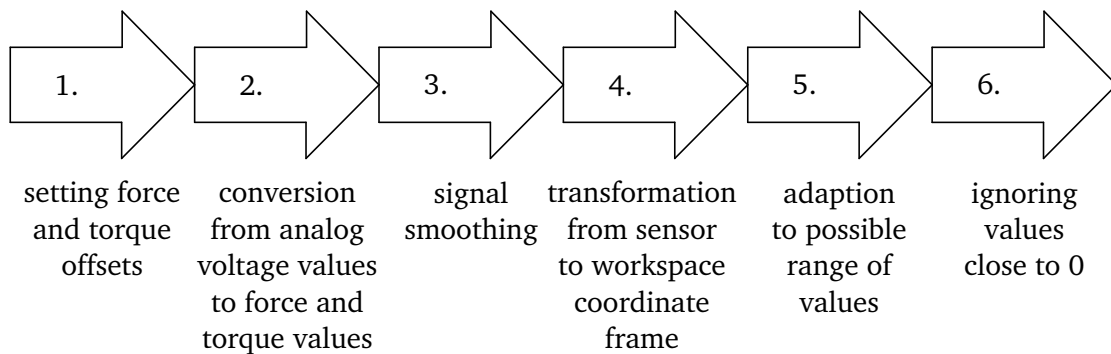


**Figure 3.2:** Data processing steps

Note, that data processing strongly depends on the experimental setup. The steps mentioned are necessary for the specific Stewart platform and the force/torque sensor that has been worked with in the context of this thesis. For other parallel robots and sensors, data processing might look different.

#### Setting Force and Torque Offsets

Similar to the referencing described in section 2.3.2, an origin for the force and torque measurements has to be defined before operating the Stewart platform in contact tasks. Therefore, the upper platform is driven to a specified pose where the actual output values of the force/torque sensor are measured for an adequate amount of time. For this Stewart platform, a time span of 10 s is chosen. The mean values of this measurement are saved as force and torque offsets and are subtracted from the sensor values during operation. The correspon-

ding implementations have been realized by Christina Insam in the context of experiments for her dissertation [11].

### Conversion from Analog Voltage Values to Force and Torque Values

The force/torque sensor outputs analog voltage values that range from  $-5$  V to  $+5$  V. Its specified measuring range is  $[-130$  N,  $+130$  N] for forces and  $[-10$  Nm,  $+10$  Nm] for torques [7]. Thus, a conversion to force and torque values can easily be performed by multiplying the sensor signals by the constant factors  $\frac{130 \text{ N}}{5 \text{ V}}$  and  $\frac{10 \text{ Nm}}{5 \text{ V}}$  respectively.

### Signal smoothing

Sensor signals characteristically contain noise and outliers. To get more realistic values, it is reasonable to smooth sensor data output. This is commonly done by a low-pass filter. As tuning the filter usually requires some knowledge of the noise, a simpler alternative method is chosen: the moving average. Each sample step, it computes the average over the data in a window of a user-defined length, while the window is sliding over the whole measurement data set sample by sample.

### Transformation from Sensor to Workspace Coordinate Frame

So far, we can describe the measured forces and torques along/about each axis of the sensor coordinate frame  $\{S\}$ , combined in the following vector:

$$\mathbf{F}^{(S)} = \begin{pmatrix} F_x \\ F_y \\ F_z \\ M_x \\ M_y \\ M_z \end{pmatrix}^{(S)}. \quad (3.1)$$

The force/torque sensor is mounted on the Stewart platform in a way that its coordinate frame  $\{S\}$  does not conform to the manipulator's workspace coordinate frame  $\{W\}$ . Figure 3.3 illustrates their relation. Note, that positive directions indicate tensile forces.

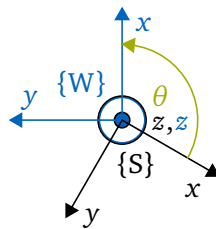


**Figure 3.3:** Sensor and workspace coordinate frames

Actually, the force/torque sensor is characterized by a right-handed system [7]. However, it is mounted on the TCP upside down which turns it into a left-handed system. For further computations, it is necessary to express the six measured force and torque values in the workspace coordinate frame of the Stewart platform in order to be able to achieve decoupled compliant motion control. Therefore, a coordinate transformation has to be performed. According to fig. 3.3, at first, the  $y$ -axis of the sensor coordinate system  $\{S\}$  has to be swapped in order to receive a right-handed system. Afterwards, the resulting frame can be rotated about

the  $z$ -axis through the angle  $\theta = 120^\circ$  expressed by an elementary rotation [24, Chap. 18]. Thus, the corresponding rotation matrix  $\mathbf{R}_{WS}$ , that transforms a vector expressed in coordinate frame  $\{S\}$  to a vector expressed in coordinate frame  $\{W\}$ , is:

$$\mathbf{R}_{WS} = \begin{pmatrix} 1 & 0 & 0 \\ 0 & -1 & 0 \\ 0 & 0 & 1 \end{pmatrix} \begin{pmatrix} \cos \theta & -\sin \theta & 0 \\ \sin \theta & \cos \theta & 0 \\ 0 & 0 & 1 \end{pmatrix} = \begin{pmatrix} \cos \theta & -\sin \theta & 0 \\ -\sin \theta & -\cos \theta & 0 \\ 0 & 0 & 1 \end{pmatrix}. \quad (3.2)$$

The force/torque vector can then be written in the workspace coordinate frame by means of the following coordinate transformation:

$$\mathbf{F}^{(W)} = \begin{pmatrix} F_x \\ F_y \\ F_z \\ M_x \\ M_y \\ M_z \end{pmatrix}^{(W)} = \begin{pmatrix} \mathbf{R}_{WS} & \mathbf{0} \\ \mathbf{0} & \mathbf{R}_{WS} \end{pmatrix} \begin{pmatrix} F_x \\ F_y \\ F_z \\ M_x \\ M_y \\ M_z \end{pmatrix}^{(S)}, \quad (3.3)$$

where  $\mathbf{0}$  is a  $3 \times 3$  zero matrix.

#### Adaption to Possible Range of Values

Often in real applications, variables can only reach certain values due to constraints resulting from a specific setup. For the structure presented in fig. 2.11 and fig. 3.1, we can restrict forces in vertical direction to be non-positive ( $F_z^{(W)} \leq 0$ ) as the only way to measure contact forces in vertical direction is to compress the spring by moving the TCP against the upper metal plate. For the existing experimental setup, it would also be possible to set  $F_x^{(W)} \leq 0$  and  $F_y^{(W)} = M_x^{(W)} = M_y^{(W)} = M_z^{(W)} = 0$  because the metal plates lying in the  $xy$ - and  $yz$ -plane of the workspace coordinate system are the only contact surfaces to be used. However, this restriction can easily be invalidated by placing additional barriers in the workspace of the Stewart platform. The implementation shall be kept as general as possible, so all the other force and torque values except from  $F_z^{(W)}$  may not be limited.

#### Ignoring Values close to 0

In many applications, contact forces and torques simultaneously occur only within a subset of the whole set of DOFs of a manipulator due to its natural constraints. For the existing experimental setup of the Stewart platform for example,  $F_x^{(W)}$  and  $F_z^{(W)}$  are the relevant contact forces appearing at the same time and thus, in theory, they exclusively influence control, at least when dealing with decoupled control schemes. However, in practice, noise induces non-zero force/torque values also along the other DOFs and thus effects control, even after having smoothed the sensor signals with the help of the moving average approach. On top of that, noise can even impair control for DOFs along which real contact forces and torques can be measured, especially on the boundary surfaces where non-contact tasks become contact tasks and vice versa. To ensure that the TCP truly is in contact with its environment, for each element in  $\mathbf{F}^{(W)}$ , all values within a small interval around 0 can be interpreted as noise and thus be ignored. On the one hand, this can be done by strictly setting the signal to zero whenever its absolute value falls below a threshold. On the other hand, the threshold can also be subtracted from the absolute value of the sensor signal, leading to a dead zone within a defined interval. The drawback of the first approach is that the force/torque signal immediately jumps from a certain threshold to zero. In exchange, it does not change the

rest of the values in contrast to the second approach which constantly reduces measured forces and torques. In return, it smoothly reaches zero values. Figure 3.4 exemplifies both approaches by showing the results for an imaginary perfect force sine wave without any noise and a threshold of 2 N.

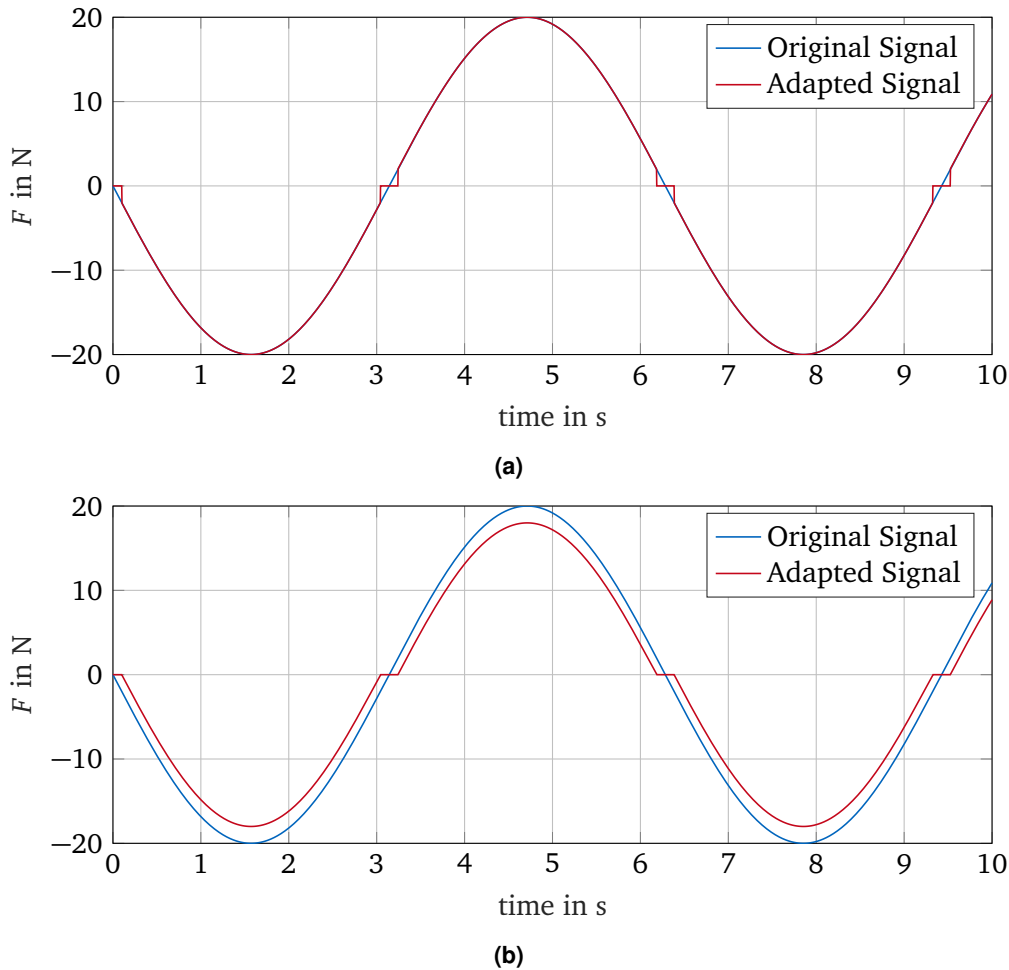


**Figure 3.4:** Ignoring force values in the interval  $[-2, 2]$  by (a) a strict threshold and (b) subtraction

Another effect to be aware of is that due to the inertia of the two masses in the mass-spring system shown in fig. 2.11, contact forces/torques may be measured by the force/torque sensor when accelerating the upper platform of the Stewart platform, even if the robot is not in real contact with its environment. As a result, the threshold has to be larger than the force caused by the inertia and acceleration of the mass-spring system.

For the existing Stewart platform, we apply the second approach because for further applications, an immediate jump in the force/torque signals is not desirable, while a constant offset can be accepted. The threshold is set to 2 N for force signals and to  $\frac{2}{13}$  Nm for torques. The ratio between force and torque threshold can be traced back to the measuring range mentioned four paragraphs above.

All the steps of data processing presented in this section, result in an adjusted force/torque signal that can be used by a hybrid position/force controller as well as by a position-based impedance controller. The signal will be referred to by the variable  $\mathbf{F}$  for abbreviation.

### 3.3 Realization of Hybrid Position/Force Control

Based on the theory explained in section 2.2.3 and the control scheme shown in fig. 2.8, a hybrid position/force control has been designed and implemented for the Stewart platform presented in section 2.3. Figure 3.5 shows the controller itself, while fig. 3.6 illustrates how the controller has been integrated in the existing system. The gap symbols in the first figure represent necessary signal conversions and transformations that are explained in more detail in the scope of the latter figure.

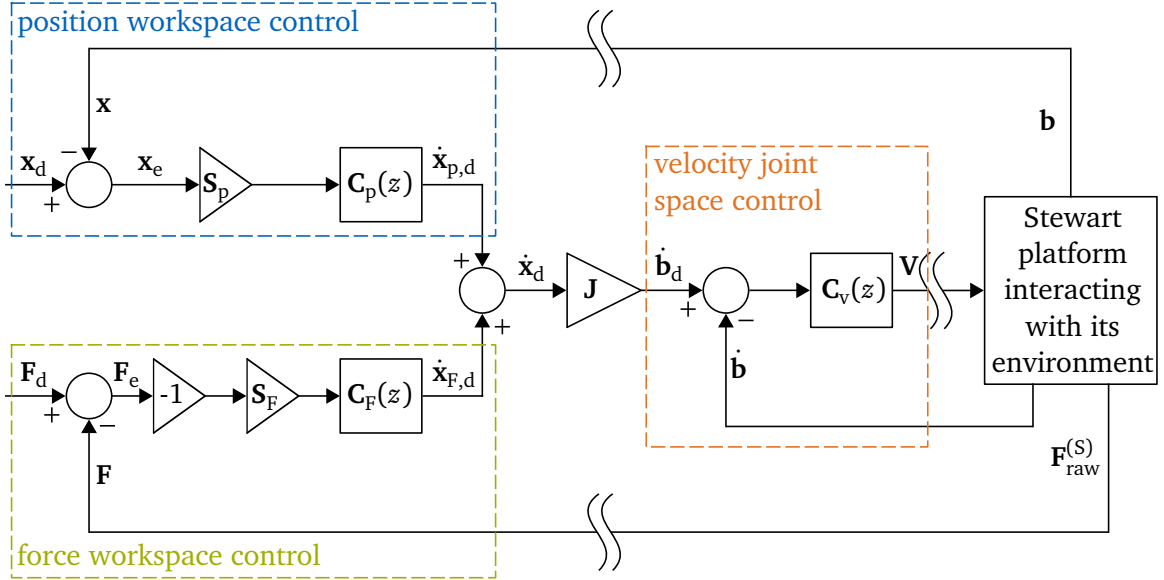


Figure 3.5: Realization of a hybrid position/force controller on the Stewart platform

For the hybrid position/force controller, a PPI-cascade control scheme is chosen. The inner loop of the cascade is a velocity control loop with a discrete-time PI-controller  $C_v(z)$ , realized in joint space in order to be able to reuse the velocity controller of the already existing independent joint controller described in section 2.3.2. It nullifies the error between the desired and the actual joint space velocity  $\dot{\mathbf{b}}_d$  and  $\mathbf{b}$  and outputs a vector  $\mathbf{V} = (V_1 V_2 V_3 V_4 V_5 V_6)^T$  containing voltage values used to provide target values for the current controllers of all servo amplifiers of the Stewart platform. The values can be limited to a defined threshold  $i_{\max}$  for safety reasons. It would be possible to add a velocity feed-forward controller analog to the one in the existing independent joint control. However, this goes beyond the scope of this thesis.

The outer loop of the cascade complies with the classical hybrid position/force control scheme presented in fig. 2.8. It is composed of two discrete-time P-controllers  $C_p(z)$  and  $C_F(z)$  which separately control the pose of the TCP on the one hand and interaction forces and torques of the Stewart platform with its environment on the other hand. The outputs of both controllers  $\dot{\mathbf{x}}_{p,d}$  and  $\dot{\mathbf{x}}_{F,d}$  are interpreted to be workspace velocity vectors that, if added in terms of superposition, result in the target velocity vector of the TCP  $\dot{\mathbf{x}}_d$ . Then, eq. (2.5) is used to compute the desired leg velocities  $\dot{\mathbf{b}}_d$ . Again, these values can be limited to a defined threshold  $\dot{b}_{\max}$  for safety reasons. Both the position controller and the force controller operate in the manipulator's workspace because firstly, it allows to easily interpret controller parameters and secondly, it helps avoiding unnecessary coordinate transformations as for the existing Stewart platform, the constraint frame  $\{C\}$  is equal to the manipulator's workspace coordinate frame  $\{W\}$ . Thus, target position and force trajectories  $\mathbf{x}_d$  and  $\mathbf{F}_d$  are also defined in



workspace coordinates. Again, the multiplication with a compliance matrix guarantees that each DOF in  $\{C\}$ , i.e. each translational and rotational DOF in  $\{W\}$ , is controlled by either the position controller or the force controller. To ease further investigations, we distinguish between a *force selection matrix*  $\mathbf{S}_F \in \mathbb{R}^{6 \times 6}$  and its counterpart, called *position selection matrix*  $\mathbf{S}_p \in \mathbb{R}^{6 \times 6}$ . The relation  $\mathbf{S}_p = \mathbf{I} - \mathbf{S}_F$  still holds true. Additionally, both matrices are diagonal and again an entry equal to 1 in the force selection matrix and equal to 0 in the position selection matrix indicates the corresponding DOF to be purely controlled by the force (and velocity) controller, while defining an entry equal to 0 in the force selection matrix and equal to 1 in the position selection matrix leads to pure position (and velocity) control of the corresponding DOF. The multiplication by  $-1$  in the force control loop results from the definition of the coordinate frames  $\{S\}$  and  $\{W\}$ .

The controllers in fig. 3.5 are represented by their transfer function matrices. They are diagonal  $6 \times 6$  matrices, containing transfer functions of the same type on their diagonal, one for each DOF. Thus, each DOF is controlled separately and control is decoupled. The transfer function matrices are chosen in the following way, depending on whether they describe a P- or a PI-controller:

$$\mathbf{C}_p(z) = \text{diag}(C_{p,x}(z), C_{p,y}(z), C_{p,z}(z), C_{p,\alpha}(z), C_{p,\beta}(z), C_{p,\gamma}(z)) \quad (3.4)$$

with

$$C_{p,i}(z) = K_{p,p,i} \text{ for } i \in \{x, y, z, \alpha, \beta, \gamma\}; \quad (3.5)$$

$$\mathbf{C}_F(z) = \text{diag}(C_{F,x}(z), C_{F,y}(z), C_{F,z}(z), C_{F,\alpha}(z), C_{F,\beta}(z), C_{F,\gamma}(z)) \quad (3.6)$$

with

$$C_{F,i}(z) = K_{p,F,i} \text{ for } i \in \{x, y, z, \alpha, \beta, \gamma\}; \quad (3.7)$$

and

$$\mathbf{C}_v(z) = \text{diag}(C_{v,1}(z), C_{v,2}(z), C_{v,3}(z), C_{v,4}(z), C_{v,5}(z), C_{v,6}(z)) \quad (3.8)$$

with

$$C_{v,i}(z) = K_{p,v,i} + K_{I,v,i} \cdot T_s \frac{1}{z-1} \text{ for } i = 1 \dots 6. \quad (3.9)$$

The integral term of the PI-controller is reset whenever  $\mathbf{x}_d$  is set to another value along a DOF that is position-controlled or  $\mathbf{F}_d$  is varied along a DOF that is force-controlled.

Note, that it is not adequate to leave out the inner velocity control loop, even if the legs' velocities shall not be explicitly controlled by making use of a velocity feed-forward controller. The absence of an integral term leads to remaining constant steady-state errors in the position and force control loops. Choosing PI-controllers for  $\mathbf{C}_p(z)$  and  $\mathbf{C}_F(z)$  instead also leads to unsatisfying results, especially because there is no way to prevent extremely high leg velocities.

So far, the hybrid position/force controller has been explained on its own. However, how can it be integrated into the existing system? Figure 3.6 displays all necessary modules and their relationships. Blue background marks the ones that have been implemented or modified in the context of this thesis.

First of all, the trajectory generation module has to enable specifying target force and torque values  $\mathbf{F}_d$  on top of target position and orientation values  $\mathbf{x}_d$  to generate all necessary input

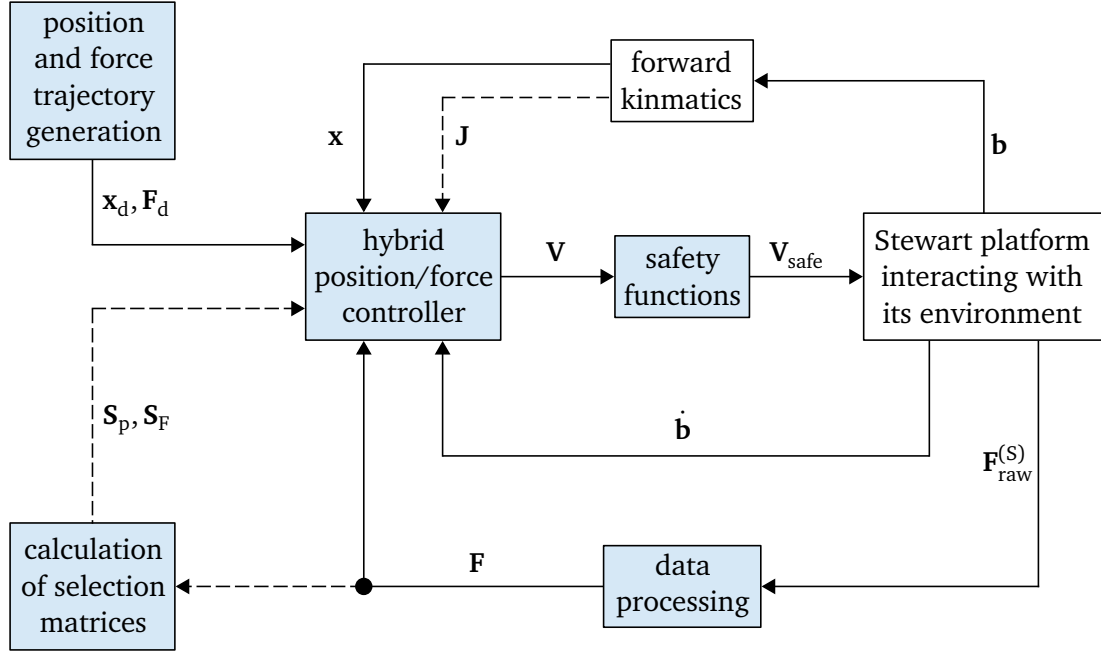


Figure 3.6: Integration of hybrid position/force control onto the Stewart platform

reference signals for the hybrid position/force controller. Thus, the module has been expanded in a way that it allows users to define  $\mathbf{F}_d$  as a single vector of force/torque values or as a sine wave trajectory in  $z$ -direction. If needed, other specifications can be added.

Furthermore, the hybrid position/force controller is dependent on sensor signals which state the actual pose of the TCP  $\mathbf{x}$ , the actual joint space velocity  $\dot{\mathbf{b}}$  and the actual contact force and torque values  $\mathbf{F}$ . However, the resolver can only determine actual leg lengths of the Stewart platform  $\mathbf{b}$  and the force/torque sensor outputs noisy analog voltage values  $\mathbf{F}_{raw}^{(S)}$  (here the letter  $\mathbf{F}$  is used to indicate that the vector results from a force/torque sensor although its unit is volt), expressed in its own coordinate frame  $\{S\}$ . To get appropriate input signals for the hybrid position/force controller, the steps mentioned in section 3.2 are applied on  $\mathbf{F}_{raw}^{(S)}$ , while the already existing forward kinematics module computes  $\mathbf{x}$  from the vector  $\mathbf{b}$ . By analogy to the implementation of the independent joint controller, the actual leg velocity vector  $\dot{\mathbf{b}}$  is received by differentiating  $\mathbf{b}$  with reference to time and smoothing the resulting signal with the help of a FIR filter.

To avoid damage, the safety functions presented in section 2.3.2 are used to modulate the voltage output of the hybrid position/force controller  $\mathbf{V}$  to get the vector  $\mathbf{V}_{safe}$  which can be passed on to the servomotors of the Stewart platform. An additional implementation ensures that  $\mathbf{V}_{safe}$  is set to 0 whenever an entry in  $\mathbf{V}$  becomes NaN due to an error in the Simulink model or any computational errors.

So far, all inputs and outputs of the hybrid position/force controller have been clarified. On top of that, the control scheme illustrated in fig. 3.5 requires knowledge of the actual Jacobian matrix  $\mathbf{J}$  and selection matrices  $\mathbf{S}_p$  and  $\mathbf{S}_F$ . In fig. 3.6 their relationship to other modules is indicated by dashed arrows.  $\mathbf{J}$  can be computed along with Newton's method, implemented in the forward kinematics module described in section 2.3.2, while  $\mathbf{S}_p$  and  $\mathbf{S}_F$  have to be determined separately. Generally, the user has to define a compliance matrix  $\mathbf{S}$  in order to specify the DOFs that shall be position-controlled and those that shall be force-controlled. However, the hybrid position-force controller must not get any information telling it to apply force control along DOFs where no interaction forces exist because the manipulator does not contact its environment along these DOFs. Thus, the adjusted force/torque vector  $\mathbf{F}$  is used

to define a diagonal *contact matrix*  $\mathbf{S}_c$  whose elements on the diagonal are equal to 1 if the corresponding entry in  $\mathbf{F}$  is unequal to 0 and 0 for all the corresponding DOFs where robot-environment interaction does not exist due to an entry equal to 0 in  $\mathbf{F}$ . Then, we can choose force and position selection matrices in the following way:

$$\mathbf{S}_F = \mathbf{S}\mathbf{S}_c, \quad \mathbf{S}_p = \mathbf{I} - \mathbf{S}_F. \quad (3.10)$$

### 3.4 Realization of Position-based Impedance Control

To be able to compare direct and indirect force control, a representative of the class of indirect force control schemes has been implemented over and above the hybrid position/force controller. To keep implementation as simple as possible, a position-based approach is chosen because this allows to reuse the existing independent joint control in the inner position control loop. Also, it is desirable to keep control as general as possible. Thus, impedance/admittance control is preferred to stiffness/compliance and damping control. Altogether, this leads to the position-based impedance control scheme explained in section 2.2.4, with position control taking place in joint space. Figure 3.7 shows its integration in the existing system. Again, blue background indicates new or modified modules.

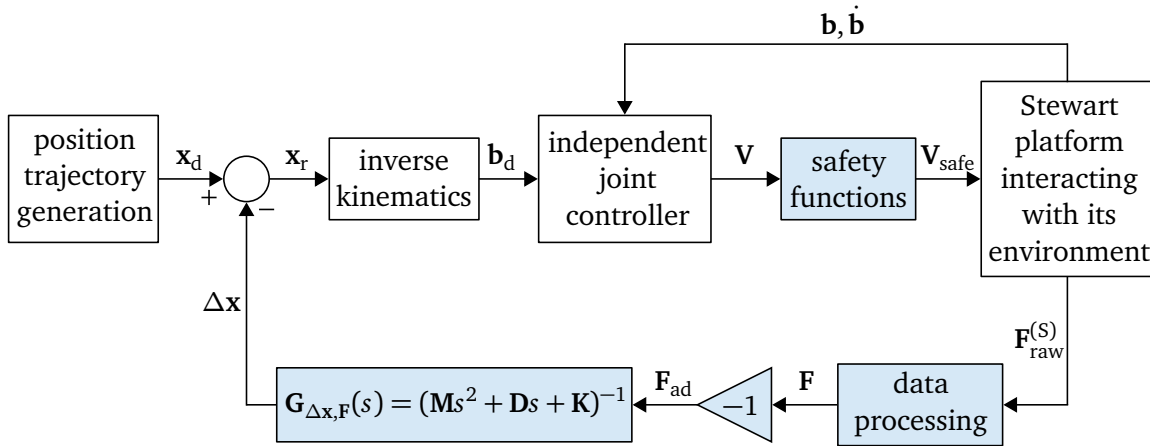


Figure 3.7: Realization and integration of position-based impedance control on the Stewart platform

The upper signal flow in the figure conforms to the one of pure independent joint control presented in [18] and implemented on the Stewart platform. The only adaption in there is the additional implementation of the safety function concerning NaN output values already introduced in section 3.3. Completely new is the feedback based on force/torque sensor data  $\mathbf{F}_{\text{raw}}^{(S)}$ . Analog to the hybrid position/force control scheme, the signal has to pass through the data processing steps explained in section 3.2 to receive an adjusted force/torque vector  $\mathbf{F}$  which can further be used for control purposes. Again, the sign of  $\mathbf{F}$  has to be converted due to the definition of the coordinate frames  $\{S\}$  and  $\{W\}$ . In a final step, the transfer function matrix  $\mathbf{G}_{\Delta x, F}$  adjusts the target admittance behavior defined by the  $6 \times 6$  mass/inertia, damping and stiffness matrices  $\mathbf{M}$ ,  $\mathbf{D}$  and  $\mathbf{K}$  by outputting a pose modification vector  $\Delta \mathbf{x}$  which is subtracted from the desired position trajectory  $\mathbf{x}_d$ . To achieve decoupled behavior,  $\mathbf{M}$ ,  $\mathbf{D}$  and  $\mathbf{K}$  are chosen to be diagonal matrices. Then, the transfer function matrix  $\mathbf{G}_{\Delta x, F}$  also turns into a diagonal  $6 \times 6$  matrix, containing transfer functions of the following type on its diagonal, one for each DOF:

$$\mathbf{G}_{\Delta x, F}(s) = \text{diag}(G_{\Delta x, F}(s), G_{\Delta y, F}(s), G_{\Delta z, F}(s), G_{\Delta \alpha, F}(s), G_{\Delta \beta, F}(s), G_{\Delta \gamma, F}(s)) \quad (3.11)$$

with

$$G_{\Delta i, F}(s) = \frac{1}{M_i s^2 + D_i s + K_i} \text{ for } i \in \{x, y, z, \alpha, \beta, \gamma\}. \quad (3.12)$$

$M_i$ ,  $D_i$  and  $K_i$  mark the  $i^{\text{th}}$  value on the diagonal of the matrices  $\mathbf{M}$ ,  $\mathbf{D}$  and  $\mathbf{K}$  respectively.

As long as the TCP is not in contact with its environment,  $\mathbf{F}$  is zero and thus  $\mathbf{x}_r = \mathbf{x}_d$ . In this case, position-based impedance control is not different from pure independent joint control. However, if  $\mathbf{F} \neq \mathbf{0}$ , the robot-environment interaction is controlled in order to achieve a target admittance behavior specified by the transfer function matrix  $\mathbf{G}_{\Delta x, F}$ . Figure 3.8 shows a mechanical interpretation of position-based impedance control in case of a contact task exemplary for the  $z$ -direction of the Stewart platform. Because of the structure of  $\mathbf{G}_{\Delta x, F}$  described above, diagrams for the other DOFs of the Stewart platform would look the same, except that when describing the relation between measured torques and orientation of the TCP, inertia elements, torsion springs and dampers replace mass elements, compression springs and dampers. Thus, everything explained in the context of fig. 3.8 can also be applied to the other DOFs.

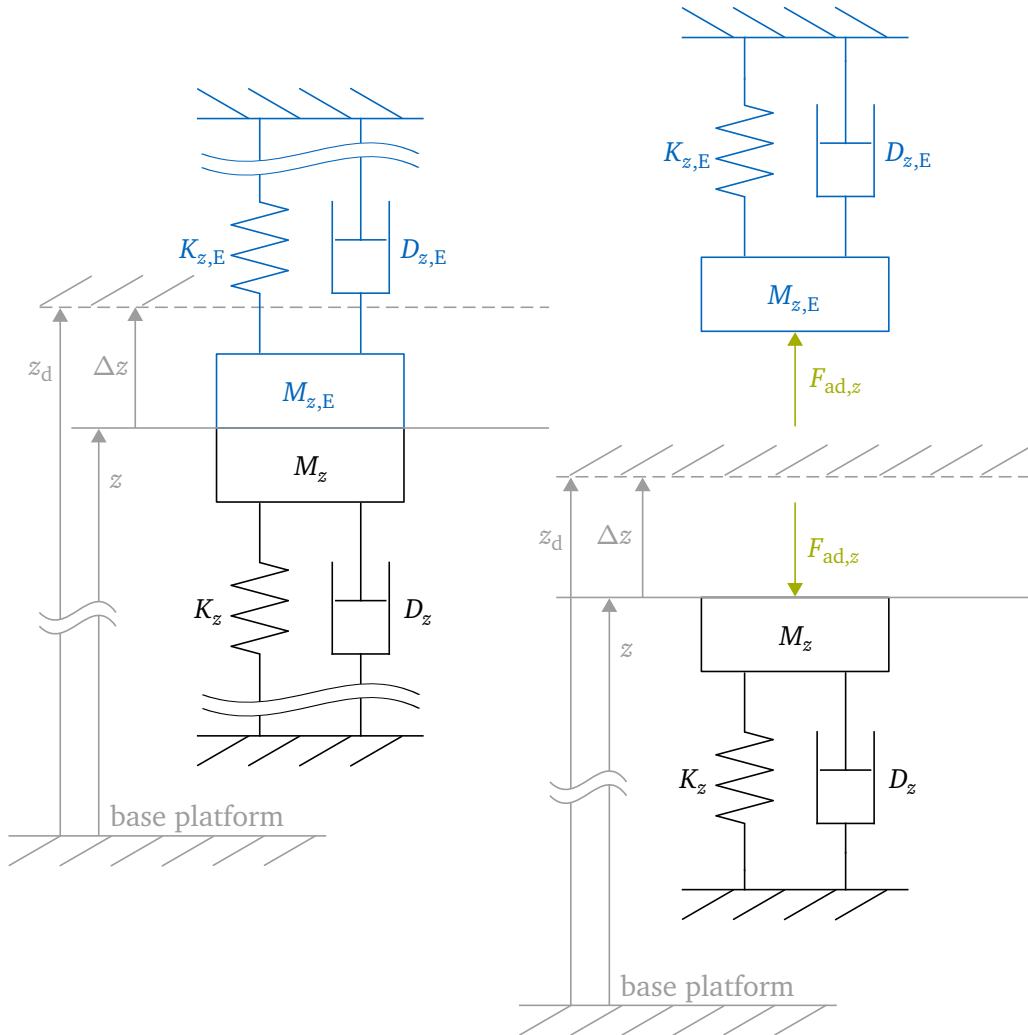


**Figure 3.8:** Interpretation of position-based impedance control exemplary shown in  $z$ -direction

on the left: connected bodies, on the right: free body diagrams

As the target admittance behavior is described by the linear second-order differential equation of a mass-spring-damper system, it can be represented by a virtual mass  $M_z$ , a virtual damper with damping constant  $D_z$  and a virtual spring with stiffness  $K_z$ . The dynamics of the environment can also be simplified to the one of a mass-spring-damper system with a mass  $M_{z,E}$ , a damping constant  $D_{z,E}$  and a stiffness  $K_{z,E}$ . We assume that the upper metal plate as well as the two masses serving as a support in the experimental setup described in section 2.3 are infinitely stiff. Thus, we can set  $K_{z,E} = 10000 \frac{\text{N}}{\text{mm}}$  in accordance with the stiffness  $k_E$  of the real compression spring. Note, that for all the other DOFs, determining stiffness values is not that trivial. Also, it is hard to specify  $\mathbf{M}$  and  $\mathbf{D}$ . The Stewart platform is modeled as an admittance because it accepts the force  $F_{\text{ad},z}$  as input and yields motion along the  $z$ -direction as output. As the environment must physically complement the manipulator, it has to be interpreted as an impedance [8]. The exact positions of the infinitely stiff fixings of the virtual dampers and springs for all DOFs  $i \in \{x, y, z, \alpha, \beta, \gamma\}$  are not relevant because the elements are considered to be linear. Nevertheless, we know that the desired position  $z_d$  is equal to the equilibrium position of the robot's mass-spring-damper system according to the definition in eq. (2.8). In case of robot-environment interaction, the contact surface between  $M_{z,E}$  and  $M_z$  defines the actual position of the TCP  $z$ . The free body diagrams on the right-hand side of fig. 3.8 reveal the contact force  $F_{\text{ad},z}$  between the TCP and its environment. Note, that in fig. 3.8 we focus on the effects caused by the admittance control loop. Thus, we assume  $\mathbf{x} = \mathbf{x}_r$ , in particular  $z = z_r$ , i.e. the inner independent joint controller has accomplished its control goal. Equivalent to eq. (3.12), we can describe the dynamics of the virtual admittance according to Newton's second law of motion:

$$F_{\text{ad},z} = M_z(\ddot{z} - \ddot{z}_d) + D_z(\dot{z} - \dot{z}_d) + K_z(z - z_d) = M_z\Delta\ddot{z} + D_z\Delta\dot{z} + K_z\Delta z, \quad (3.13)$$

where I introduced  $\Delta z = z - z_d$  and similarly  $\Delta\dot{z}$  and  $\Delta\ddot{z}$  respectively, leading to the scalar form of eq. (2.8). The attentive reader may recognize an apparent inconsistency between the reverse directions of  $\Delta z$  and  $F_{\text{ad},z}$  drawn in fig. 3.8 and the signs applied in eq. (3.13). This inconsistency clears up by having in mind that the reference system of eq. (3.13) is not fix because the upper platform and thus the point of application of  $\Delta z$  moves when applying a force  $F_{\text{ad},z}$  on the TCP.

The dynamics of the environment, here modeled by  $M_{z,E}$ ,  $D_{z,E}$  and  $K_{z,E}$  determines the contact force  $F_{\text{ad},z}$  between the TCP and the environment.  $F_{\text{ad},z}$  then leads to a position modification  $\Delta z$  which is subtracted from the desired position  $z_d$  in order to receive a reference position  $z_r$  serving as new input for the independent joint controller. The transient response of the Stewart platform to a desired trajectory  $z_d$  significantly depends on the choice of  $M_z$  and  $D_z$  relative to  $M_{z,E}$  and  $D_{z,E}$ . A mass  $M_z$  that is small relative to  $M_{z,E}$  can be accelerated more quickly towards the desired position  $z_d$  and is also slowed down more easily when finally reaching  $z_d$  than a bigger mass  $M_z$ . Similarly, a value  $D_z$  that is large relative to  $D_{z,E}$  influences the velocity of the TCP  $\dot{z}$  more effectively than a smaller one. The stationary behavior of the virtual mass-spring-damper system depends on its stiffness  $K_z$  relative to  $K_{z,E}$ . Firstly, when looking at fig. 3.8, it becomes clear that, only if  $K_z \geq K_{z,E}$ , i.e. the virtual admittance of the manipulator is stiffer than the environment, it is mechanically possible for the TCP to approach the desired position  $z_d$ . Besides, the TCP is in its pose of equilibrium  $\mathbf{x}_{\text{st}}$  if the target trajectory remains at a constant value  $\mathbf{x}_{d,\text{st}}$  and if  $\mathbf{x} \equiv \mathbf{x}_r$ , which means that the inner independent joint controller has achieved its target of control. As a result, the output voltage vector  $\mathbf{V}_{\text{safe}}$  does not change anymore, which leads to the fact that the contact force and thus also the position modification vector reach their stationary values  $\mathbf{F}_{\text{st}}$  and  $\Delta\mathbf{x}_{\text{st}}$ . Thus, the pose of equilibrium of the TCP is

$$\mathbf{x}_{\text{st}} = \mathbf{x}_{r,\text{st}} = \mathbf{x}_{d,\text{st}} - \Delta\mathbf{x}_{\text{F,st}} = \mathbf{x}_{d,\text{st}} + \mathbf{K}^{-1}\mathbf{F}_{\text{st}} = \mathbf{x}_{d,\text{st}} - \mathbf{K}^{-1}\mathbf{F}_{\text{ad,st}} \quad (3.14)$$

and depends on the stiffness matrix  $\mathbf{K}$  of the virtual admittance. Moreover, eq. (3.14) shows that within position-based impedance control, the virtual mass-spring-damper system of the manipulator may not reach its pose of equilibrium  $\mathbf{x}_{d,st}$ , unless  $\mathbf{F}_{st} = \mathbf{0}$ , i.e. the TCP is not in contact with its environment or unless  $K_i \rightarrow \infty, \forall i \in \{x, y, z, \alpha, \beta, \gamma\}$ . Descriptively speaking this means that for the static case  $t \rightarrow \infty$ , the environment becomes infinitely stiff. As a result, position-based impedance control cannot operate with exact stationary accuracy. However, according to [1], the following principle holds true: "instead of positioning the part with high accuracy at the desired position, it is enough if the robot is able to position the part within the ROA and push it compliantly in the calculated direction". ROA stands for *region of attraction*. Overall, the mechanical interpretation illustrated in fig. 3.8 clearly shows that the choice of the matrices  $\mathbf{M}$ ,  $\mathbf{D}$  and  $\mathbf{K}$  strongly depends on the characteristics of the environment the manipulator is interacting with.

### 3.5 Design and Implementation of Test Cases

In order to be able to test and compare the two control schemes that have been implemented, two different types of test cases are used: step response analysis and following a test trajectory.

#### Step Response Analysis

For basic testing and analyzing the control schemes' influence on the Stewart platform, simple Heaviside step functions are used as input signals for the desired pose of the TCP  $\mathbf{x}_d$  as well as for the desired interaction force/torque vector  $\mathbf{F}_d$  and the corresponding step responses of relevant variables are tracked. This kind of analysis is very suitable and commonly applied to study system behaviors because an excitation with a Heaviside step function contains all frequencies and thus a step response fully describes a system's transfer behavior. In the following tests, step input functions will be defined by a start and an end vector for  $\mathbf{x}_d$  or  $\mathbf{F}_d$  and will be used to analyze both control schemes' performances in contact-tasks and in non-contact tasks as well as when switching from non-contact to contact tasks and vice versa. For hybrid position/force control, both  $\mathbf{x}_d$  and  $\mathbf{F}_d$  can be specified, while for position-based impedance control, only  $\mathbf{x}_d$  can be defined.

To be able to better compare results, independent joint control is used to move the TCP to the start pose  $\mathbf{x}_{start}$ . Then  $\mathbf{x}_{end}$  or  $\mathbf{F}_{end}$  is transmitted to the system and simultaneously the control algorithm is switched from independent joint control to hybrid position/force control or position-based impedance control.

#### Following a Test Trajectory

The second test case is developed in order to be able to compare hybrid position/force control and position-based impedance control in a more complex and a more descriptive task. Therefore, a target trajectory is designed in a way that different kinds of assignments are passed through. Figure 3.10 shows the sequence of all different tasks in a UML state chart. For position-based impedance control, only the desired pose of the TCP  $\mathbf{x}_d$  can be specified, while for hybrid position/force control, a target force/torque vector  $\mathbf{F}_d$  is additionally defined. The compliance selection matrix for hybrid position/force control is set to  $\mathbf{S} = \text{diag}(0, 0, 1, 0, 0, 0)$ . Thus, whenever the TCP is in contact with its environment, only the third element of  $\mathbf{F}_d$  is relevant.

At the beginning, the Stewart platform is supposed to move to a start pose in free space:

$$\mathbf{x}_{\text{start}} = \begin{pmatrix} x_{\text{start}} \\ y_{\text{start}} \\ z_{\text{start}} \\ \alpha_{\text{start}} \\ \beta_{\text{start}} \\ \gamma_{\text{start}} \end{pmatrix}, \mathbf{F}_{\text{start}} = \begin{pmatrix} F_{x,\text{start}} \\ F_{y,\text{start}} \\ F_{z,\text{start}} \\ M_{x,\text{start}} \\ M_{y,\text{start}} \\ M_{z,\text{start}} \end{pmatrix}. \quad (3.15)$$

As soon as the TCP has reached its start pose according to the sensor signals of the resolvers and the force/torque vector, it is further moved to a pose where it is in contact with its environment:

$$\mathbf{x}_{\text{contact}} = \begin{pmatrix} x_{\text{contact}} \\ y_{\text{contact}} \\ z_{\text{contact}} \\ \alpha_{\text{contact}} \\ \beta_{\text{contact}} \\ \gamma_{\text{contact}} \end{pmatrix}, \mathbf{F}_{\text{contact}} = \begin{pmatrix} F_{x,\text{contact}} \\ F_{y,\text{contact}} \\ F_{z,\text{contact}} \\ M_{x,\text{contact}} \\ M_{y,\text{contact}} \\ M_{z,\text{contact}} \end{pmatrix}. \quad (3.16)$$

When arrived at the contact pose, the TCP shall simultaneously follow a trajectory in the  $xy$ -plane specified as a circle with Radius  $R$  and center  $(x_{\text{contact}} + R, y_{\text{contact}})$  and a trajectory along the  $z$ -direction specified as a sine wave around  $z_{\text{contact}}$  with amplitude  $A_z$  and frequency  $f_z$  for the position-based impedance control and around  $F_{z,\text{contact}}$  with amplitude  $A_F$  and frequency  $f_F$  for the hybrid position/force control. The circle is divided into its upper and lower part. The TCP moves along the circle one and a half turns. The sine wave in  $z$ -direction stays unchanged during that time:

$$\mathbf{x}_{\text{first\_upper\_semicircle}}(t) = \begin{pmatrix} x_{\text{contact}} + \frac{2R}{t_{\text{max}}}t \\ y_{\text{contact}} + \sqrt{R^2 - \left(\frac{2R}{t_{\text{max}}}t - R\right)^2} \\ z_{\text{contact}} - A_z \sin(f_z t) \\ \alpha_{\text{contact}} \\ \beta_{\text{contact}} \\ \gamma_{\text{contact}} \end{pmatrix}, \quad (3.17)$$

$$\mathbf{F}_{\text{first\_upper\_semicircle}}(t) = \begin{pmatrix} F_{x,\text{contact}} \\ F_{y,\text{contact}} \\ F_{z,\text{contact}} - A_F \sin(f_F t) \\ M_{x,\text{contact}} \\ M_{y,\text{contact}} \\ M_{z,\text{contact}} \end{pmatrix}, \quad (3.18)$$

$$\mathbf{x}_{\text{lower\_semicircle}}(t) = \begin{pmatrix} x_{\text{contact}} + 2R - \frac{2R}{t_{\text{max}}}t \\ y_{\text{contact}} - \sqrt{R^2 - \left(2R - \frac{2R}{t_{\text{max}}}t - R\right)^2} \\ z_{\text{contact}} - A_z \sin(f_z t) \\ \alpha_{\text{contact}} \\ \beta_{\text{contact}} \\ \gamma_{\text{contact}} \end{pmatrix}, \quad (3.19)$$

$$\mathbf{F}_{\text{lower\_semicircle}}(t) = \mathbf{F}_{\text{first\_upper\_semicircle}}(t), \quad (3.20)$$

$$\mathbf{x}_{\text{second\_upper\_semicircle}}(t) = \mathbf{x}_{\text{first\_upper\_semicircle}}(t), \quad (3.21)$$

$$\mathbf{F}_{\text{second\_upper\_semicircle}}(t) = \mathbf{F}_{\text{first\_upper\_semicircle}}(t), \quad (3.22)$$

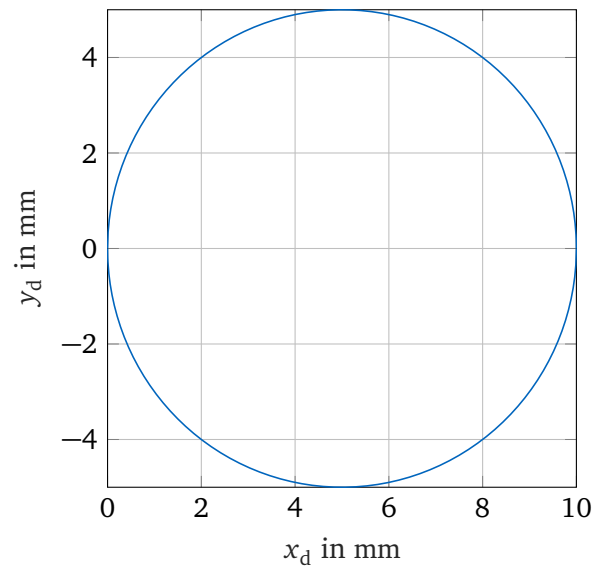
with time  $t \in \{0; T_s; 2T_s; 3T_s; \dots; t_{\max}\}$ , where  $T_s$  is the sample time of the system. As the domain of  $t$  is discrete, interpolation can be applied to receive continuous trajectories. Figure 3.9 shows how the trajectories look like for exemplary values.

When the circle and sine wave trajectories have been accomplished, the TCP finally moves out of the area of contact to an end pose in free space:

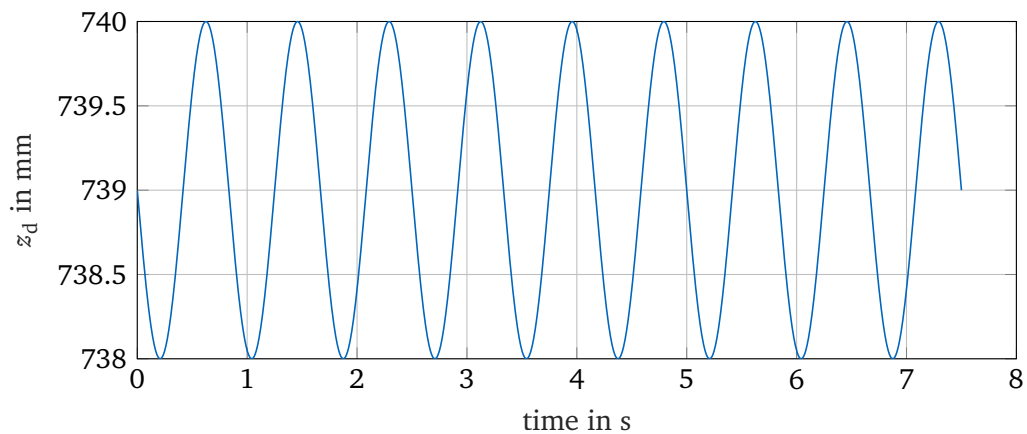
$$\mathbf{x}_{\text{end}} = \begin{pmatrix} x_{\text{end}} \\ y_{\text{end}} \\ z_{\text{end}} \\ \alpha_{\text{end}} \\ \beta_{\text{end}} \\ \gamma_{\text{end}} \end{pmatrix}, \quad \mathbf{F}_{\text{end}} = \begin{pmatrix} F_{x,\text{end}} \\ F_{y,\text{end}} \\ F_{z,\text{end}} \\ M_{x,\text{end}} \\ M_{y,\text{end}} \\ M_{z,\text{end}} \end{pmatrix}. \quad (3.23)$$

The test trajectory is designed to combine different kinds of signal inputs: Heaviside step functions, a sine wave and a circle trajectory. Step functions help to study basic characteristics of the system's transfer behavior, while the sine wave and circle trajectory are used to investigate how well the TCP can follow an arbitrary trajectory. Additionally, the sine wave and circle trajectory are combined to see how the two compliant motion control schemes handle superposed control along different DOFs. On top of that, the start, contact and end poses are chosen in a way that the Stewart platform has to deal with contact-tasks, non-contact tasks and the transition from non-contact tasks to contact-tasks and vice versa.

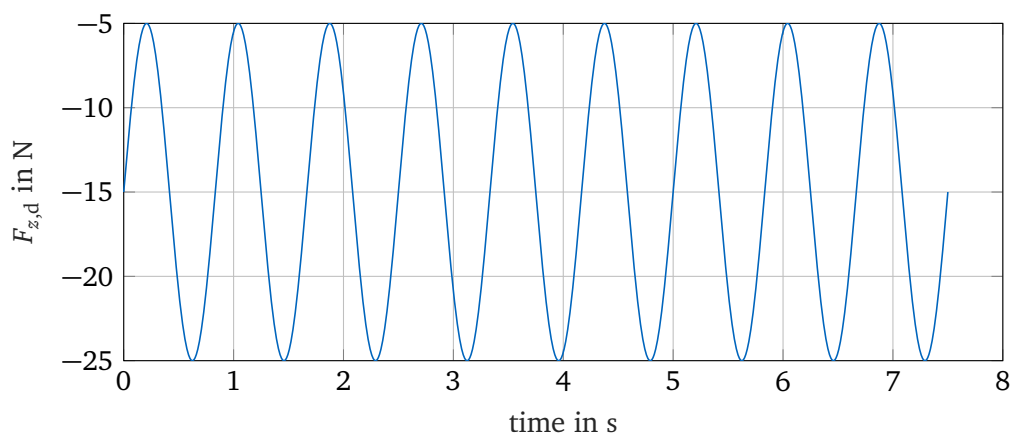




(a) Circle in the  $xy$ -plane with radius  $R = 5$  mm and center  $(5 \text{ mm}, 0 \text{ mm})$



(b) Position along the  $z$ -direction (sine wave around  $z = 739$  mm with amplitude  $A_z = 1$  mm and frequency  $f_z = 2.4\pi$  Hz)



(c) Force along the  $z$ -direction (sine wave around  $F_{z,d} = -15$  N with amplitude  $A_z = 10$  N and frequency  $f_z = 2.4\pi$  Hz)

**Figure 3.9:** Target position and force trajectories with the test trajectory test case

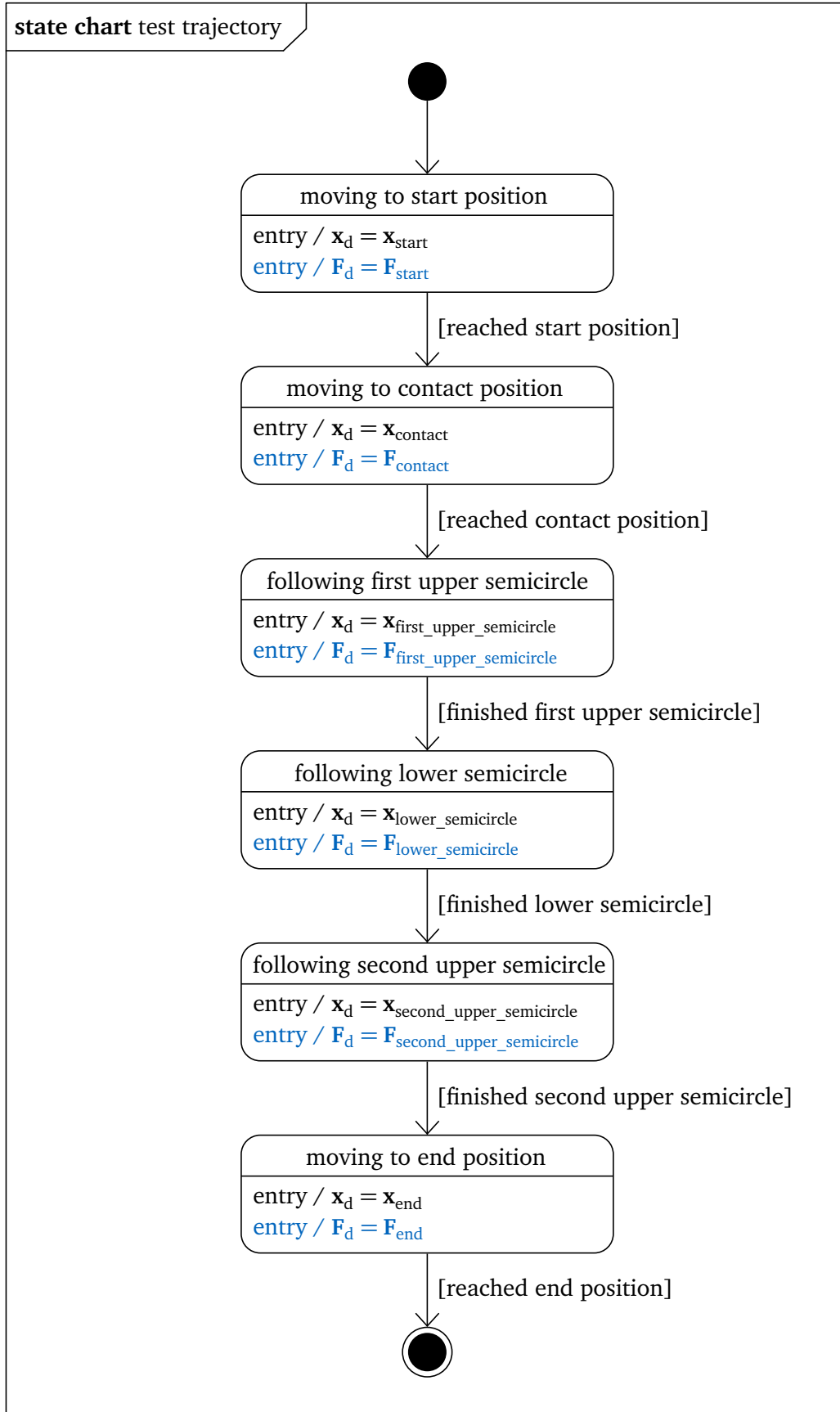


Figure 3.10: State chart of the test trajectory

## Chapter 4

# Design of Controller Parameters, Testing and Validation

In the following chapter, we study the concepts developed in chapter 3 in practice. We start by examining some preliminary problems in section 4.1 which have to be solved before being able to concentrate on testing. Then, in section 4.2 we investigate hybrid position/force control in terms of its control parameters and its behavior when switching from a non-contact tasks to a contact task and vice versa. In section 4.3 we focus on the tuning of control parameters for position-based impedance control and their effect on the system's step response. Finally, in section 4.4 we compare hybrid position/force control with position-based impedance control in terms of their influence on system behavior, computational costs and when applying the control schemes along other DOFs of the Stewart platform. In most of the tests, we use the experimental setup shown in fig. 2.10. Only for the ones of the last subsection, we apply another lower mass, illustrated in fig. 3.1, because of further development on the support that took place parallel to the experiments in the context of this thesis. However, this does not change the behavior of robot-environment interaction in comparison to the other lower mass. Overall, the experimental setup is best suitable to execute tests along the  $z$ -direction of the Stewart platform as the compression spring typically transfers forces along that direction. Also, by modeling the environment with the help of the spring and being aware of its stiffness, we know how the environment behaves for  $t \rightarrow \infty$  for a certain excitation. In order to be able to properly test along other DOFs of the Stewart platform, we would have to install springs also along these DOFs. All following tests are based on the test cases introduced in section 3.5. Furthermore, in the context of this thesis, we only want to tune controller parameters experimentally and not theoretically. For simplicity, we consider the performance of the existing independent joint controller to be the optimal one and use it as a reference to adjust the control parameters of the compliant motion control schemes. Besides, we always choose the same control parameter values for all DOFs of the Stewart platform because we want to treat all DOFs equally. Whenever we want to compare hybrid position/force control with independent joint control or position-based impedance control, we need to specify target forces and torques on top of target poses of the TCP. Therefore, we define a target pose, move the TCP to this pose, measure the actual force/torque values and take the average over a sufficient number of sample steps to receive the corresponding target force/torque values. We could also first specify target force/torque values, move the TCP to a pose where these values are measured, determine the leg lengths of the Stewart platform and compute the TCP's pose in workspace by means of forward kinematics to get the corresponding target pose. We avoid this alternative approach in order to prevent using Newton's method as it is only an approximation of the real pose of the TCP. All results we receive and all statements we make during this chapter, are strictly speaking only true for the area in workspace used for the corresponding test because the Stewart platform is a nonlinear sys-

tem. However, we always equally carry out tests when directly comparing multiple aspects. Moreover, the choice of control parameter always depends on the specific manipulator and its environment. Thus, the aim of the following tests is to show general characteristics, benefits and drawbacks of hybrid position/force control and respectively position-based impedance control instead of finding perfect control parameters.

## 4.1 Preliminary Investigations

Before performing tests on the control schemes, we look at two different aspects which directly influence performance of control. On the one hand, we investigate the effect of signal smoothing within data processing of the force/torque sensor signal and on the other hand, we check to which extent forward kinematics can approximate the real pose of the TCP.

### Signal Smoothing

Section 3.2 already described the need for signal smoothing as a part of data preparation of the force/torque sensor signal and introduced the concept of moving average. Here, we want to demonstrate its effect on the measured force signal for an appropriate window length. Therefore, we set the force/torque offset at position

$$\mathbf{x} = ( 0 \text{ mm} \quad 0 \text{ mm} \quad 733 \text{ mm} \quad 0 \text{ rad} \quad 0 \text{ rad} \quad 0 \text{ rad} )^T \quad (4.1)$$

and present a sine wave position reference trajectory in  $z$ -direction with amplitude 5 mm and frequency 0.2 Hz to the system. The existing individual joint control is applied. Figure 4.1 shows the resulting plots for the measured and adjusted force  $F_z$  without signal smoothing as well as with signal smoothing setting the window length to 3.

Comparing the two plots, we observe that introducing moving average with a window length of 3 leads to less noise in the force signal  $F_z$ . Still, it does not distort the sequence of force values as the shape of the expected sine wave is preserved. Finding appropriate parameters for filtering methods is always a trade-off between good signal smoothing, i.e. noise and outlier reduction and low delay as filtering always adds a phase delay to the system. For the existing Stewart platform, a window length of 3 seems appropriate and is therefore used in all following tests.

### Forward Kinematics

In the following tests, we investigate the Stewart platform's response to different input desired trajectories. Therefore, we often look at the actual pose of the TCP in workspace coordinates in order to be able to directly compare it to the desired trajectory which is always specified in workspace coordinates. As a result, we need to apply forward kinematics for this analysis. Besides, hybrid position/force control also makes use of forward kinematics. Thus, the parameters in Newton's method explained in section 2.3.2 have to be adequately chosen to ensure that the forward kinematics algorithm approximates the pose of the TCP with high accuracy.

To rate the performance of the algorithm, we apply independent joint control to move the TCP of the Stewart platform to the arbitrary pose

$$\mathbf{x}_d = ( 0 \text{ mm} \quad 0 \text{ mm} \quad 738 \text{ mm} \quad 0 \text{ rad} \quad 0 \text{ rad} \quad 0 \text{ rad} )^T, \quad (4.2)$$

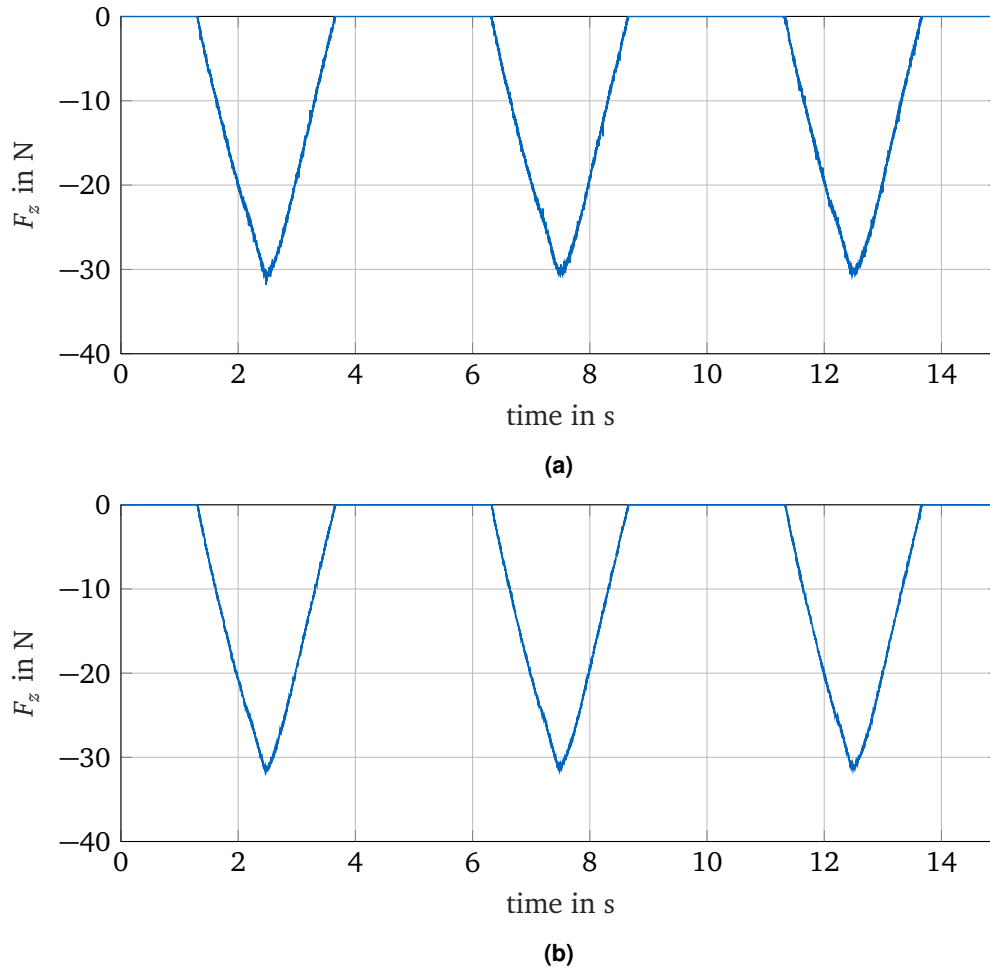


**Figure 4.1:** Measured force  $F_z$  (a) without signal smoothing and (b) with signal smoothing using the moving average approach with a window length equal to 3

measure its leg lengths  $\mathbf{b}$ , take the average of the elements in  $\mathbf{b}$  from 1000 sample points and apply Newton's method for the initial guess

$$\mathbf{x}_0 = \left( 0 \text{ mm} \quad 0 \text{ mm} \quad 727 \text{ mm} \quad 0 \text{ rad} \quad 0 \text{ rad} \quad 0 \text{ rad} \right)^T \quad (4.3)$$

for a maximum number of iterations  $k_{\max} = 100$ . First, we set the user-defined acceptable maximum approximation error  $\epsilon_{\text{tol}} = 1 \cdot 10^{-6} \mu\text{m}$ . In accordance with eq. (2.20), the algorithm converges to

$$\mathbf{x} = \begin{pmatrix} 0.0044 \text{ mm} \\ 0.0085 \text{ mm} \\ 738.0030 \text{ mm} \\ 1.4055 \cdot 10^{-5} \text{ rad} \\ 9.1215 \cdot 10^{-6} \text{ rad} \\ 3.2201 \cdot 10^{-5} \text{ rad} \end{pmatrix} \quad (4.4)$$

after four iterations. The value for  $\epsilon_{\text{tol}}$  is so small that we can interpret  $\mathbf{x}$  to be the actual correct pose of the TCP. Note, that it differs from  $\mathbf{x}_d$  primarily because of inaccuracy of the independent joint control as well as inaccuracy resulting from elasticity in the belts of the Stewart platform. Now, we repeat the computation for a more realistic acceptable maximum

approximation error  $\epsilon_{\text{tol}} = 23 \mu\text{m}$ . Then the algorithm converges to

$$\mathbf{x}_{\text{approx}} = \begin{pmatrix} 0.0043 \text{ mm} \\ 0.0083 \text{ mm} \\ 738.0089 \text{ mm} \\ 1.4070 \cdot 10^{-5} \text{ rad} \\ 9.1285 \cdot 10^{-6} \text{ rad} \\ 3.1630 \cdot 10^{-5} \text{ rad} \end{pmatrix} \quad (4.5)$$

after two iterations. So, the absolute error in each direction of vector  $\mathbf{x}_{\text{approx}}$  that is made when choosing  $\epsilon_{\text{tol}} = 23 \mu\text{m}$  is

$$|\mathbf{x} - \mathbf{x}_{\text{approx}}| = \begin{pmatrix} 0.0001 \text{ mm} \\ 0.0002 \text{ mm} \\ 0.0069 \text{ mm} \\ 0.0015 \cdot 10^{-5} \text{ rad} \\ 0.0070 \cdot 10^{-6} \text{ rad} \\ 0.0571 \cdot 10^{-5} \text{ rad} \end{pmatrix}. \quad (4.6)$$

As the approximated pose vector  $\mathbf{x}_{\text{approx}}$  is accurate enough, we will use  $\epsilon_{\text{tol}} = 23 \mu\text{m}$  due to the manufacturing tolerances mentioned in section 2.3.2. A lower limit would not make sense because of inaccuracy resulting from elasticity in the belts of the Stewart platform and because we need to ensure that the computation time for the Newton-iterations does not exceed the systems sample time of 1 ms. Although forward kinematics will not equally perform in different areas of the Stewart platform's workspace, we assume that, according to eq. (4.6), we can trust position values with accuracy  $10 \mu\text{m}$  and orientation values with accuracy  $\frac{1}{1000000}$  rad, although the values may practically be too low for a real physical system with measurement and computation inaccuracies. Furthermore, we choose  $k_{\text{max}} = 5$  as even for  $\epsilon_{\text{tol}} = 1 \cdot 10^{-6} \mu\text{m}$ , the algorithm converges after four iterations.

### Settings for Testing

Table 4.1 specifies values for all parameters investigated in the latter paragraphs as well as for all user-defined parameters applied during data processing and control. We use those values in all following tests if not declared differently in the context of a specific test case.

## 4.2 Testing on Hybrid Position/Force Control

In this section, we focus on testing hybrid position/force control. Therefore, we firstly tune its control parameters in section 4.2.1. Thereafter, in section 4.2.2, we test the behavior of hybrid position/force control when switching between a contact-task and a non-contact task.

### 4.2.1 Design of Hybrid Position/Force Controller Parameters

Before being able to work with the hybrid position/force controller, we need to tune its parameters. As described in section 3.3, it consists of a position, force and velocity controller. The latter one has been designed in a way that the velocity controller of the independent joint control can be reused. Thus, we take the parameter values from the independent joint controller and set  $K_{p,v,i} = K_{p,v} = 0.2 \frac{\text{Vs}}{\text{mm}}$  and  $K_{I,v,i} = K_{I,v} = 1 \frac{\text{V}}{\text{mm}} \forall i = 1 \dots 6$  in eq. (3.9). We

**Table 4.1:** Parameter values used during testing

parameter	value	explanation
sample time $T_s$	1 ms	section 2.3.2
window length for moving average	3	section 3.2, section 4.1
$\theta$ for coordinate transformation	120°	section 3.2
threshold for ignoring values close to 0	2 N, $\frac{2}{13}$ Nm	section 3.2
$\epsilon_{\text{tol}}$ in forward kinematics	23 $\mu\text{m}$	section 2.3.2, section 4.1
$k_{\text{max}}$ in forward kinematics	5	section 2.3.2, section 4.1
$\dot{b}_{\text{max}}$ in all control schemes	20 $\frac{\text{mm}}{\text{s}}$	section 2.3.2, section 3.3 section 3.4
$i_{\text{max}}$ in all control schemes	3 A	section 2.3.2, section 3.3 section 3.4
$K_{p,p}$ in independent joint control	20 $\frac{1}{\text{s}}$	section 2.3.2
$K_{p,v}$ in independent joint control	0.2 $\frac{\text{Vs}}{\text{mm}}$	section 2.3.2
$K_{I,v}$ in independent joint control	1 $\frac{\text{V}}{\text{mm}}$	section 2.3.2

use the variables  $K_{p,v}$  and  $K_{I,v}$  for simplicity and to stress that we choose the parameters for all DOFs equally because we do not want to treat the DOFs of the Stewart platform differently as explained above. The tuning of the remaining parameters is separately and experimentally done for the position and force controller in the following paragraphs.

### Design of Position Controller Parameters

For correctly tuning the parameters  $K_{p,p,i}$  of the position controller within hybrid position/force control, we need to specify a task in which only the position controller and not the force controller influences the Stewart platform's behavior. This is the case in non-contact tasks, i.e. when measured interaction force and torque values are zero apart from noise in the real measurement. Thus, during this test, we use poses for which the TCP can move freely without contacting its environment. This means that the upper mass in fig. 2.11 may not touch any contact surface. Therefore, we use the step response analysis presented in section 3.5 with following target pose vectors:

$$\mathbf{x}_{\text{start}} = \begin{pmatrix} 0 \text{ mm} \\ 0 \text{ mm} \\ 720 \text{ mm} \\ 0 \text{ rad} \\ 0 \text{ rad} \\ 0 \text{ rad} \end{pmatrix}, \quad \mathbf{x}_{\text{end}} = \begin{pmatrix} 0 \text{ mm} \\ 0 \text{ mm} \\ 723 \text{ mm} \\ 0 \text{ rad} \\ 0 \text{ rad} \\ 0 \text{ rad} \end{pmatrix}. \quad (4.7)$$

The initial guess for the forward kinematics algorithm is arbitrary set to:

$$\mathbf{x}_0 = \begin{pmatrix} 0 \text{ mm} \\ 0 \text{ mm} \\ 716 \text{ mm} \\ 0 \text{ rad} \\ 0 \text{ rad} \\ 0 \text{ rad} \end{pmatrix}. \quad (4.8)$$

Again, we choose same values for all elements of the P-controller transfer function matrix  $C_p(z)$  in eq. (3.4) and eq. (3.5) to treat all DOFs equally:

$$K_{p,p,i} = K_{p,p} \quad \forall i \in \{x, y, z, \alpha, \beta, \gamma\}. \quad (4.9)$$

We repeat the test for multiple values  $K_{p,p}$  and display the resulting position in  $z$ -direction of the TCP computed by Newton's method in fig. 4.2. The plots also show the result for the test using the currently implemented independent joint control as well as the target position of the TCP  $z_d$ .

Figure 4.2b shows the results that are close to the one for independent joint control, whereas fig. 4.2a presents curves for smaller and fig. 4.2c for larger values  $K_{p,p}$ . In general, the step responses have the same shape, but settling time decreases for larger control parameter values and for roughly  $K_{p,p} \leq 150 \frac{1}{s}$  overshooting can be observed. However, the latter effect is small. For  $K_{p,p} = 250 \frac{1}{s}$  the overshoot value is around 0.02 mm which is close to the maximum accuracy achieved by Newton's method  $\epsilon_{tol} = 23 \mu\text{m}$  and thus not that relevant. However, we want our position controller to be robust and realize a trade-off between fast reaction and accuracy. As we consider the behavior of the independent joint controller being optimal in terms of this trade-off, we choose  $K_{p,p} = 20 \frac{1}{s}$  because the corresponding step response fits the one of independent joint control. Additionally, the control output signals look fine and do not show any undesired effects. Hence, the control parameters of the position controller are the same for both the operational space control like for the hybrid position/force controller and the joint space control like in the case of independent joint control.

#### Design of Force Controller Parameters

Next, we want to find parameter values for the force controller within hybrid position/force control. We proceed analog to the former test case, but this time, we need to specify the test as a contact-task in order to be able to measure interaction forces as an input for the force controller. As we are now using data from the force/torque sensor, we need to set the force/torque offset and therefore choose the position

$$\mathbf{x} = (0 \text{ mm} \quad 0 \text{ mm} \quad 737 \text{ mm} \quad 0 \text{ rad} \quad 0 \text{ rad} \quad 0 \text{ rad})^T. \quad (4.10)$$

We specify the following vectors for the target poses of the TCP and the initial guess for the forward kinematics algorithm:

$$\mathbf{x}_{\text{start}} = \begin{pmatrix} 0 \text{ mm} \\ 0 \text{ mm} \\ 738 \text{ mm} \\ 0 \text{ rad} \\ 0 \text{ rad} \\ 0 \text{ rad} \end{pmatrix}, \quad \mathbf{x}_{\text{end}} = \begin{pmatrix} 0 \text{ mm} \\ 0 \text{ mm} \\ 741 \text{ mm} \\ 0 \text{ rad} \\ 0 \text{ rad} \\ 0 \text{ rad} \end{pmatrix}, \quad \mathbf{x}_0 = \begin{pmatrix} 0 \text{ mm} \\ 0 \text{ mm} \\ 734 \text{ mm} \\ 0 \text{ rad} \\ 0 \text{ rad} \\ 0 \text{ rad} \end{pmatrix}. \quad (4.11)$$



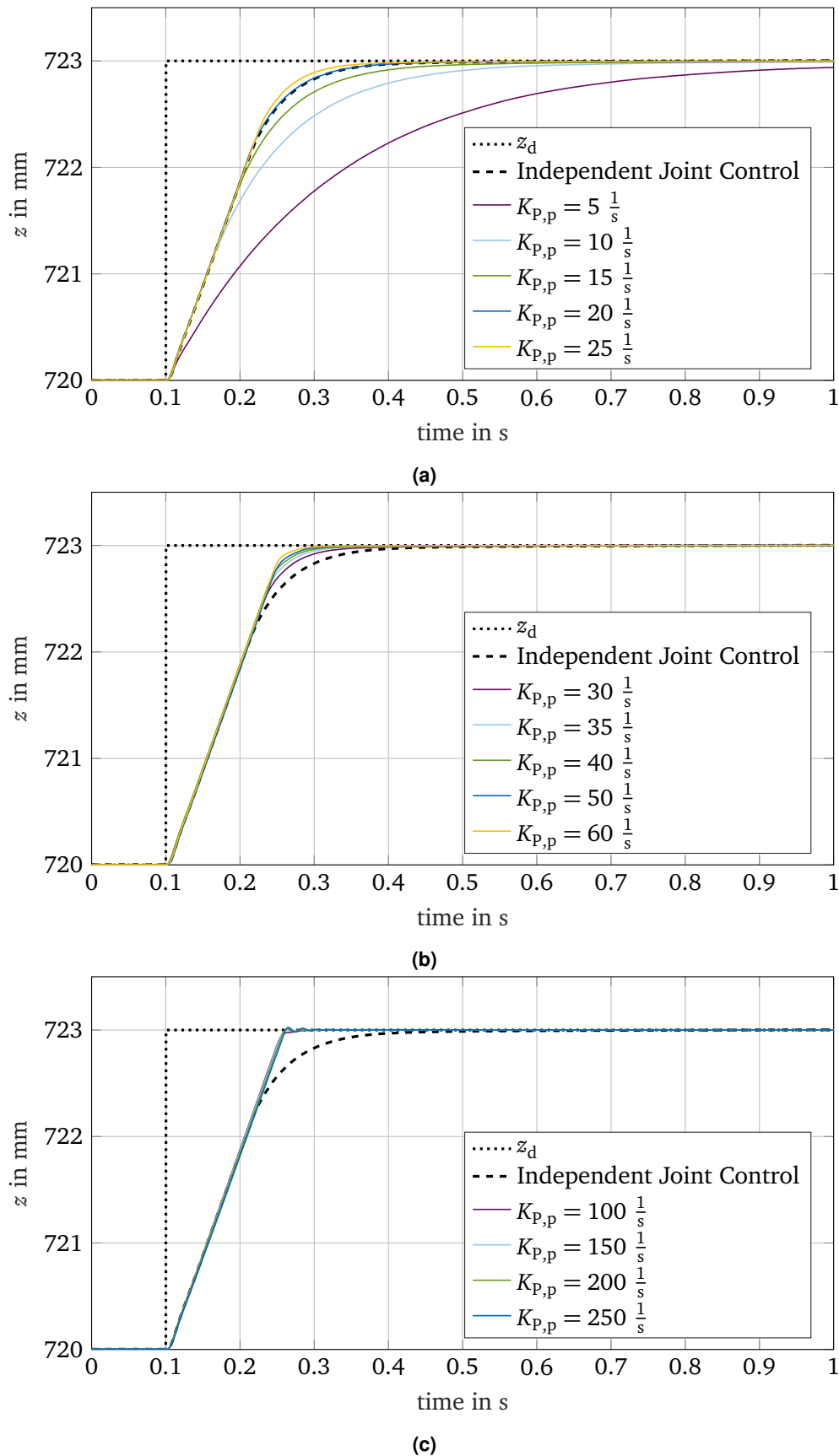


**Figure 4.2:** Comparison of step responses applying independent joint control and hybrid position/force control in a non-contact task when varying  $K_{p,p}$  (a) from  $5 \frac{1}{s}$  to  $25 \frac{1}{s}$ , (b) from  $30 \frac{1}{s}$  to  $60 \frac{1}{s}$  and (c) from  $100 \frac{1}{s}$  to  $250 \frac{1}{s}$

As described in the introductory part of the chapter, we concentrate on the robot-environment interaction in  $z$ -direction, thus we define the following compliance selection matrix:

$$\mathbf{S} = \text{diag}(001000). \quad (4.12)$$

As a result, the third element of  $\mathbf{x}_{\text{end}}$  is only needed for independent joint control. For hybrid position/force control we have to determine an appropriate force value. Therefore, we measure  $F_z$  at the position  $\mathbf{x}_{\text{end}}$  and take the average over 12000 sample steps. This leads to the following target force/torque vector:

$$\mathbf{F}_{\text{end}} = \begin{pmatrix} 0 \text{ N} \\ 0 \text{ N} \\ -34.60 \text{ N} \\ 0 \text{ Nm} \\ 0 \text{ Nm} \\ 0 \text{ Nm} \end{pmatrix}. \quad (4.13)$$

By this, we can directly compare the step responses for hybrid position/force control with the one when applying independent joint control. Again, we choose same values for all elements of the P-controller transfer function matrix  $\mathbf{C}_F(z)$  in eq. (3.6) and eq. (3.7) to treat all DOFs equally:

$$K_{p,F,i} = K_{p,F} \quad \forall i \in \{x, y, z, \alpha, \beta, \gamma\}. \quad (4.14)$$

We repeat the test for multiple values  $K_{p,F}$  and display the resulting measured interaction forces in  $z$ -direction in fig. 4.3. The plots also include the result when applying the currently implemented independent joint control as well as the target force  $F_{z,d}$ . Note, that the specification of the unit of  $K_{p,F}$  means that we distinguish between  $\frac{\text{mm}}{\text{Ns}}$  for forces and  $\frac{\text{rad}}{\text{Nm}\cdot\text{s}}$  for torques.

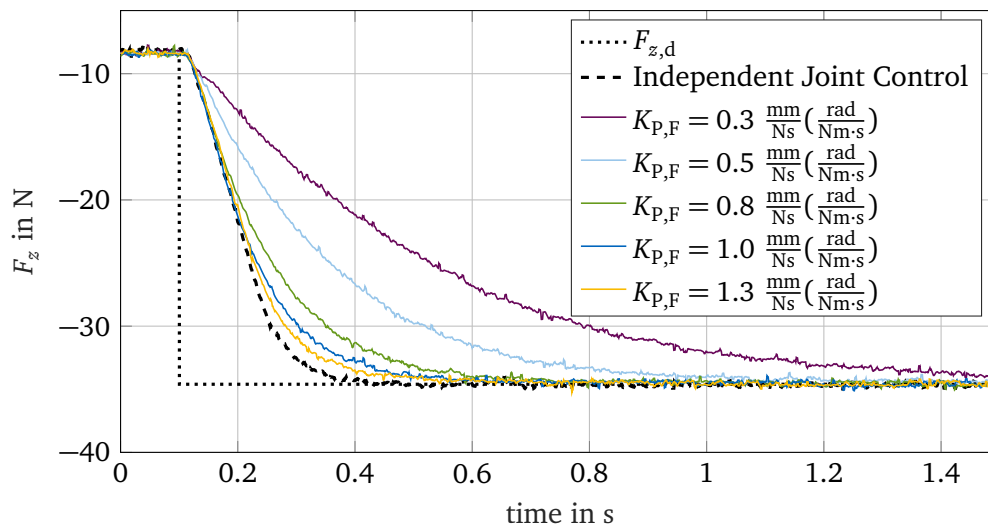
In analogy to fig. 4.2 we investigate control parameter values that lead to curves close to the one when applying independent joint control in fig. 4.3b as well as smaller values in fig. 4.3a and larger values in fig. 4.3c. All curves have basically the same shape and contain noise because they are real measurement data. Again, larger values  $K_{p,F}$  result in a smaller settling time, but for approximately  $K_{p,F} > 3.0 \frac{\text{mm}}{\text{Ns}} (\frac{\text{rad}}{\text{Nm}\cdot\text{s}})$  overshooting occurs. Again, we consider the step response for independent joint control to be optimal in terms of the trade-off between fast reaction and accuracy. Thus, we may choose a value between  $1.5 \frac{\text{mm}}{\text{Ns}} (\frac{\text{rad}}{\text{Nm}\cdot\text{s}})$  and  $1.9 \frac{\text{mm}}{\text{Ns}} (\frac{\text{rad}}{\text{Nm}\cdot\text{s}})$  for the control parameter as the curves are very close to each other in this interval. For following tests and usage of the hybrid position/force control, we set  $K_{p,F} = 1.8 \frac{\text{mm}}{\text{Ns}} (\frac{\text{rad}}{\text{Nm}\cdot\text{s}})$ . The corresponding control output signals are also reasonable in a way that they do not show any undesirable effects.

#### Overview of Control Parameters of Hybrid Position/Force Control

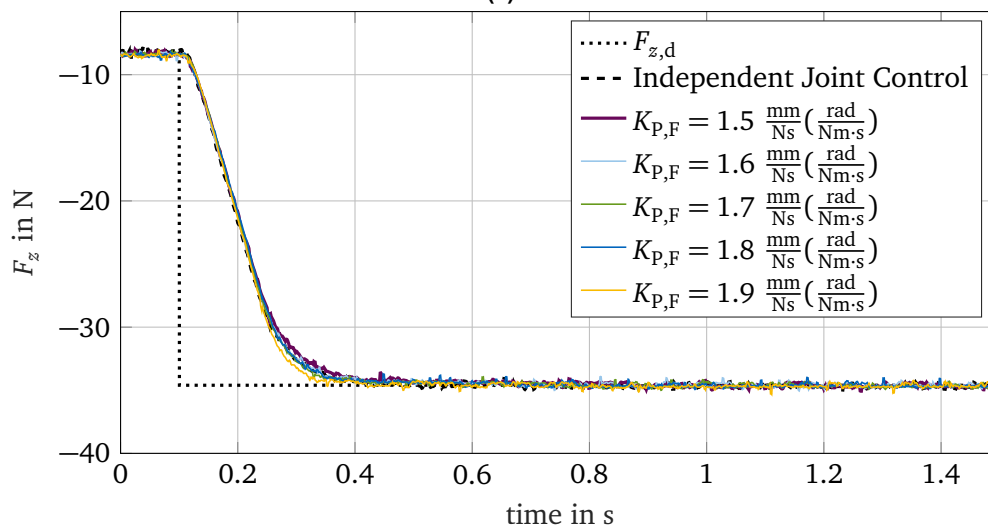
Table 4.2 sums up all control parameters of hybrid position/force control that have been determined during the former test cases. They are used for further testing and usage of the control approach on the Stewart platform.

#### 4.2.2 Testing on Switch between Position and Force Control

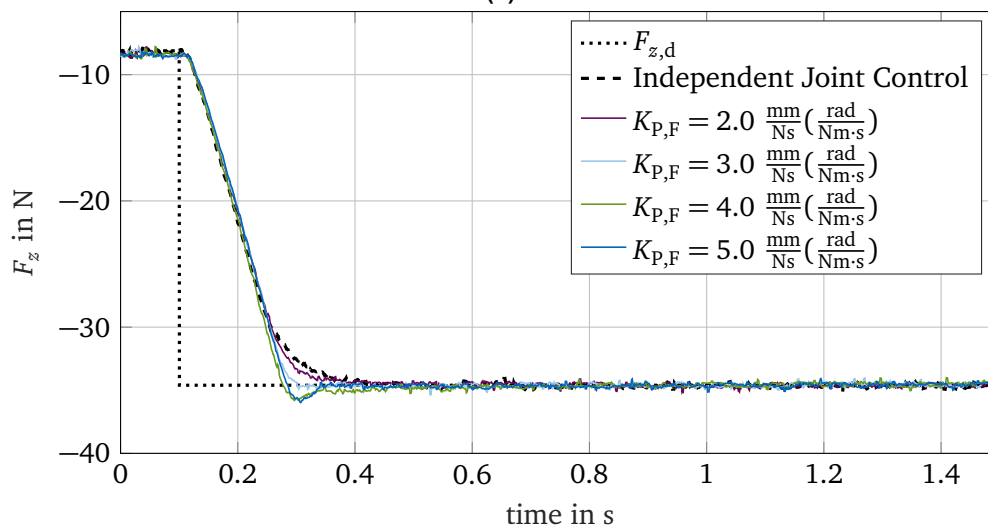
The difficult part of hybrid position/force control is that the scheme itself has to decide whether to control a DOF by position or force control based on the user-defined compliance



(a)



(b)



(c)

**Figure 4.3:** Comparison of step responses applying independent joint control and hybrid position/force control in a contact task when varying  $K_{p,F}$  (a) from  $0.3 \frac{\text{mm}}{\text{Ns}} \left( \frac{\text{rad}}{\text{Nm}\cdot\text{s}} \right)$  to  $1.3 \frac{\text{mm}}{\text{Ns}} \left( \frac{\text{rad}}{\text{Nm}\cdot\text{s}} \right)$ , (b) from  $1.5 \frac{\text{mm}}{\text{Ns}} \left( \frac{\text{rad}}{\text{Nm}\cdot\text{s}} \right)$  to  $1.9 \frac{\text{mm}}{\text{Ns}} \left( \frac{\text{rad}}{\text{Nm}\cdot\text{s}} \right)$  and (c) from  $2.0 \frac{\text{mm}}{\text{Ns}} \left( \frac{\text{rad}}{\text{Nm}\cdot\text{s}} \right)$  to  $5.0 \frac{\text{mm}}{\text{Ns}} \left( \frac{\text{rad}}{\text{Nm}\cdot\text{s}} \right)$

**Table 4.2:** Control parameters of hybrid position/force control

parameter	value
$K_{P,v}$	$0.2 \frac{Vs}{mm}$
$K_{I,v}$	$1 \frac{V}{mm}$
$K_{P,p}$	$20 \frac{1}{s}$
$K_{P,F}$	$1.8 \frac{mm}{Ns} (\frac{rad}{Nm \cdot s})$

selection matrix and the actual force/torque measurements leading to a contact matrix. The relationship has been derived in eq. (3.10). Problematic herein is that sensor measurements contain noise and therefore are adjusted by an approach that ignores values close to 0 and has been introduced in section 3.2. This ensures that an element in the contact matrix is only equal to 1 if the TCP is definitely in contact with its environment along the corresponding DOF and thus, alternate changes in the elements of the contact and consequently the position and force selection matrices are avoided. We want to have a look at the behavior of the hybrid position/force control when the contact matrix changes during control actions. As we concentrate on interaction forces only along one DOF, the problem can be seen as a switch from a non-contact task to a contact task or vice versa. In the following, we investigate both cases. Although section 3.2 has already explained why we want to apply the subtraction approach for the Stewart platform, we still try both approaches of fig. 3.4 in the second test of this section in order to illustrate their differences.

#### Switch from Non-Contact Task to Contact Task

Again, we perform a step response analysis and therefore move the TCP from a pose where it is not in contact with its environment:

$$\mathbf{x}_{\text{start}} = \begin{pmatrix} 0 \text{ mm} \\ 0 \text{ mm} \\ 733 \text{ mm} \\ 0 \text{ rad} \\ 0 \text{ rad} \\ 0 \text{ rad} \end{pmatrix} \quad (4.15)$$

to a pose where it touches the upper metal plate:

$$\mathbf{x}_{\text{end}} = \begin{pmatrix} 0 \text{ mm} \\ 0 \text{ mm} \\ 741 \text{ mm} \\ 0 \text{ rad} \\ 0 \text{ rad} \\ 0 \text{ rad} \end{pmatrix}. \quad (4.16)$$

Herein, we set the force/torque offset at the pose

$$\mathbf{x} = (0 \text{ mm} \ 0 \text{ mm} \ 737 \text{ mm} \ 0 \text{ rad} \ 0 \text{ rad} \ 0 \text{ rad})^T. \quad (4.17)$$

Additionally, we anew concentrate on the  $z$ -direction of the Stewart platform and therefore define the following compliance selection matrix:

$$\mathbf{S} = \text{diag}(001000). \quad (4.18)$$

Thus, like in the test before, the third element of  $\mathbf{x}_{\text{end}}$  is only needed for independent joint control. So, for hybrid position/force control we determine an appropriate force value by measuring  $F_z$  at the position  $\mathbf{x}_{\text{end}}$  and take the average over 20000 sample steps. This leads to the following target force/torque vector:

$$\mathbf{F}_{\text{end}} = \begin{pmatrix} 0 \text{ N} \\ 0 \text{ N} \\ -32.71 \text{ N} \\ 0 \text{ Nm} \\ 0 \text{ Nm} \\ 0 \text{ Nm} \end{pmatrix}. \quad (4.19)$$

Once again, we investigate the step responses in workspace and therefore apply Newton's method with the initial guess

$$\mathbf{x}_0 = \begin{pmatrix} 0 \text{ mm} \\ 0 \text{ mm} \\ 734 \text{ mm} \\ 0 \text{ rad} \\ 0 \text{ rad} \\ 0 \text{ rad} \end{pmatrix} \quad (4.20)$$

to compute the actual pose of the TCP.

Figure 4.4 shows the step response for independent joint control compared to the one for hybrid position/force control in terms of the approximated position  $z$  and measured force  $F_z$  as well as the corresponding target input signals  $z_d$  and  $F_{z,d}$ . For hybrid position/force control, we use the control parameters determined in the latter sections.

Note, that because we set the offset at  $z = 737$  mm and because we chose the threshold for ignoring values close to 0 due to the subtraction approach to 2 N and  $\frac{2}{13}$  Nm respectively, the third element on the diagonal of the contact matrix of the hybrid position/force control switches from 0 to 1 at roughly  $z = 737.2$  mm according to the stiffness of the environment  $k_E = 10000 \frac{\text{N}}{\text{m}}$ . Correspondingly, at this position, we start to observe a contact force larger than zero in fig. 4.4b. As a result, at  $z = 737.2$  mm, the control mode along the  $z$ -direction of the Stewart platform switches from position control to force control within hybrid position/force control.

In terms of both position and force tracking, hybrid position/force control performs as well as independent joint control. Also along the other DOFs, both control approaches meet their requirements. The corresponding plots are not included here, as they only show that position/orientation and force/torque values remain zero. This means that in this test case, hybrid position/force control can handle moving from a non-contact pose to a contact pose along  $z$ -direction without any problems.

### Switch from Contact Task to Non-Contact Task

Next, we examine the reverse problem, i.e. moving from a pose where the TCP is in contact with the upper metal plate to a pose where the TCP is in free space. We reuse all parameters from the former test, but change start and end values of the target pose and force/torque

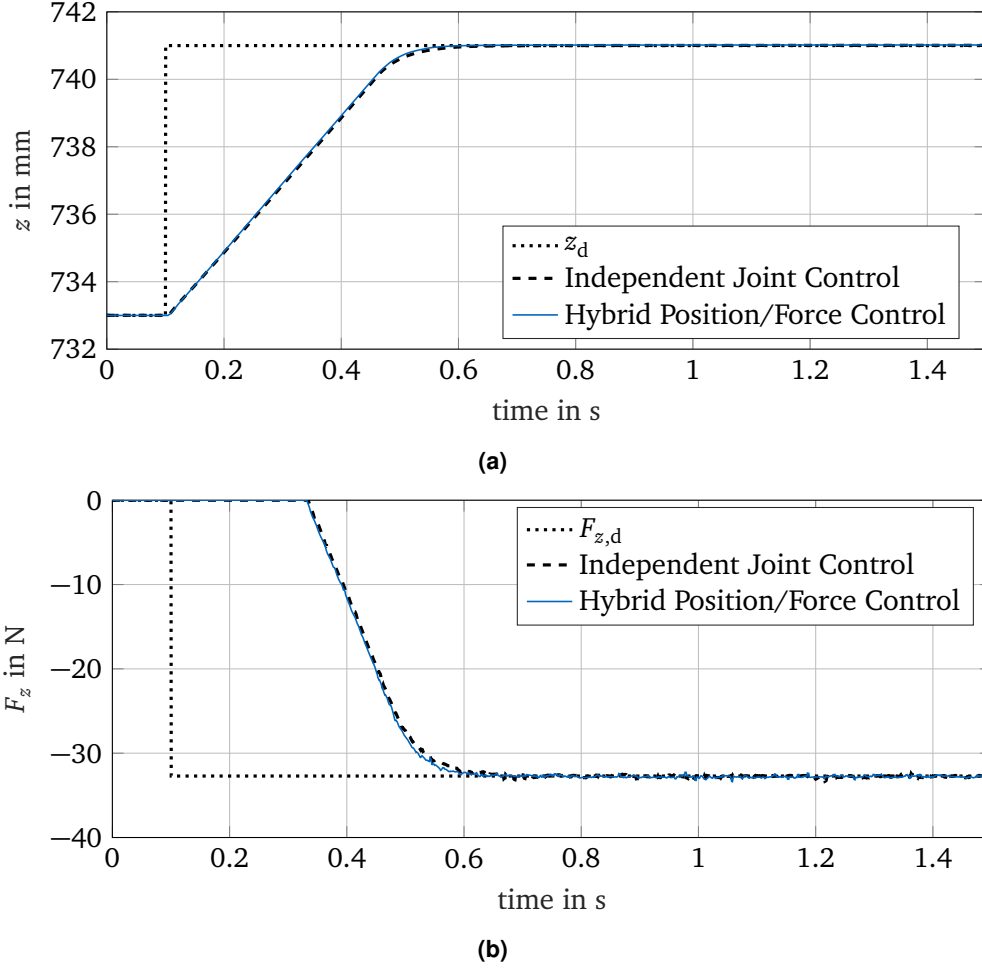


**Figure 4.4:** Comparison of step responses applying independent joint control and hybrid position/force control when switching from a non-contact task to a contact task along (a) position  $z$  and (b) force  $F_z$

vector:

$$\mathbf{x}_{\text{start}} = \begin{pmatrix} 0 \text{ mm} \\ 0 \text{ mm} \\ 741 \text{ mm} \\ 0 \text{ rad} \\ 0 \text{ rad} \\ 0 \text{ rad} \end{pmatrix}, \quad \mathbf{x}_{\text{end}} = \begin{pmatrix} 0 \text{ mm} \\ 0 \text{ mm} \\ 733 \text{ mm} \\ 0 \text{ rad} \\ 0 \text{ rad} \\ 0 \text{ rad} \end{pmatrix}. \quad (4.21)$$

As the end position is a non-contact pose, we set the desired end force to zero for hybrid position/force control:

$$\mathbf{F}_{\text{end}} = \begin{pmatrix} 0 \text{ N} \\ 0 \text{ N} \\ 0 \text{ N} \\ 0 \text{ Nm} \\ 0 \text{ Nm} \\ 0 \text{ Nm} \end{pmatrix}. \quad (4.22)$$

Figure 4.5 shows the corresponding position and force step response along the  $z$ -direction of the Stewart platform.

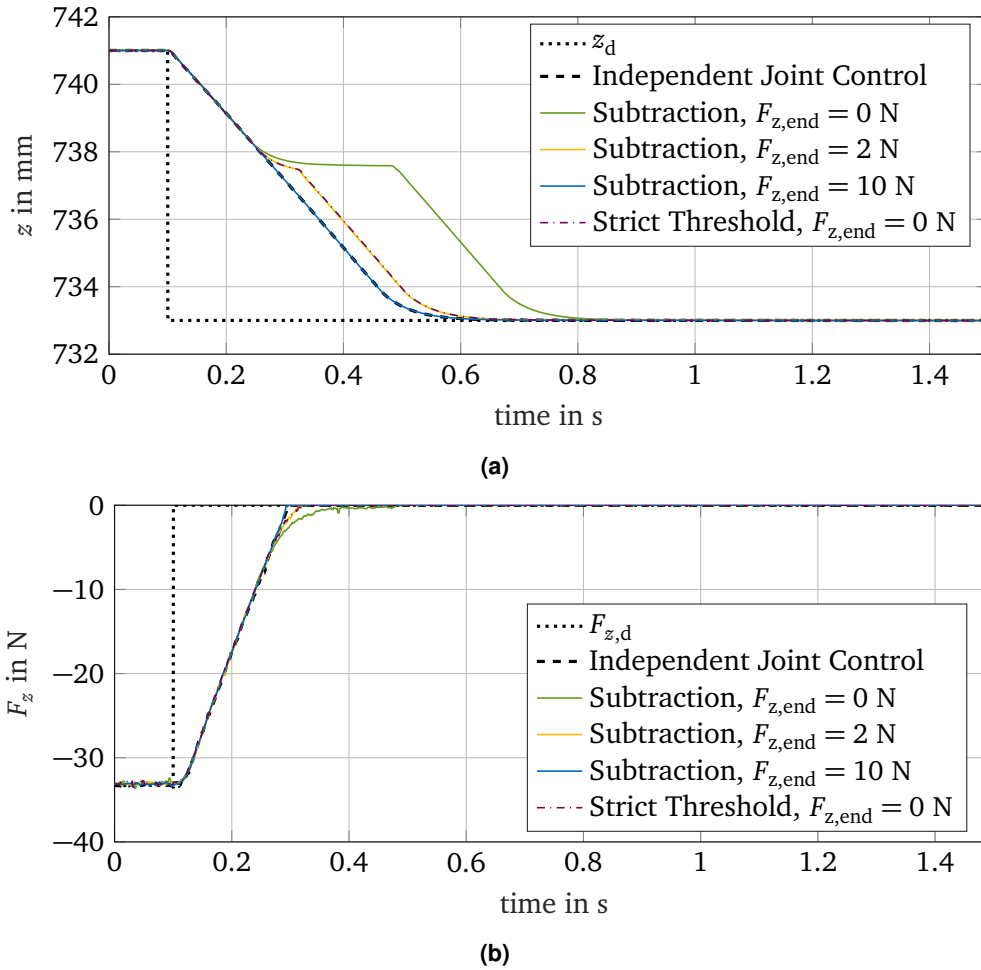


**Figure 4.5:** Comparison of step responses applying independent joint control and hybrid position/force control when switching from a contact task to a non-contact task along (a) position  $z$  and (b) force  $F_z$

At first, we concentrate on the curves for  $F_{z,end} = 0$  N. These are the step responses resulting from choosing  $F_{end}$  as specified in eq. (4.22), on the one hand using the subtraction approach for ignoring measured force/torque values close to 0 and on the other hand using a strict threshold during data processing according to section 3.2. Both perform worse than independent joint control, but the subtraction approach is even worse. The reason for this is that as long as the TCP is in contact with the upper metal plate, the measured force  $F_z$  is unequal to zero and thus the force selection matrix  $\mathbf{S}_F$  is equal to the user-defined compliance selection matrix  $\mathbf{S} = \text{diag}(001000)$  due to eq. (3.10). Not before  $F_z = 0$  N, the contact matrix  $\mathbf{S}_c$  as well as the force selection matrix  $\mathbf{S}_F$  become zero matrices. As a result, the control scheme forces the TCP to asymptotically reach the pose where  $F_z = 0$  N, before further position-controlling it towards the end pose  $\mathbf{x}_{end}$ . The end position of force control, i.e. the position where  $F_z = 0$  N, is theoretically at  $z = 737.2$  mm according to the explications in the former paragraph. Nevertheless, fig. 4.5a shows that in practice, the end pose of force control is located slightly higher due to the fact that the compression spring used in the experimental setup reacts differently to loading and unloading. The end position of force control is the same for both subtraction and strict threshold approach. However, fig. 4.5a shows that in the case of subtraction, the controller starts to approach the end position of force control earlier than when applying the strict threshold approach. We know that the input force/torque vector for the hybrid position/force controller using the subtraction approach is reduced by the

threshold, being set to 2 N along the  $z$ -direction, compared to the strict threshold approach. Note, that the force signal  $F_z$  in fig. 4.5b is the one when subtracting the threshold from the original force signal. As a result, in the strict threshold approach the controller interprets the end pose of force control to be further away from the actual pose and thus later begins to asymptotically approach it. Nevertheless, at the end pose for force control, the force/torque signal of the strict threshold approach immediately jumps from the threshold value to zero indicating the controller to switch to pure position control. This is also the explanation for the kink in the curve shown in fig. 4.5b. Based on these explanations, we can conclude that the step response applying the subtraction approach theoretically has to be equal to the one for the strict threshold approach when setting

$$\mathbf{F}_{\text{end}} = \begin{pmatrix} 0 \text{ N} \\ 0 \text{ N} \\ \text{threshold} \\ 0 \text{ Nm} \\ 0 \text{ Nm} \\ 0 \text{ Nm} \end{pmatrix} = \begin{pmatrix} 0 \text{ N} \\ 0 \text{ N} \\ 2 \text{ N} \\ 0 \text{ Nm} \\ 0 \text{ Nm} \\ 0 \text{ Nm} \end{pmatrix}. \quad (4.23)$$

Figure 4.5b confirms this conclusion. This observation also shows, that we can achieve better performance through increasing  $F_{z,\text{end}}$ . So, if we choose for example

$$\mathbf{F}_{\text{end}} = \begin{pmatrix} 0 \\ 0 \\ 10 \text{ N} \\ 0 \\ 0 \\ 0 \end{pmatrix}, \quad (4.24)$$

the step response applying hybrid position/force control with the subtraction approach fits the one resulting from independent joint control. We can expect the same result for applying the strict threshold approach for a threshold of 10 N while remaining  $F_{z,\text{end}} = 0 \text{ N}$ . However, such a strict threshold would be very inaccurate as this would lead to a large jump inside the measured force/torque signal  $\mathbf{F}$ .

So, can we always achieve good performance by just setting  $F_{z,\text{end}}$  to a large value? The experimental setup used in the context of this thesis allows us to specify  $\mathbf{F} \leq \mathbf{0} \text{ N (Nm)}$  as explained in section 3.2. As a result, the pose where  $F_{z,\text{end}} > 0 \text{ N}$  does not exist, but the specification makes the force controller believe that the TCP has to maintain its motion, even if it is close to the end pose of force control. As soon as the end pose of force control is actually reached, i.e.  $F_z = 0 \text{ N}$ , the change in the selection matrices leads to pure position control and makes further control independent of  $\mathbf{F}_{\text{end}}$ . However, imagine a situation where interaction forces continuously change from positive to negative values or vice versa, but for positive force values we want to control the position of the TCP and for negative force values its interaction forces or vice versa. In this case, we cannot easily avoid the undesired effect of slow control around the end pose of force control. So, in general we cannot arbitrarily set  $\mathbf{F}_{z,\text{end}}$  to any value that does not physically make sense.

Note, that hybrid position/force control only performs well in the former test case because we set  $z_{\text{end}}$  higher than the start position of force control. This is analog to choosing  $F_{z,\text{end}} > 0 \text{ N}$  during this test. However, for switching from a non-contact task to a contact task, such a specification of  $z_{\text{end}}$  is always physically possible and does not lead to any problems. To sum up, the main difficulty in hybrid position/force control is to handle slow control around the end pose of force control when switching from a contact task to a non-contact task due to asymptotically approaching the end pose of force control.



### 4.3 Testing on Position-based Impedance Control

Within position-based impedance control, the Stewart platform is modeled as an admittance because it accepts contact forces as input and yields motion of the TCP as output. Its target admittance behavior can be specified by the transfer function matrix  $\mathbf{G}_{\Delta\mathbf{x},\mathbf{F}}$  introduced in section 3.4 and defined by the diagonal mass/inertia, damping and stiffness matrices  $\mathbf{M}$ ,  $\mathbf{D}$  and  $\mathbf{K}$ . The values on their diagonal are named  $M_i$ ,  $D_i$  and  $K_i$  for the Stewart platform's DOFs  $i \in \{x, y, z, \alpha, \beta, \gamma\}$ . Analog to hybrid position/force control, we treat all DOFs equally and thus define:

$$M_i = M, D_i = D \text{ and } K_i = K \quad \forall i \in \{x, y, z, \alpha, \beta, \gamma\}. \quad (4.25)$$

Before being able to use the position-based impedance control for real control tasks, we need to tune its parameters. As the control method includes independent joint control, its control parameters are not only composed of the diagonals of the mass/inertia, damping and stiffness matrices  $M$ ,  $D$  and  $K$ , but also of the parameters of independent joint control  $K_{p,p}$ ,  $K_{p,v}$  and  $K_{I,v}$ . Firstly, in section 4.3.1, we study the influence of  $M$ ,  $D$  and  $K$  on the step response of the Stewart platform for unchanged independent joint control parameters. Secondly, in section 4.3.2, we also adapt  $K_{p,p}$ ,  $K_{p,v}$  and  $K_{I,v}$  to check whether this leads to better performance of the position-based impedance control. Again, we apply the step response analysis described in section 3.5. For all following tests, we set the force/torque offset at pose

$$\mathbf{x} = \left( 0 \text{ mm} \quad 0 \text{ mm} \quad 737 \text{ mm} \quad 0 \text{ rad} \quad 0 \text{ rad} \quad 0 \text{ rad} \right)^T \quad (4.26)$$

and specify the start and end pose vector and the initial guess for Newton's method as:

$$\mathbf{x}_{\text{start}} = \begin{pmatrix} 0 \text{ mm} \\ 0 \text{ mm} \\ 738 \text{ mm} \\ 0 \text{ rad} \\ 0 \text{ rad} \\ 0 \text{ rad} \end{pmatrix}, \quad \mathbf{x}_{\text{end}} = \begin{pmatrix} 0 \text{ mm} \\ 0 \text{ mm} \\ 741 \text{ mm} \\ 0 \text{ rad} \\ 0 \text{ rad} \\ 0 \text{ rad} \end{pmatrix}, \quad \mathbf{x}_0 = \begin{pmatrix} 0 \text{ mm} \\ 0 \text{ mm} \\ 734 \text{ mm} \\ 0 \text{ rad} \\ 0 \text{ rad} \\ 0 \text{ rad} \end{pmatrix}. \quad (4.27)$$

We measure the Stewart platform's actual leg lengths, compute the actual pose of the TCP with the help of forward kinematics and present the resulting step responses along the position of the TCP in  $z$ -direction in multiple plots which also include the target position  $z_d$  and the step response when applying independent joint control alone for comparison.

#### 4.3.1 Design of Position-based Impedance Controller Parameters

Position-based impedance control is equal to independent joint control as long as the TCP is not in contact with its environment, i.e. actual interaction force/torque values are equal to zero apart from noise in the measurements. Thus, control in free space only depends on the performance of the independent joint control. So, in order not to change the behavior of the Stewart platform in non-contact tasks, we use the standard parameter values for  $K_{p,p}$ ,  $K_{p,v}$  and  $K_{I,v}$  given in table 4.1. Instead, we concentrate on the target admittance behavior specified by the mass/inertia, damping and stiffness matrices and vary their parameters  $M$ ,  $D$  and  $K$  in order to experimentally study their effect on the dynamical behavior of the Stewart platform in contact tasks.

You will find the figures showing the results collected at the end of all explanations.

### Varying Damping and Stiffness Matrix for $M = 1 \text{ kg (kg} \cdot \text{m}^2)$

At first, we choose  $M = 1 \text{ kg (kg} \cdot \text{m}^2)$  and vary  $K$  from  $10000 \frac{\text{N}}{\text{m}}$  (Nm) to  $1 \frac{\text{N}}{\text{m}}$  (Nm) as well as  $D$  from  $1 \frac{\text{N}\cdot\text{s}}{\text{m}}$  (Nm·s) to  $1 \frac{\text{N}\cdot\text{s}}{\text{m}}$  (Nm·s). Figure 4.6 shows the results. Note, that the specification of the units using brackets indicates that units are different for position and orientation values.

At first, we observe that the deviation of the stationary position  $z$  from the target value  $z_d$  increases for decreasing values  $K$ . This confirms the explanations in section 3.4 and illustrates the relationship in eq. (3.14). Theoretically, we have to set  $K \rightarrow \infty$  in order to achieve stationary accuracy, i.e. to reach  $z_d$  for  $t \rightarrow \infty$ . However, in practice, the TCP reaches  $z_d$  for  $K = 10000 \frac{\text{N}}{\text{m}}$  (Nm) and approximately  $z = 740.97 \text{ mm}$  for  $K = 1000 \frac{\text{N}}{\text{m}}$  (Nm). For smaller values the deviation becomes visible in the plots and for  $K = 1 \frac{\text{N}}{\text{m}}$  (Nm) the stationary value  $z$  is even below the start position  $z_{\text{start}}$ . Thus, for real tasks it is reasonable to choose  $K \geq 1000 \frac{\text{N}}{\text{m}}$  (Nm).

Next, the analysis of the step responses shows that the system tends to oscillate for small damping constants  $D$ . On the other hand, large damping values lead to a large settling time as they strongly damp the motion of the TCP. This can be best seen in fig. 4.6d. This behavior corresponds to the one of a mass-spring-damper system and thus again supports the physical interpretation of position-based impedance control shown in fig. 3.8.

Another effect to be mentioned is that for large values  $K$  the static behavior of the system, i.e. the behavior observed for  $t \rightarrow \infty$ , dominates its dynamic (transient) behavior. Thus, the influence of  $D$  on the step response increases for decreasing values of the parameter  $K$ .

To sum up, the choice of the damping constant  $D$  is a trade-off between rapidity and avoidance of oscillations. On the other hand, the mass/inertia parameter  $K$  has to be tuned in a way that stationary accuracy is achieved. A good combination for  $M = 1 \text{ kg (kg} \cdot \text{m}^2)$  may be for example  $K = 10000 \frac{\text{N}}{\text{m}}$  (Nm) and  $D = 100 \frac{\text{N}\cdot\text{s}}{\text{m}}$  (Nm·s). In the following, we study the influence of the mass/inertia parameter  $M$  on the dynamics of the Stewart platform. In order to not restrict further investigations too much, we therefore again vary  $K$  from  $10000 \frac{\text{N}}{\text{m}}$  (Nm) to  $1 \frac{\text{N}}{\text{m}}$  (Nm) for  $D = 100 \frac{\text{N}\cdot\text{s}}{\text{m}}$ . Also, we look at  $D = 10 \frac{\text{N}\cdot\text{s}}{\text{m}}$  and  $D = 1000 \frac{\text{N}\cdot\text{s}}{\text{m}}$ , but limit these analyses to a variation of  $K$  from  $10000 \frac{\text{N}}{\text{m}}$  (Nm) to  $100 \frac{\text{N}}{\text{m}}$  (Nm).

### Varying Mass/Inertia and Stiffness Matrix for $D = 10 \frac{\text{N}\cdot\text{s}}{\text{m}}$ (Nm·s)

For the following test, we choose  $D = 10 \frac{\text{N}\cdot\text{s}}{\text{m}}$  (Nm·s) and vary  $K$  from  $10000 \frac{\text{N}}{\text{m}}$  (Nm) to  $100 \frac{\text{N}}{\text{m}}$  (Nm) as well as  $M$  from  $0.01 \text{ kg (kg} \cdot \text{m}^2)$  to  $100 \text{ kg (kg} \cdot \text{m}^2)$ . Figure 4.7 displays the results.

At first, we see that the relationship between stationary accuracy and the parameter  $K$  is the same as described in the former test. Additionally, in analogy to the explanation for the damping constant  $D$  above, the influence of  $M$  on the step response increases for decreasing values of the parameter  $K$ .

Besides, we observe decaying oscillations for large mass/inertia constants. Their amplitude as well as their settling time increase whereas their frequency decreases for increasing values of  $M$ . Again, this can be explained by the characteristics of a mass-spring-damper system. Small masses can be accelerated and decelerated by a small force, they are less inert. In order to accelerate and decelerate large masses, large forces are needed. Large masses are more inert. Thus, for large values  $M$ , the system is too inert and thus moves too far. Then, it moves back, but again too far because of its inert behavior. Oscillations occur. Note, that the effect is intensified for even higher masses  $M = 1000 \text{ kg (kg} \cdot \text{m}^2)$  and  $M = 10000 \text{ kg (kg} \cdot \text{m}^2)$  and therefore not displayed in the graphs. The curves for  $M = 0.01 \text{ kg (kg} \cdot \text{m}^2)$ ,  $M = 0.1 \text{ kg (kg} \cdot \text{m}^2)$  and  $M = 1 \text{ kg (kg} \cdot \text{m}^2)$  are nearly the same in the three graphs.

To sum up, for  $D = 10 \frac{\text{N}\cdot\text{s}}{\text{m}}$  (Nm · s) it seems like small values  $M = 0.01 \text{ kg}$  ( $\text{kg} \cdot \text{m}^2$ ),  $M = 0.1 \text{ kg}$  ( $\text{kg} \cdot \text{m}^2$ ) or  $M = 1 \text{ kg}$  ( $\text{kg} \cdot \text{m}^2$ ) and large values  $K = 10000 \frac{\text{N}}{\text{m}}$  (Nm) or  $1000 \frac{\text{N}}{\text{m}}$  (Nm) work best.

#### Varying Mass/Inertia and Stiffness Matrix for $D = 100 \frac{\text{N}\cdot\text{s}}{\text{m}}$ (Nm · s)

Now, we set  $D = 100 \frac{\text{N}\cdot\text{s}}{\text{m}}$  (Nm · s) and vary  $K$  from  $10000 \frac{\text{N}}{\text{m}}$  (Nm) to  $1 \frac{\text{N}}{\text{m}}$  (Nm) as well as  $M$  from  $0.1 \text{ kg}$  ( $\text{kg} \cdot \text{m}^2$ ) to  $1000 \text{ kg}$  ( $\text{kg} \cdot \text{m}^2$ ). Figure 4.8 displays the results.

Once again, the relationship between stationary accuracy and the parameter  $K$  as well as increasing influence of  $M$  on the step response for decreasing values of the parameter  $K$  can be observed. Additionally, everything that has been said about the decaying oscillations for large mass/inertia constants in the paragraph above holds true for this test. However, overall, the frequency as well as the settling time of the oscillations is smaller than for  $D = 10 \frac{\text{N}\cdot\text{s}}{\text{m}}$  (Nm · s). Descriptively speaking, the oscillations are damped more strongly by a higher damping constant.

Note, that the graphs do not include curves for  $M = 0.01 \text{ kg}$  ( $\text{kg} \cdot \text{m}^2$ ) as this leads to  $\Delta z = \text{NaN}$  for all values of  $K$ . The large difference in order of magnitude between  $M = 0.01 \text{ kg}$  ( $\text{kg} \cdot \text{m}^2$ ) and  $D = 100 \frac{\text{N}\cdot\text{s}}{\text{m}}$  seems to lead to computational inaccuracies and thus to values equal to zero in the denominators of the admittance transfer functions. The curves for  $M = 0.1 \text{ kg}$  ( $\text{kg} \cdot \text{m}^2$ ),  $M = 1 \text{ kg}$  ( $\text{kg} \cdot \text{m}^2$ ) and  $M = 10 \text{ kg}$  ( $\text{kg} \cdot \text{m}^2$ ) are nearly the same in all graphs.

To sum up, for  $D = 100 \frac{\text{N}\cdot\text{s}}{\text{m}}$  (Nm · s), rather small values  $M = 0.1 \text{ kg}$  ( $\text{kg} \cdot \text{m}^2$ ),  $M = 1 \text{ kg}$  ( $\text{kg} \cdot \text{m}^2$ ) or  $M = 10 \text{ kg}$  ( $\text{kg} \cdot \text{m}^2$ ) and large values  $K = 10000 \frac{\text{N}}{\text{m}}$  (Nm) or  $K = 1000 \frac{\text{N}}{\text{m}}$  (Nm) work best.

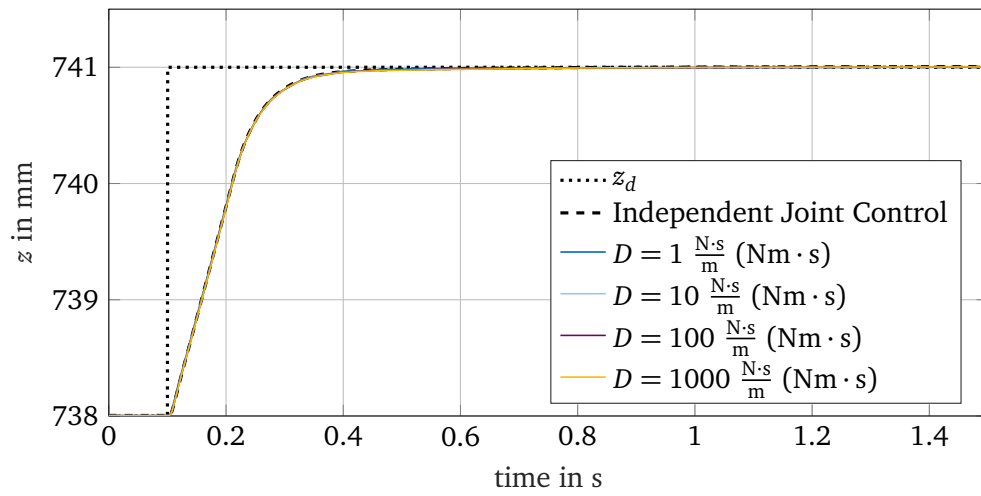
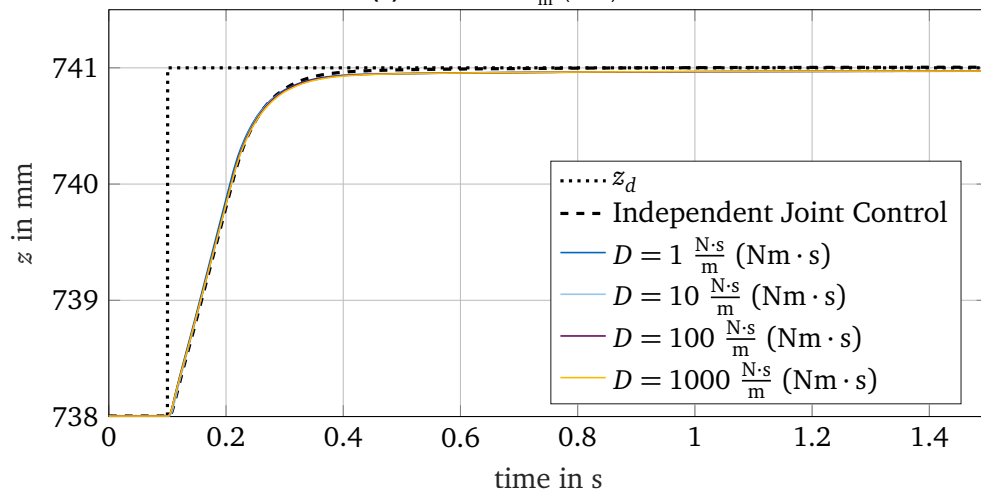
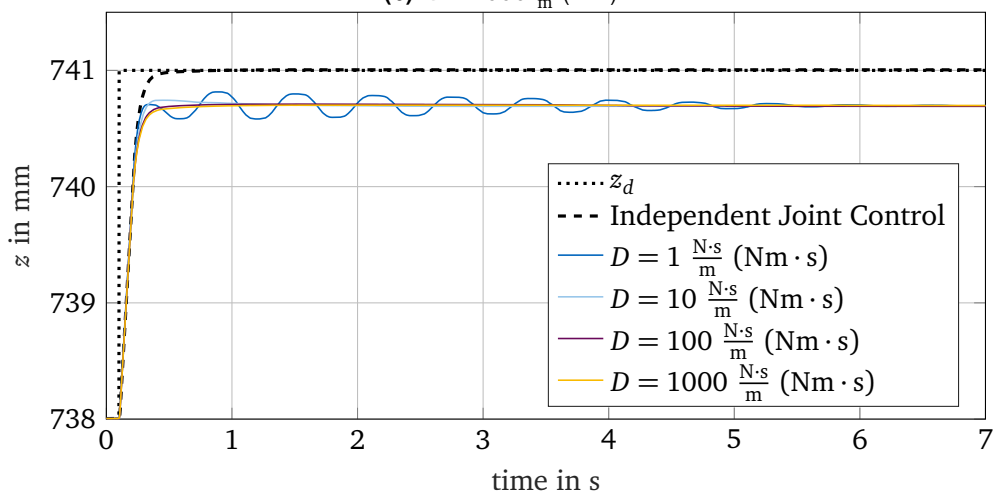
#### Varying Mass/Inertia and Stiffness Matrix for $D = 1000 \frac{\text{N}\cdot\text{s}}{\text{m}}$ (Nm · s)

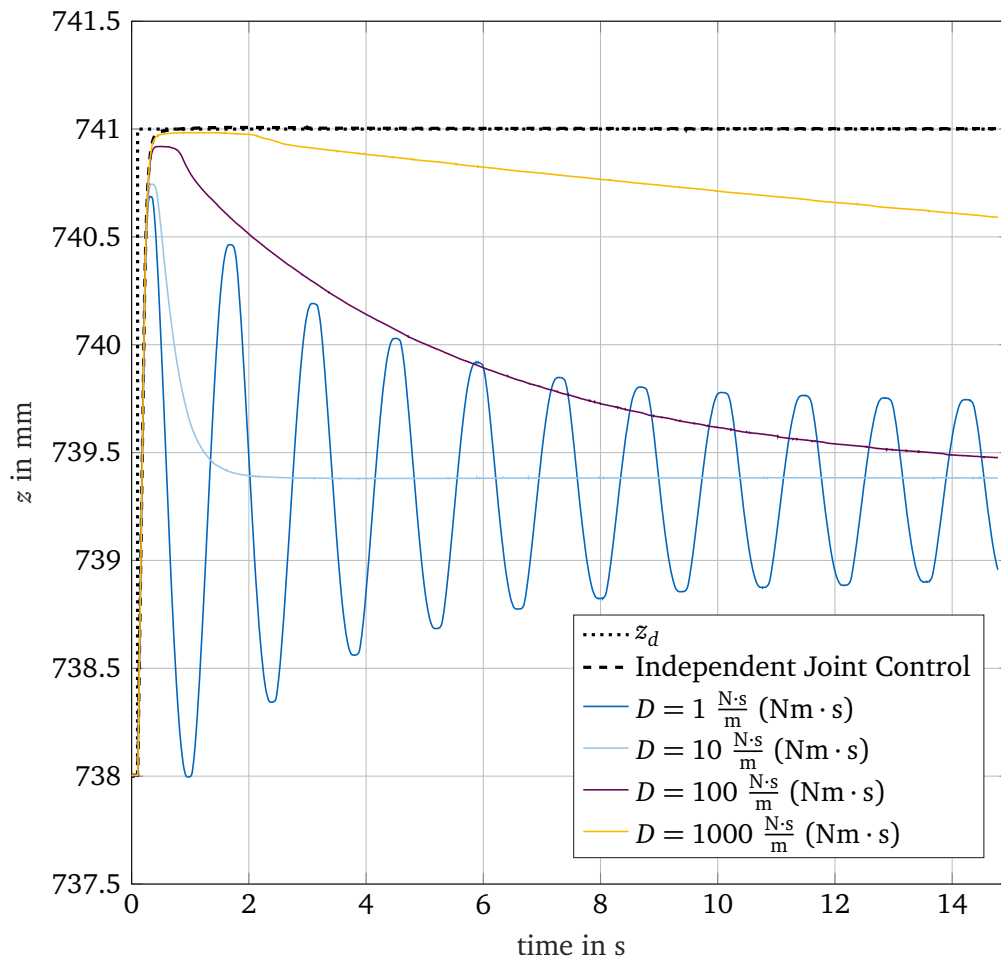
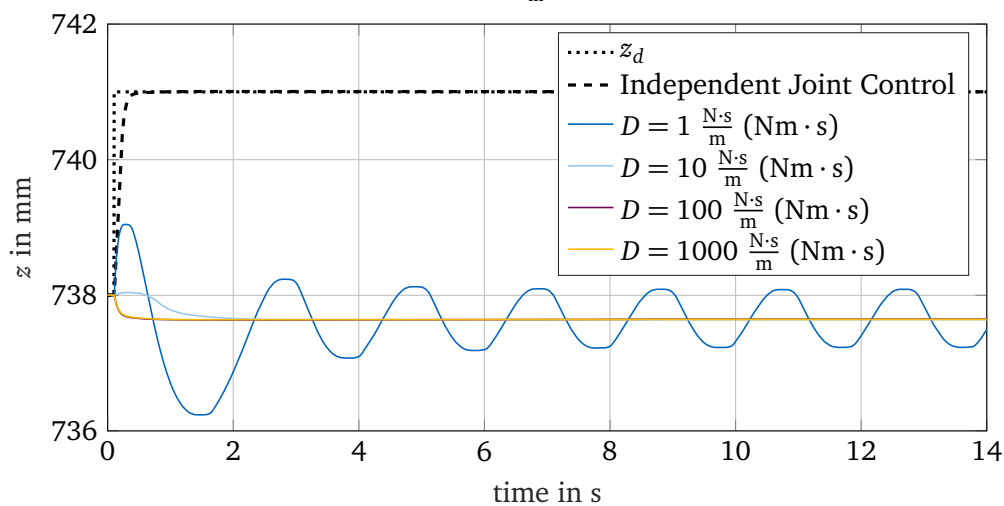
Finally, we try  $D = 1000 \frac{\text{N}\cdot\text{s}}{\text{m}}$  (Nm · s) and vary  $K$  from  $10000 \frac{\text{N}}{\text{m}}$  (Nm) to  $100 \frac{\text{N}}{\text{m}}$  (Nm) as well as  $M$  from  $1 \text{ kg}$  ( $\text{kg} \cdot \text{m}^2$ ) to  $10000 \text{ kg}$  ( $\text{kg} \cdot \text{m}^2$ ). Figure 4.9 shows the results. All the relations that have already been discussed hold true. Besides, the effect of the oscillations gets stronger. Again, the problem concerning  $\Delta z = \text{NaN}$  appears, but this time also for  $M = 0.1 \text{ kg}$  ( $\text{kg} \cdot \text{m}^2$ ). So, this time, the difference in order of magnitude between  $M = 0.01 \text{ kg}$  ( $\text{kg} \cdot \text{m}^2$ ) and  $M = 0.1 \text{ kg}$  ( $\text{kg} \cdot \text{m}^2$ ) and  $D = 1000 \frac{\text{N}\cdot\text{s}}{\text{m}}$  (Nm · s) leads to computational inaccuracies. The curves for  $M = 1 \text{ kg}$  ( $\text{kg} \cdot \text{m}^2$ ),  $M = 10 \text{ kg}$  ( $\text{kg} \cdot \text{m}^2$ ) and  $M = 100 \text{ kg}$  ( $\text{kg} \cdot \text{m}^2$ ) are nearly the same in all graphs.

To sum up, for  $D = 1000 \frac{\text{N}\cdot\text{s}}{\text{m}}$  (Nm · s), values  $M = 1 \text{ kg}$  ( $\text{kg} \cdot \text{m}^2$ ),  $M = 10 \text{ kg}$  ( $\text{kg} \cdot \text{m}^2$ ) or  $M = 100 \text{ kg}$  ( $\text{kg} \cdot \text{m}^2$ ) and large values  $K = 10000 \frac{\text{N}}{\text{m}}$  (Nm) or  $K = 1000 \frac{\text{N}}{\text{m}}$  (Nm) work best.

Comparing the former three tests, we can observe that the influence of the mass/inertia parameter  $M$  on the system behavior decreases for increasing damping constants  $D$ . On the one hand,  $M$  has to be chosen larger for larger values  $D$  in order to achieve comparable curves with regard to the graphs of smaller constants  $D$ . On the other hand, the system tends to less oscillation for larger values  $D$ . Again, this is plausible when thinking of a mass-spring-damper system.

Regarding all investigations with focus on the mass/inertia, damping and stiffness constants, we can declare the following relationships: Increasing  $K$  leads to better stationary accuracy but less influence on the step response by  $M$  and  $D$ . Increasing  $M$  and decreasing  $D$  results in more oscillations. Furthermore, decreasing  $D$  allows more influence on the system behavior by  $M$ . Having in mind all effects, we choose  $M = 1 \text{ kg}$  ( $\text{kg} \cdot \text{m}^2$ ),  $D = 100 \frac{\text{N}\cdot\text{s}}{\text{m}}$  (Nm · s) and  $K = 10000 \frac{\text{N}}{\text{m}}$  (Nm) in order to achieve stationary accurate, fast behavior without any oscillations.

(a)  $K = 10000 \frac{N}{m}$  (Nm)(b)  $K = 1000 \frac{N}{m}$  (Nm)(c)  $K = 100 \frac{N}{m}$  (Nm)

(d)  $K = 10 \frac{\text{N}}{\text{m}}$  (Nm)(e)  $K = 1 \frac{\text{N}}{\text{m}}$  (Nm)

**Figure 4.6:** Comparison of step responses for different values  $K$  when applying position-based impedance control for  $M = 1 \text{ kg}$  ( $\text{kg} \cdot \text{m}^2$ ) and varying  $D$  from  $1 \frac{\text{N}\cdot\text{s}}{\text{m}}$  ( $\text{Nm} \cdot \text{s}$ ) to  $1000 \frac{\text{N}\cdot\text{s}}{\text{m}}$  ( $\text{Nm} \cdot \text{s}$ )

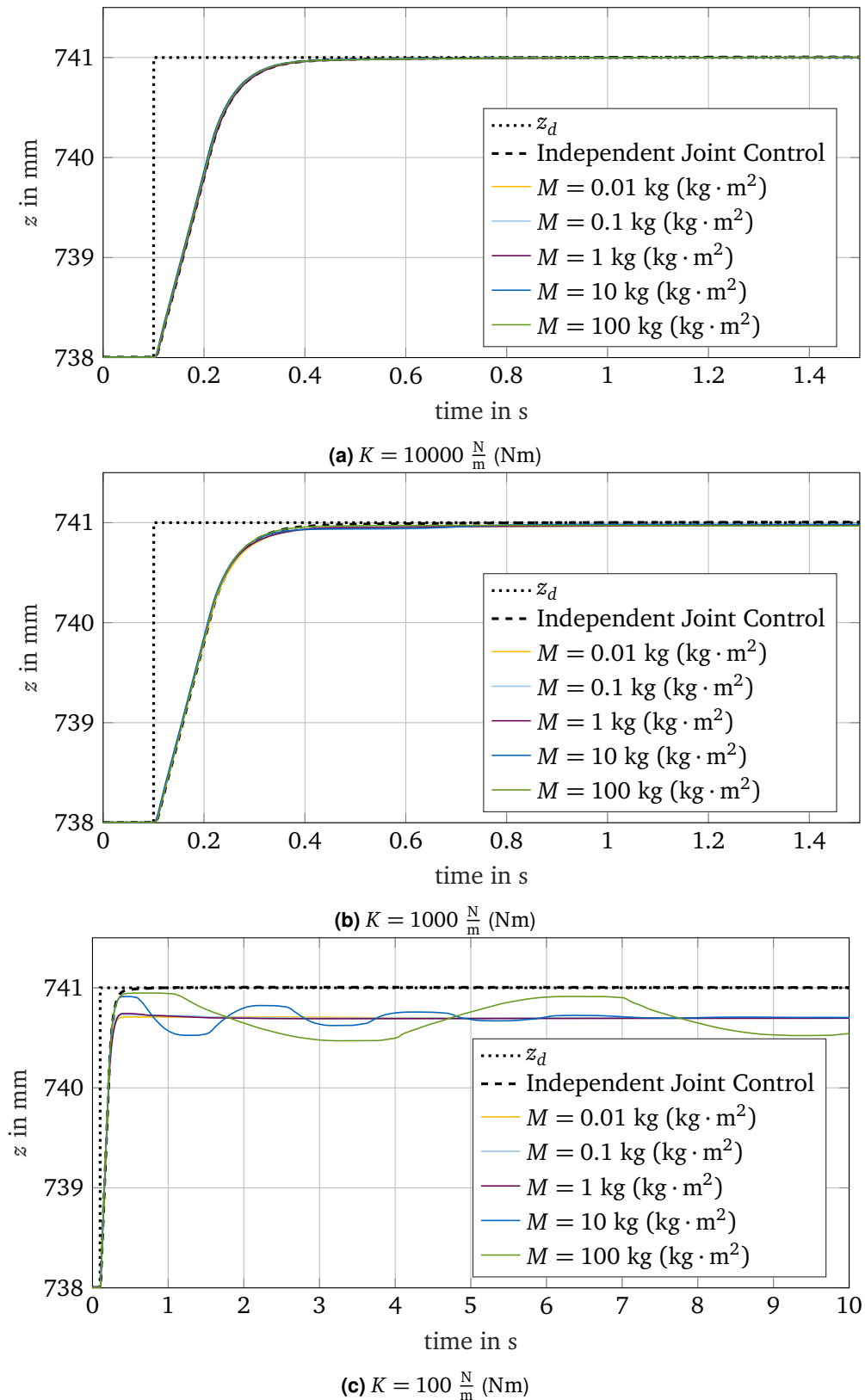
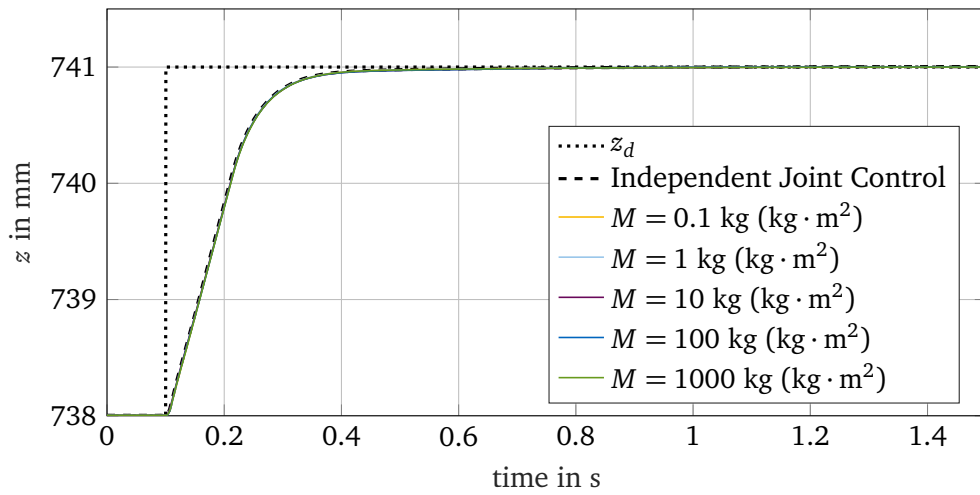
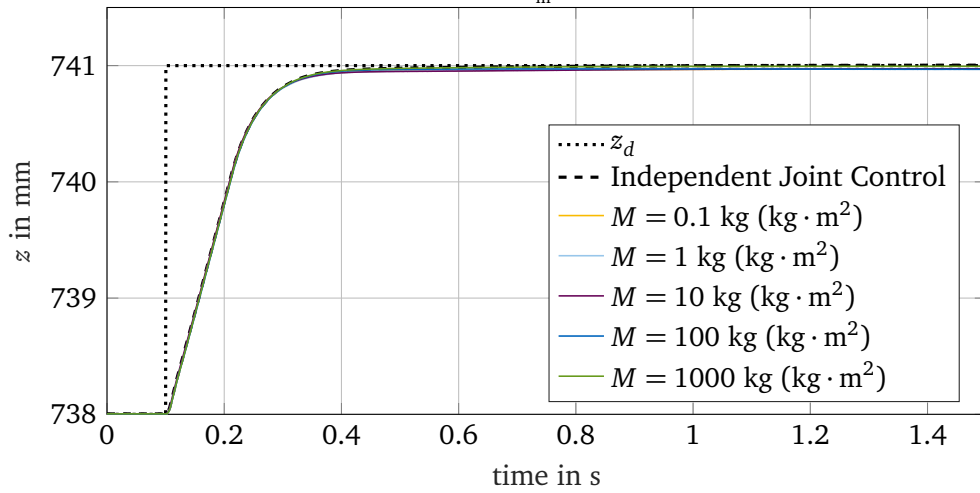


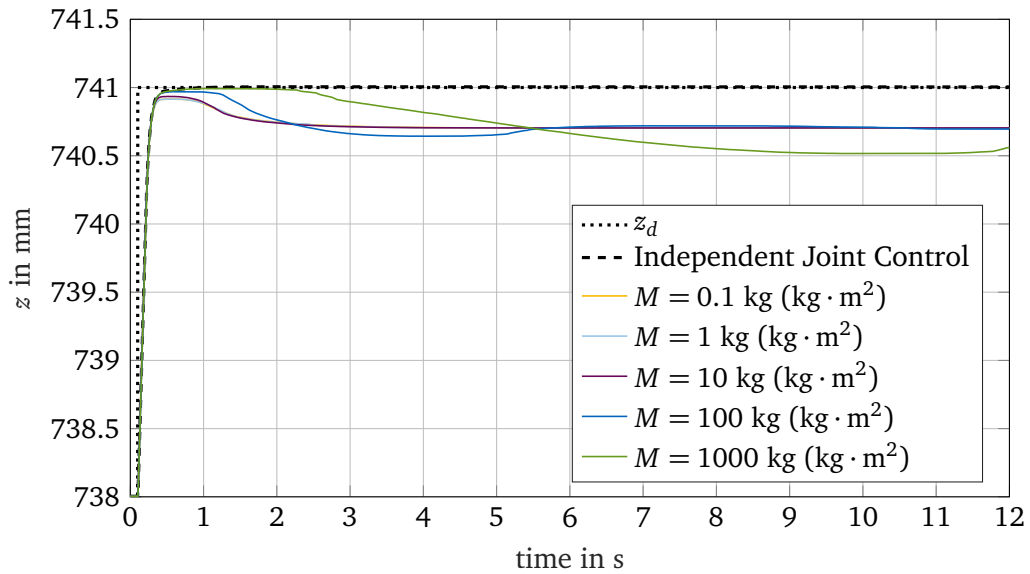
**Figure 4.7:** Comparison of step responses for different values  $K$  when applying position-based impedance control for  $D = 10 \frac{\text{N}\cdot\text{s}}{\text{m}}$  (Nm · s) and varying  $M$  from 0.01 kg ( $\text{kg} \cdot \text{m}^2$ ) to 100 kg ( $\text{kg} \cdot \text{m}^2$ )



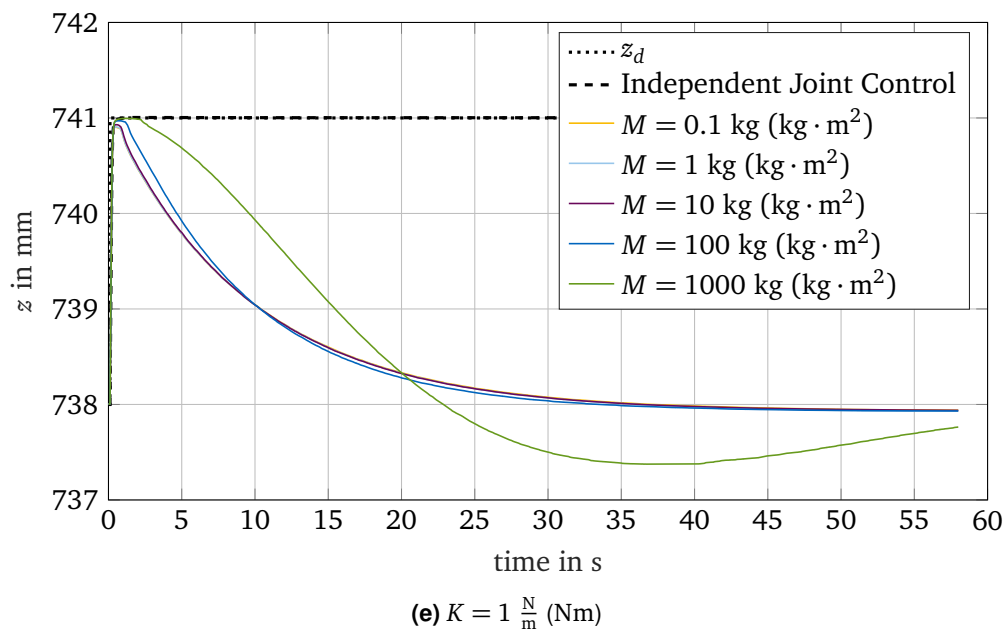
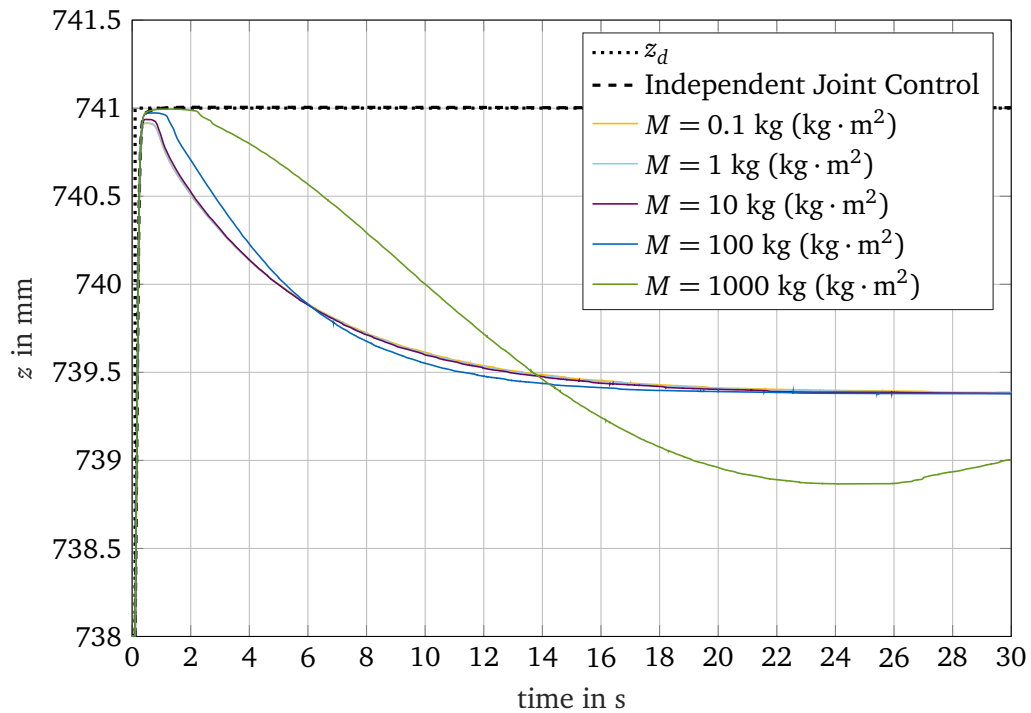
(a)  $K = 10000 \frac{N}{m}$  (Nm)



(b)  $K = 1000 \frac{N}{m}$  (Nm)

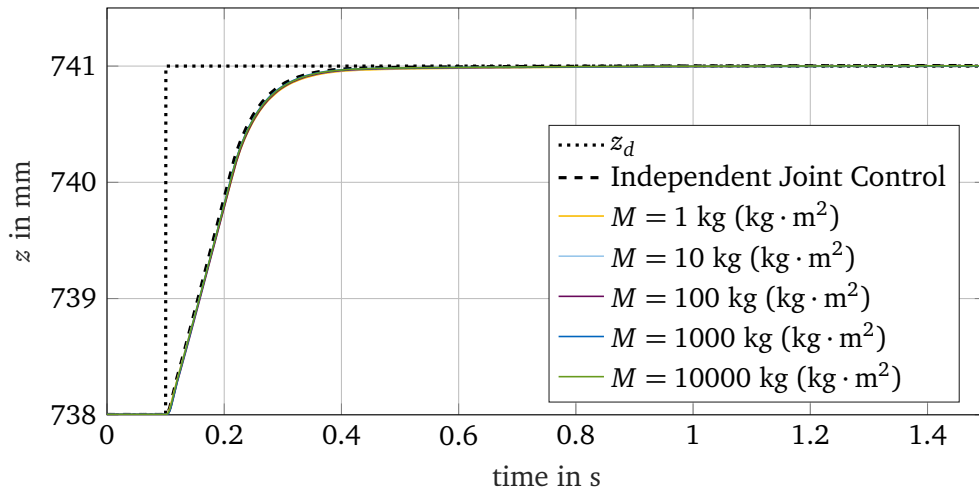
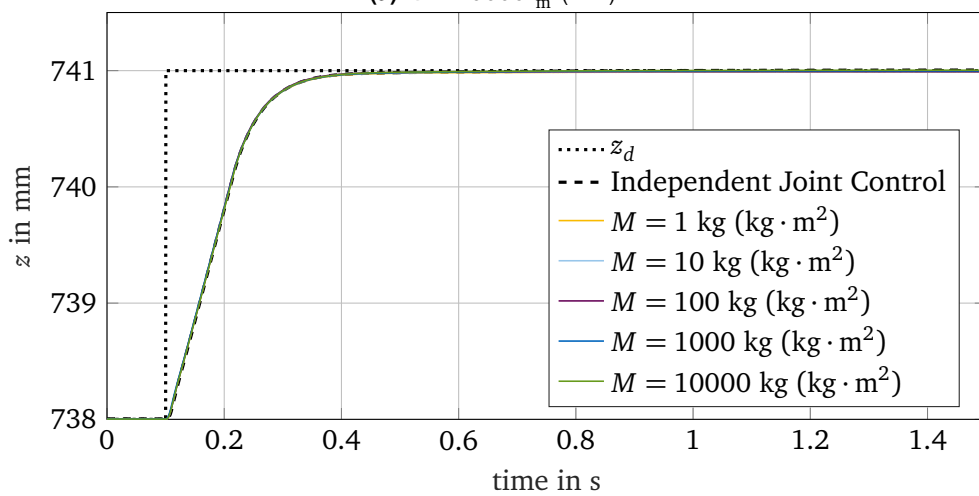
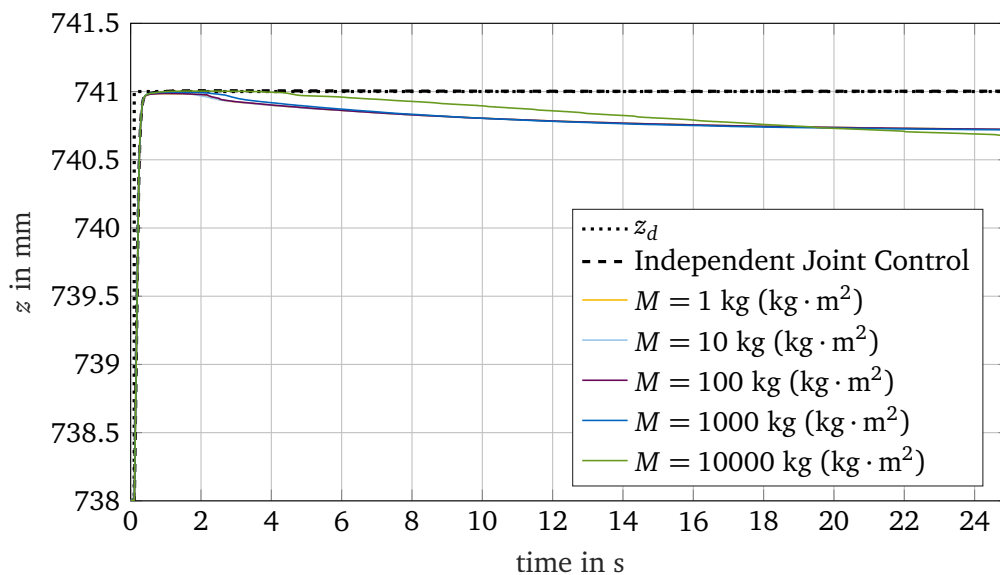


(c)  $K = 100 \frac{N}{m}$  (Nm)



**Figure 4.8:** Comparison of step responses for different values  $K$  when applying position-based impedance control for  $D = 100 \frac{\text{N}\cdot\text{s}}{\text{m}}$  and varying  $M$  from  $0.1 \text{ kg (kg}\cdot\text{m}^2)$  to  $1000 \text{ kg (kg}\cdot\text{m}^2)$



(a)  $K = 10000 \frac{\text{N}}{\text{m}}$  (Nm)(b)  $K = 1000 \frac{\text{N}}{\text{m}}$  (Nm)(c)  $K = 100 \frac{\text{N}}{\text{m}}$  (Nm)

**Figure 4.9:** Comparison of step responses for different values  $K$  when applying position-based impedance control for  $D = 1000 \frac{\text{N}\cdot\text{s}}{\text{m}}$  (Nm · s) and varying  $M$  from 1 kg ( $\text{kg}\cdot\text{m}^2$ ) to 10000 kg ( $\text{kg}\cdot\text{m}^2$ )

### Varying Pole Placement in the Target Admittance Behavior

In this paragraph, we want to analyze the control parameters of hybrid position/force control from another perspective. As we know, the target admittance of the manipulator, described by the transfer functions in eq. (3.12), is modeled as a PT2-system, a mass-spring-damper system in particular. Typically we distinguish three major cases for a stable PT2-system: the underdamped, critically damped and overdamped one. They are each characterized by a specific pole placement in the left complex plane. We choose the poles  $s_1$  and  $s_2$  in a way that the corresponding parameters  $M$ ,  $D$  and  $K$  have a similar order of magnitude for each case. By this, we make sure that the influence of these parameters on the step response discussed in the previous paragraphs, does not predominate the effects that may result from different pole placements. Furthermore, we set  $K = 100 \frac{\text{N}}{\text{m}}$  (Nm) because we have learned from the investigations above, that  $K$  has to be rather large in order to achieve stationary accuracy, but not too large for analysis purposes, in order to be able to still see the transient behavior of the system. Having this in mind, we arbitrarily specify:

- critically damped case:  $s_1 = s_2 = -10$ , leading to  $M = 1 \text{ kg (kg} \cdot \text{m}^2)$ ,  $D = 10 \frac{\text{N} \cdot \text{s}}{\text{m}}$  (Nm · s),  $K = 100 \frac{\text{N}}{\text{m}}$  (Nm);
- overdamped case:  $s_1 = -4$ ,  $s_2 = -25$ , leading to  $M = 1 \text{ kg (kg} \cdot \text{m}^2)$ ,  $D = 29 \frac{\text{N} \cdot \text{s}}{\text{m}}$  (Nm · s),  $K = 100 \frac{\text{N}}{\text{m}}$  (Nm);
- critically damped case:  $s_1 = -\frac{11}{2} - \frac{3}{2}\sqrt{31}i$ ,  $s_2 = -\frac{11}{2} + \frac{3}{2}\sqrt{31}i$ , leading to  $M = 1 \text{ kg (kg} \cdot \text{m}^2)$ ,  $D = 11 \frac{\text{N} \cdot \text{s}}{\text{m}}$  (Nm · s),  $K = 100 \frac{\text{N}}{\text{m}}$  (Nm).

The corresponding step responses are displayed in fig. 4.10. The curves are nearly identical. Thus, the choice of pole placement does not influence the system behavior, except that it generates different parameters  $M$ ,  $D$  and  $K$  and thus leads to the effects we have already examined in the previous tests.

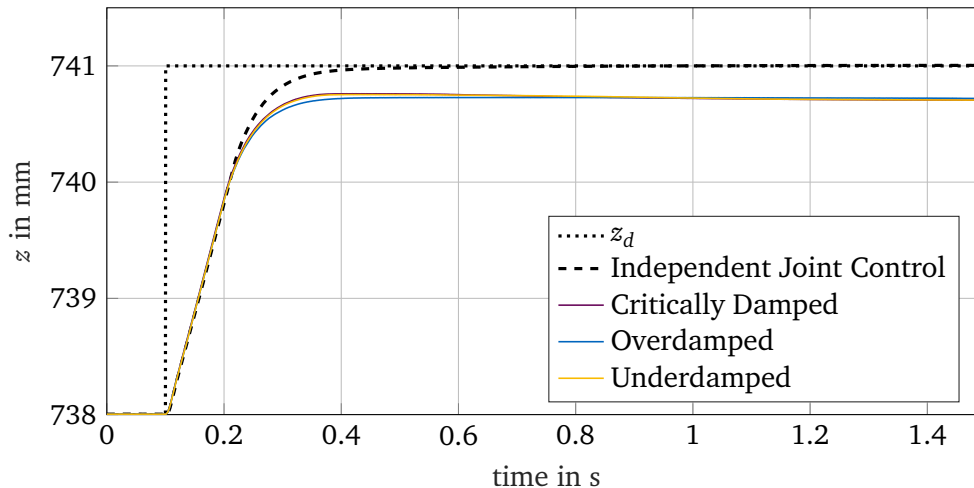


Figure 4.10: Variation of pole placement in the target admittance behavior

### Overview of Control Parameters of Position-based Impedance Control

Former tests lead to following appropriate control parameters for position-based impedance control, listed in Table 4.3.

**Table 4.3:** Control parameters of position-based impedance control

parameter	value
$K_{p,p}$	$20 \frac{1}{s}$
$K_{p,v}$	$0.2 \frac{Vs}{mm}$
$K_{I,v}$	$1 \frac{V}{mm}$
$M$	$1 \text{ kg (kg} \cdot \text{m}^2)$
$D$	$100 \frac{N \cdot s}{m} \text{ (Nm} \cdot \text{s)}$
$K$	$10000 \frac{N}{m} \text{ (Nm)}$

### 4.3.2 Approach for an Alternative Position-based Impedance Control

In contrast to section 4.3.1, we now extend our analysis and not only restrict tuning of the hybrid position/force control to the target admittance behavior specified by the mass/inertia, damping and stiffness matrices and vary their parameters  $M$ ,  $D$  and  $K$ , but also increase the position controller parameter  $K_{p,p}$  of independent joint control. By this, we hope being able to adjust the step response for contact-tasks in a way that the system reacts more quickly to changes in the target pose vector  $\mathbf{x}_d$ , but still gently reaches its stationary value without any overshooting. Indeed, this cannot be done without changing the system behavior in non-contact tasks. However, the action is reasonable if we assume that moving in free space may be performed with less accuracy. Imagine the following situation: the Stewart platform is used as a medical device. Then, the TCP has to be moved close to a human's body and gently get in contact with it. The motion towards the contact surface does not have to be performed very accurate. Nevertheless, as soon as the TCP reaches the human's skin, exactly controlled motion is required in order to not harm the human. So, we can consider the contact-task to be the critical one and accept a poorer performance during the non-contact task. In the following, we first analyze the effect of varying  $K_{p,p}$  in independent joint control. Thereafter, we set the parameter to an appropriate value and vary the target admittance parameters  $M$ ,  $D$  and  $K$  to see whether we can create an improved position-based impedance control.

#### Varying $K_{p,p}$ in Independent Joint Control

Firstly, we look at the effect of varying  $K_{p,p}$  in independent joint control. Therefore, we change the response analysis parameters in eq. (4.27) to

$$\mathbf{x}_{\text{start}} = \begin{pmatrix} 0 \text{ mm} \\ 0 \text{ mm} \\ 720 \text{ mm} \\ 0 \text{ rad} \\ 0 \text{ rad} \\ 0 \text{ rad} \end{pmatrix}, \quad \mathbf{x}_{\text{end}} = \begin{pmatrix} 0 \text{ mm} \\ 0 \text{ mm} \\ 723 \text{ mm} \\ 0 \text{ rad} \\ 0 \text{ rad} \\ 0 \text{ rad} \end{pmatrix}, \quad \mathbf{x}_0 = \begin{pmatrix} 0 \text{ mm} \\ 0 \text{ mm} \\ 716 \text{ mm} \\ 0 \text{ rad} \\ 0 \text{ rad} \\ 0 \text{ rad} \end{pmatrix} \quad (4.28)$$

in order to create a non-contact task. We want to choose the parameter value  $K_{p,p}$  from analyzing the motion of the TCP in free space in order to make sure that the performance of the later designed position-based impedance controller is still adequate in non-contact tasks. Figure 4.11 shows the resulting step responses. They are similar to those of hybrid position/force control in fig. 4.2. Increasing  $K_{p,p}$  leads to a faster dynamic behavior, i.e. settling time decreases. Also, the TCP tends to overshoot its target position  $z_d$  for large parameter values.

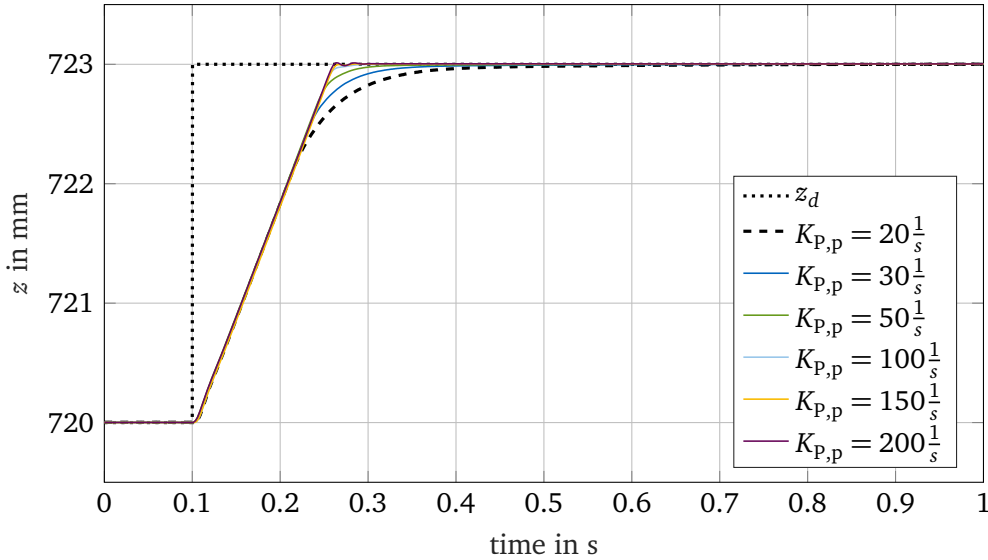


**Figure 4.11:** Variation of the parameter  $K_{p,p}$  in independent joint control

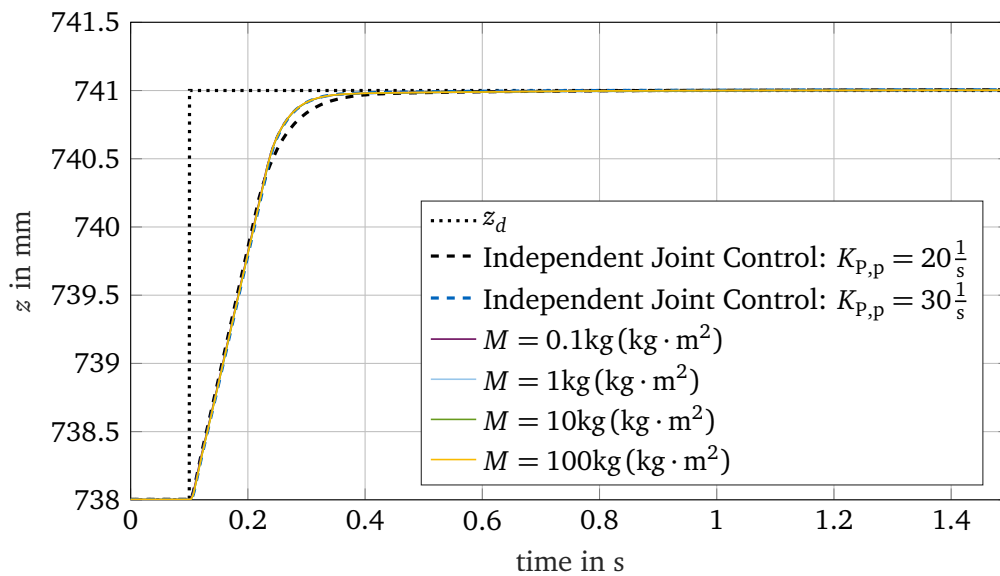
For the following analysis, we set  $K_{p,p} = 30 \frac{1}{s}$ . By this, settling time is reduced in contrast to the former value  $K_{p,p} = 20 \frac{1}{s}$ , but still it is unlikely that overshooting appears.

#### Testing on Position-based Impedance Control with Larger Value $K_{p,p}$

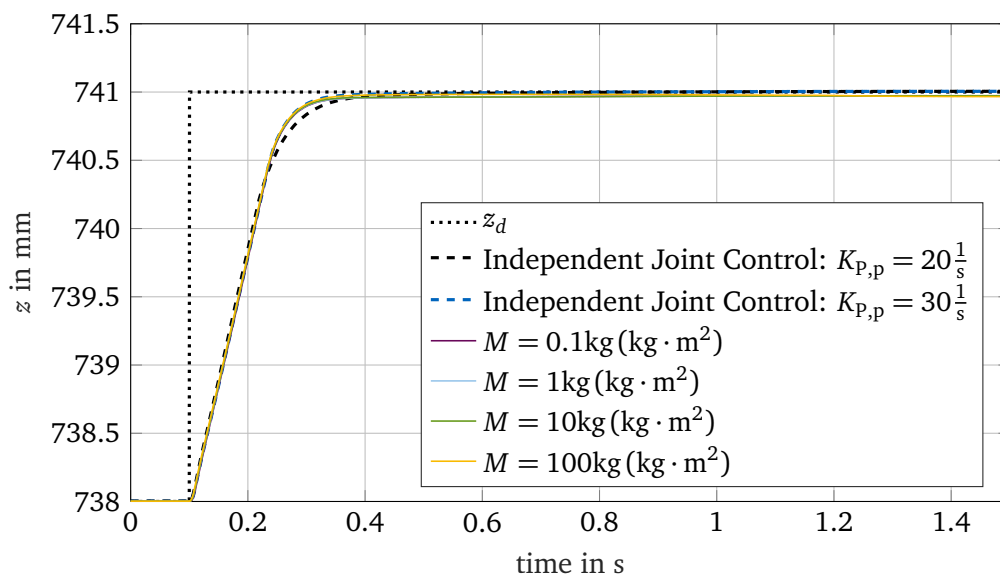
We now use the new parameter value  $K_{p,p} = 30 \frac{1}{s}$  in position-based impedance control. Once again, we perform a step response analysis using the parameters defined at the beginning of section 4.3. We examine the target admittance behavior by altering mass/inertia, damping and stiffness constants in the following way: varying  $M$  from 0.1 kg ( $\text{kg} \cdot \text{m}^2$ ) to 100 kg ( $\text{kg} \cdot \text{m}^2$ ), varying  $D$  from  $1 \frac{\text{N} \cdot \text{s}}{\text{m}}$  ( $\text{Nm} \cdot \text{s}$ ) to  $100 \frac{\text{N} \cdot \text{s}}{\text{m}}$  ( $\text{Nm} \cdot \text{s}$ ) and varying  $K$  from  $1000 \frac{\text{N}}{\text{m}}$  ( $\text{Nm}$ ) to  $10000 \frac{\text{N}}{\text{m}}$  ( $\text{Nm}$ ). We choose  $K$  rather large in order to guarantee stationary accuracy. Besides, we set  $D$  and  $M$  to rather small values because we want to avoid very inert system behavior as well as strong damping. Figure 4.12 exemplary shows the results for  $D = 100 \frac{\text{N} \cdot \text{s}}{\text{m}}$  ( $\text{Nm} \cdot \text{s}$ ),  $K = 10000 \frac{\text{N}}{\text{m}}$  ( $\text{Nm}$ ) and  $K = 1000 \frac{\text{N}}{\text{m}}$  ( $\text{Nm}$ ) and different values  $M$ .

Our goal for an alternative position-based impedance control is to create a system behavior with fast dynamics at the beginning and compliant characteristics close to the desired end pose. In practice, its step response would have to follow the one resulting from independent joint control with a higher control parameter, e.g.  $K_{p,p} = 30 \frac{1}{s}$  at the beginning and fit the step response of a lower independent joint control parameter e.g.  $K_{p,p} = 20 \frac{1}{s}$  when approaching its stationary value. However, the graphs show that this behavior cannot sufficiently be realized by position-based impedance control. For  $K = 10000 \frac{\text{N}}{\text{m}}$  ( $\text{Nm}$ ) all curves are equal to the one when applying independent joint control with  $K_{p,p} = 30 \frac{1}{s}$ . For  $K = 1000 \frac{\text{N}}{\text{m}}$  ( $\text{Nm}$ ), the TCP seems to move more gently towards the stationary pose as the step responses weakly deviate from the step response for independent joint control with  $K_{p,p} = 30 \frac{1}{s}$ . However, this happens at the cost of stationary accuracy, which is not perfectly achieved in this case. Nevertheless, the loss of accuracy is small and for use cases where high stationary accuracy is considered less important, choosing smaller values  $K$  in order to achieve a more gentle behavior close to the end pose may be an appropriate method. Still keep in mind that the effect of the target admittance parameters on the resulting step response is very little. Analog analyses for  $D = 1 \frac{\text{N} \cdot \text{s}}{\text{m}}$  ( $\text{Nm} \cdot \text{s}$ ) and  $D = 10 \frac{\text{N} \cdot \text{s}}{\text{m}}$  ( $\text{Nm} \cdot \text{s}$ ) lead to the same results. They also show that, overall, the effects of the approach for an alternative position-based impedance

control are very weak and only apparent for smaller values  $K$ . As a result, we stick to the parameters listed in table 4.3 when using position-based impedance control.



(a)  $K = 10000 \frac{\text{N}}{\text{m}}$  (Nm)



(b)  $K = 1000 \frac{\text{N}}{\text{m}}$  (Nm)

**Figure 4.12:** Comparison of step responses for different values  $K$  when applying the approach for an alternative position-based impedance control for  $D = 100 \frac{\text{N}\cdot\text{s}}{\text{m}}$  (Nm · s) and varying  $M$  from 0.1 kg (kg · m<sup>2</sup>) to 100 kg (kg · m<sup>2</sup>)

## 4.4 Comparative Test Cases and Validation

During the last two sections we have tuned the parameters of hybrid position/force control and position-based impedance control and separately studied the characteristics of both control schemes. In the following, we want to compare the two compliant motion control approaches in terms of their behavior during section 4.4.1 as well as in terms of computa-

tional costs in section 4.4.2. At the end, in section 4.4.3, we validate both control concepts by applying them along another DOF of the Stewart platform. For the following tests we use the control parameters determined in section 4.2 and section 4.3 and listed in table 4.2 and table 4.3.

#### 4.4.1 Testing on Behavioral Differences

In this section, we look at differences between hybrid position/force control and position-based impedance control in terms of their dynamical behavior. Therefore, we consider two different test cases. At first, we create a target position and force trajectory that consists of multiple Heaviside step functions. Thereafter, we compare both control schemes' performances following the test trajectory introduced in section 3.5.

##### Multiple Step Response Analysis

We begin with a simple step response analysis. We want to compare hybrid position/force control and position-based impedance control while switching from a non-contact task to a contact task and vice versa as well as during a pure contact task. Thus, we specify multiple target pose and force/torque vectors:

$$\begin{aligned}
 \mathbf{x}_{\text{start},1} &= \begin{pmatrix} 0 \text{ mm} \\ 0 \text{ mm} \\ 736 \text{ mm} \\ 0 \text{ rad} \\ 0 \text{ rad} \\ 0 \text{ rad} \end{pmatrix}, & \mathbf{x}_{\text{end},1} &= \begin{pmatrix} 0 \text{ mm} \\ 0 \text{ mm} \\ 743 \text{ mm} \\ 0 \text{ rad} \\ 0 \text{ rad} \\ 0 \text{ rad} \end{pmatrix} = \mathbf{x}_{\text{start},2}, \\
 \mathbf{x}_{\text{end},2} = \mathbf{x}_{\text{start},3} &= \begin{pmatrix} 0 \text{ mm} \\ 0 \text{ mm} \\ 744 \text{ mm} \\ 0 \text{ rad} \\ 0 \text{ rad} \\ 0 \text{ rad} \end{pmatrix}, & \mathbf{x}_{\text{end},3} &= \begin{pmatrix} 0 \text{ mm} \\ 0 \text{ mm} \\ 742 \text{ mm} \\ 0 \text{ rad} \\ 0 \text{ rad} \\ 0 \text{ rad} \end{pmatrix} = \mathbf{x}_{\text{start},4}, \\
 \mathbf{x}_{\text{end},4} &= \begin{pmatrix} 0 \text{ mm} \\ 0 \text{ mm} \\ 736 \text{ mm} \\ 0 \text{ rad} \\ 0 \text{ rad} \\ 0 \text{ rad} \end{pmatrix}.
 \end{aligned} \tag{4.29}$$

We present these target poses to the system one after another and hold each one for five seconds. The force/torque offset is set at pose

$$\mathbf{x} = ( 0 \text{ mm} \quad 0 \text{ mm} \quad 737 \text{ mm} \quad 0 \text{ rad} \quad 0 \text{ rad} \quad 0 \text{ rad} )^T. \tag{4.30}$$

As a result, the first step moves the TCP from a non-contact task to a contact task, the next two steps take place in a contact task and the last one defines a switch from a contact task to a non-contact task. In order to be able to compare the step responses with the target input pose, we once again use Newton's method to compute the actual pose of the TCP. Therefore,

we use the following arbitrary initial guess:

$$\mathbf{x}_0 = \begin{pmatrix} 0 \text{ mm} \\ 0 \text{ mm} \\ 734 \text{ mm} \\ 0 \text{ rad} \\ 0 \text{ rad} \\ 0 \text{ rad} \end{pmatrix}. \quad (4.31)$$

We want to again restrict the analysis to the  $z$ -direction of the Stewart platform. Thus, for hybrid position/force control we define the following compliance selection matrix:

$$\mathbf{S} = \text{diag}(001000) \quad (4.32)$$

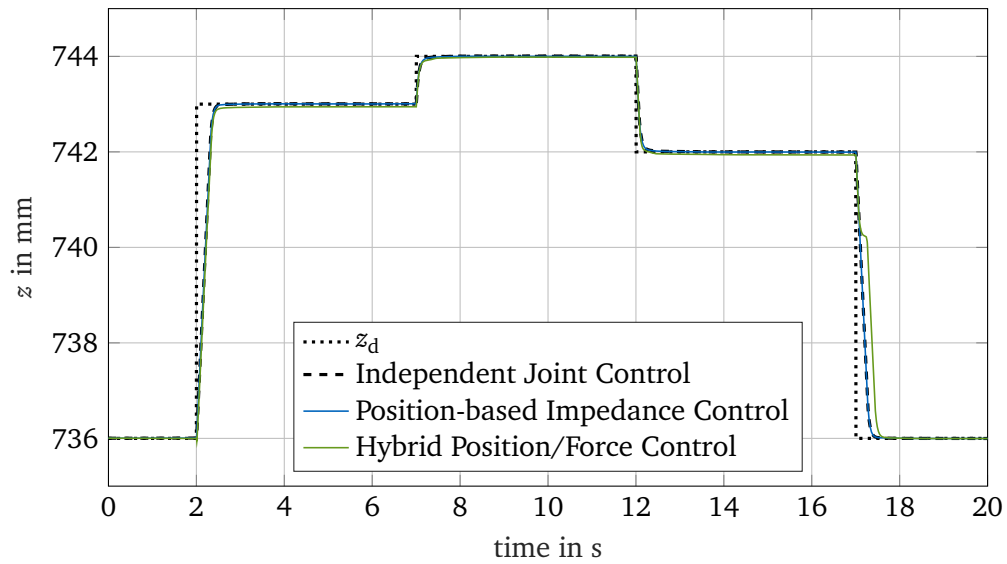
as well as following target force/torque values:

$$\begin{aligned} \mathbf{F}_{\text{start},1} &= \begin{pmatrix} 0 \text{ N} \\ 0 \text{ N} \\ 0 \text{ N} \\ 0 \text{ Nm} \\ 0 \text{ Nm} \\ 0 \text{ Nm} \end{pmatrix}, & \mathbf{F}_{\text{end},1} &= \begin{pmatrix} 0 \text{ N} \\ 0 \text{ N} \\ -27.56 \text{ N} \\ 0 \text{ Nm} \\ 0 \text{ Nm} \\ 0 \text{ Nm} \end{pmatrix} = \mathbf{F}_{\text{start},2}, \\ \mathbf{F}_{\text{end},2} &= \begin{pmatrix} 0 \text{ N} \\ 0 \text{ N} \\ -36.88 \text{ N} \\ 0 \text{ Nm} \\ 0 \text{ Nm} \\ 0 \text{ Nm} \end{pmatrix} = \mathbf{F}_{\text{start},3}, & \mathbf{F}_{\text{end},3} &= \begin{pmatrix} 0 \text{ N} \\ 0 \text{ N} \\ -16.03 \text{ N} \\ 0 \text{ Nm} \\ 0 \text{ Nm} \\ 0 \text{ Nm} \end{pmatrix} = \mathbf{F}_{\text{start},4}, \\ \mathbf{F}_{\text{end},4} &= \begin{pmatrix} 0 \text{ N} \\ 0 \text{ N} \\ 0 \text{ N} \\ 0 \text{ Nm} \\ 0 \text{ Nm} \\ 0 \text{ Nm} \end{pmatrix}. \end{aligned} \quad (4.33)$$

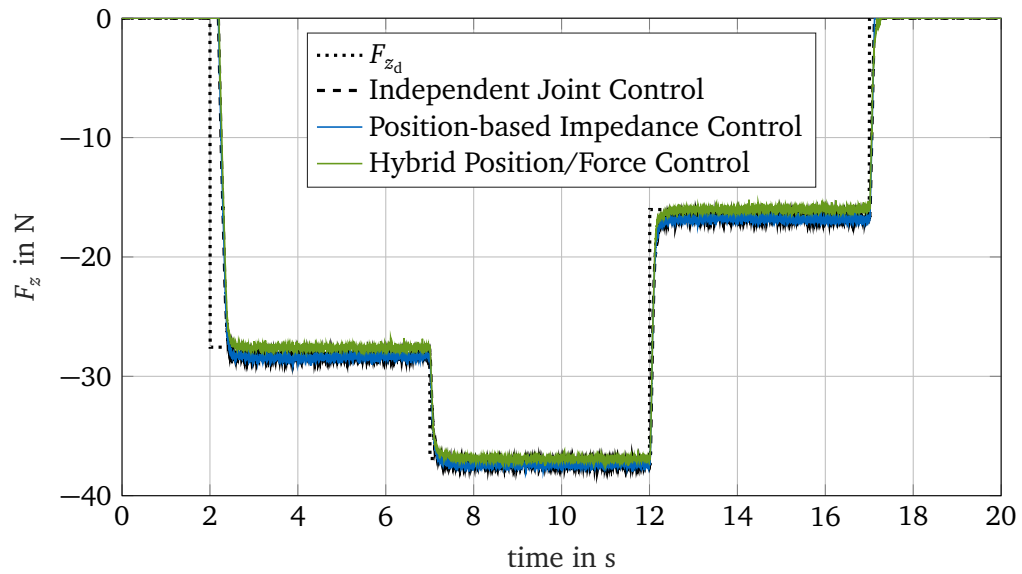
The values  $F_z$  result from measurements at the corresponding target poses and taking the average over 20000 sample steps. To be able to better compare results, once again independent joint control is used to move the TCP to the start pose  $\mathbf{x}_{\text{start},1}$ . We simultaneously change the control algorithm from independent joint control to hybrid position/force control or position-based impedance control as soon as  $\mathbf{x}_{\text{end},1}$  or  $\mathbf{F}_{\text{end},1}$  is reached and transmitted to the real-time system.

Figure 4.13 shows the resulting step responses of the test case.

In general, independent joint control, position-based impedance control and hybrid position/force control perform equally. Small differences result from inaccuracies in the measurements leading to the force/torque values in eq. (4.33). The main difference between hybrid position/force control and position-based impedance control is that during the last step in fig. 4.13, the curve of hybrid position/force control is not smooth resulting from the problems when switching from a contact task to a non-contact task discussed in fig. 4.5. Position-based impedance control as well as independent joint control on the other hand can easily handle moving into free space.



(a)



(b)

**Figure 4.13:** Comparison of independent joint control, position-based impedance control and hybrid position/force control regarding their step responses along (a) position  $z$  and (b) force  $F_z$



### Test Trajectory

Next, we use the test trajectory introduced in section 3.5 to compare independent joint control, position-based impedance control and hybrid position/force control. For the latter control concept, we once again specify the following compliance selection matrix:

$$\mathbf{S} = \text{diag}(001000) \quad (4.34)$$

and determine target force/torque values by measurements at the corresponding target poses and taking the average over 15000 sample points. Again, we use forward kinematics to compute the actual pose of the TCP in order to be able to easily rate the control schemes' performances.

We specify the pose and force/torque vectors of the test trajectory as well as the initial guess of Newton's method in the following way:

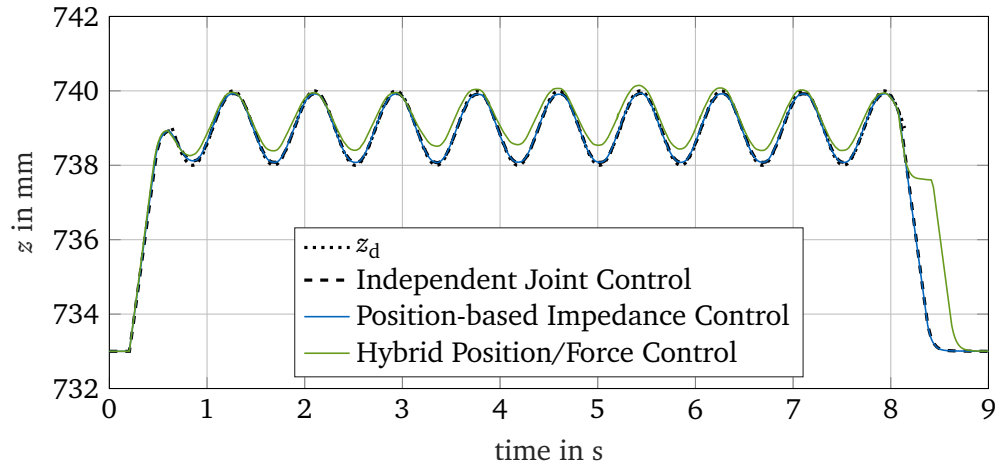
$$\begin{aligned} \mathbf{x}_{\text{start}} &= \begin{pmatrix} 0 \text{ mm} \\ 0 \text{ mm} \\ 733 \text{ mm} \\ 0 \text{ rad} \\ 0 \text{ rad} \\ 0 \text{ rad} \end{pmatrix} = \mathbf{x}_0, & \mathbf{F}_{\text{start}} &= \begin{pmatrix} 0 \text{ N} \\ 0 \text{ N} \\ 0 \text{ N} \\ 0 \text{ Nm} \\ 0 \text{ Nm} \\ 0 \text{ Nm} \end{pmatrix}, \\ \mathbf{x}_{\text{contact}} &= \begin{pmatrix} 0 \text{ mm} \\ 0 \text{ mm} \\ 739 \text{ mm} \\ 0 \text{ rad} \\ 0 \text{ rad} \\ 0 \text{ rad} \end{pmatrix}, & \mathbf{F}_{\text{contact}} &= \begin{pmatrix} 0 \text{ N} \\ 0 \text{ N} \\ -15.30 \text{ N} \\ 0 \text{ Nm} \\ 0 \text{ Nm} \\ 0 \text{ Nm} \end{pmatrix}, \\ \mathbf{x}_{\text{end}} &= \begin{pmatrix} 10 \text{ mm} \\ 0 \text{ mm} \\ 733 \text{ mm} \\ 0 \text{ rad} \\ 0 \text{ rad} \\ 0 \text{ rad} \end{pmatrix}, & \mathbf{F}_{\text{end}} &= \begin{pmatrix} 0 \text{ N} \\ 0 \text{ N} \\ 0 \text{ N} \\ 0 \text{ Nm} \\ 0 \text{ Nm} \\ 0 \text{ Nm} \end{pmatrix}, \end{aligned} \quad (4.35)$$

and set the parameters of the circle and sine wave trajectory to:

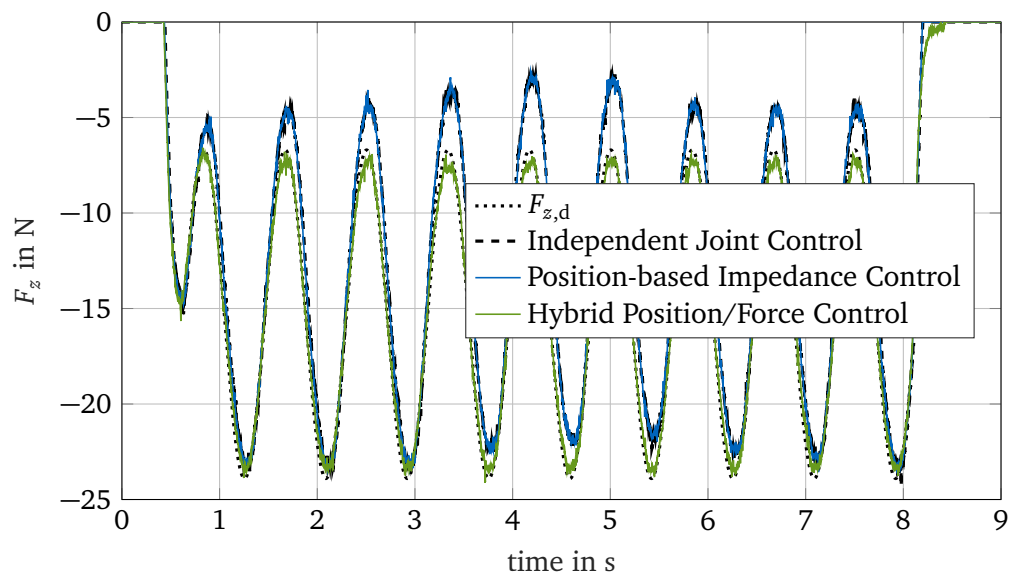
$$R = 5 \text{ mm}, A_x = 1 \text{ mm}, f_x = 2.4\pi \text{ Hz}, A_F = -8.6 \text{ N}, f_F = 2.4\pi \text{ Hz}, t_{\text{max}} = 2.5 \text{ s}. \quad (4.36)$$

Figure 4.14 shows the graphs for the actual position as well as the actual force in  $z$ -direction and the position of the TCP in the  $xy$ -plane of the Stewart platform.

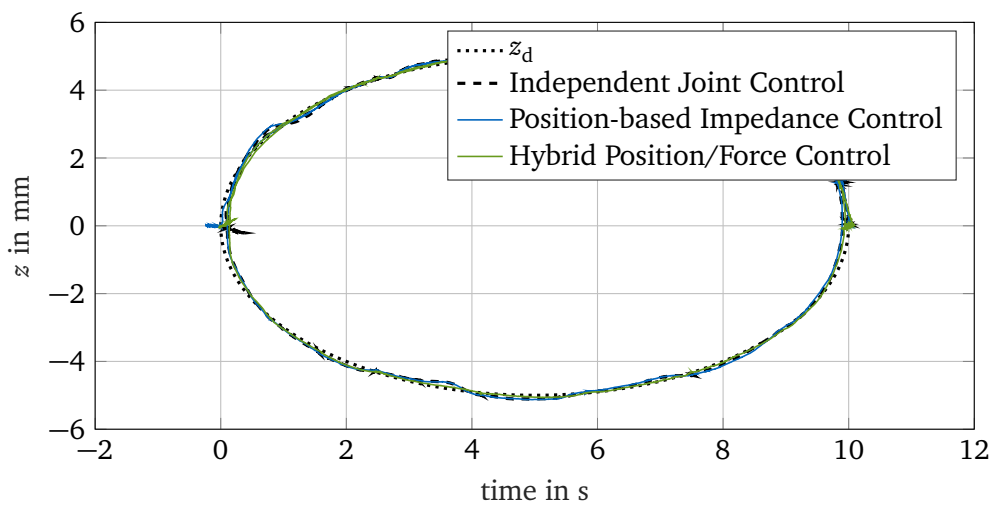
Firstly, we observe that the sine wave in fig. 4.14a for hybrid position/force control as well as the one in fig. 4.14b for position-based impedance control and independent joint control is not steady, but changes its amplitude and its upper and lower values. The reason for this is that the spring in the experimental setup reacts differently to loading and unloading and slightly deforms when following the trajectory. The deviations for hybrid position/force control appear in fig. 4.14a because the  $z$ -direction is force controlled instead of position controlled and thus, the control can only guarantee accurate behavior for the force  $F_z$ . As position-based impedance control as well as independent joint control purely control the position of the TCP, the deviations only occur in fig. 4.14b. Besides, differences between hybrid position/force control and independent joint control as well as position-based impedance control may result from inaccurate measurements of force values at the target poses to compute target force/torque vectors. Furthermore, the graphs once again show the difficulty of



(a)



(b)



(c)

**Figure 4.14:** Comparison of independent joint control, position-based impedance control and hybrid position/force control regarding the test trajectory (a) along position  $z$ , (b) along force  $F_z$  and (c) in the  $x$ - $y$ -plane

hybrid position/force control to perform a switch from contact tasks to non-contact tasks. When looking at fig. 4.14c, we determine that hybrid position/force control performs slightly better in following the circle trajectory than independent joint control and position-based impedance control. This can be traced back to the fact that hybrid position/force control uses separate controllers for force control actions along the  $z$ -direction and position control actions in the  $xy$ -plane. In independent joint control as well as position-based impedance control on the other hand, each  $x$ ,  $y$  and  $z$ -direction of the Stewart platform are position-controlled by the same controller. As a result, it is easier for hybrid position/force control to parallelly follow trajectories along different (de-)coupled directions. All together, all control schemes provide good trajectory tracking characteristics.

#### 4.4.2 Testing on Computational Costs

In this paragraph, we examine the computational costs for each independent joint control, position-based impedance control and hybrid position/force control. An appropriate measure for this is the turnaround time. It indicates the time needed to perform all tasks for the whole system within one sample step. For this test we reuse the target trajectory of the multiple step response analysis of section 4.4.1 as it contains motion control in contact tasks, non-contact tasks as well as the transition between contact and non-contact tasks. However, it is crucial to not compute the actual pose of the TCP by means of forward kinematics as this is not part of the actual control schemes. Of course, hybrid position/force control still applies Newton's method for control purposes.

Figure 4.15 presents the turnaround time for each control approach. Firstly, we observe that

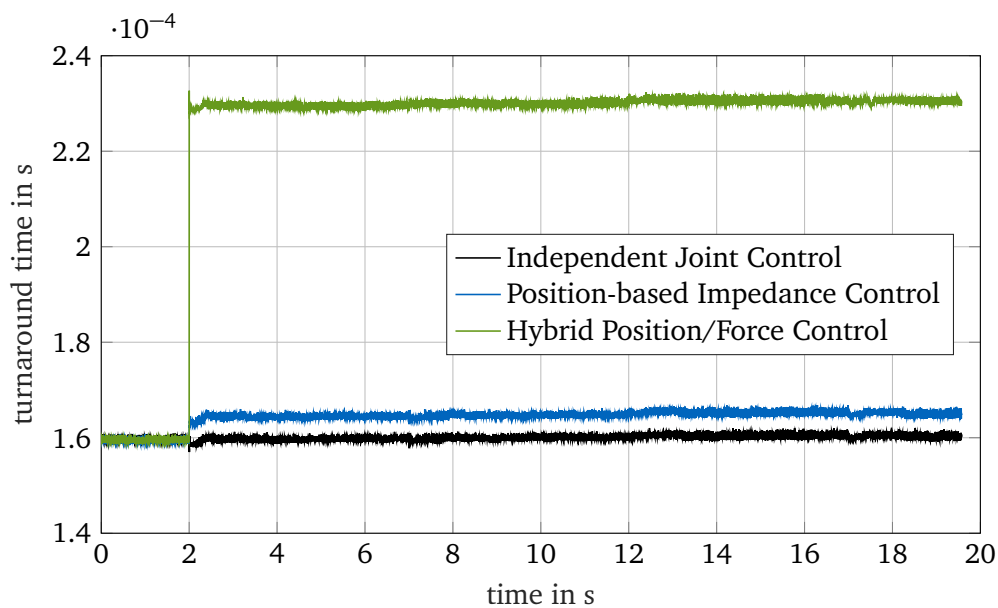


**Figure 4.15:** Comparison of independent joint control, position-based impedance control and hybrid position/force control regarding their turnaround time

the turnaround time is always lower than the sample time  $T_s = 1$  ms. This is very important as otherwise, a task overflow would arise because not all tasks could be completed during one sample step. Furthermore, the curves for position-based impedance control as well as hybrid position/force control exhibit a jump after two seconds. At this time, the control algorithm is changed from independent joint control to hybrid position/force control or position-based impedance control as explained in the description of multiple step response analysis in sec-

tion 4.4.1. So, actually up to two seconds, the control algorithm used is independent joint control for all three curves. After two seconds, the turnaround time stays constant for each of the control schemes. This means that the type of control, i.e. non-contact or contact task control, does not influence computational costs. Overall, computational costs for position-based impedance control are slightly larger than for independent joint control. The reason for this is that position-based impedance control is based on independent joint control, but expands it basically by adding the target admittance behavior transfer function matrix  $\mathbf{G}_{\Delta x, F}$ . Figure 3.7 illustrates the extension. Hybrid position/force control, however, leads to a much larger increase in the turnaround time. The critical part herein is forward kinematics because in every sample step, several Newton iterations have to be computed. To sum up, in terms of computational costs, position-based impedance control is preferred to hybrid position/force control.

#### 4.4.3 Validation of both Control Schemes

Until now, we have focused on control actions along the  $z$ -direction for analysis and comparison. However, the compliant motion control schemes presented have been realized in a way that they can equally handle control along any other DOF of the Stewart platform as well as superposed control along multiple DOFs. This section aims at validating and illustrating this statement. Therefore, we first investigate the behavior of the spring in the experimental setup along other DOFs. After that, we perform a step response analysis along the  $x$ -direction as well as a superposed step response analysis along the  $x$ - and  $z$ -direction of the Stewart platform. As already mentioned in section 3.1, a new lower mass is used for the following tests. However, this does not affect the behavior of the robot-environment interaction in comparison to the old one.

##### Behavior of the Spring along other DOFs

The experimental setup has primarily been developed for usage and testing of the Stewart platform along its  $z$ -direction. The spring is used to model a flexible, compressible environment. As we know its stiffness  $k_E = 10000 \frac{\text{N}}{\text{m}}$ , we know that a deviation of 1 mm corresponds to a force of 10 N. This only holds true for the  $z$ -direction because it is a compression spring. Along other DOFs we cannot easily determine the relationship between force and deviation values. Furthermore, we need to prestress the spring by always guaranteeing that the force in  $z$ -direction is nonzero. If we did not do that, the spring would jump out of its support. Also, the spring deforms when moving it for example in  $x$ -direction while simultaneously prestressing it along the  $z$ -direction. Overall, the behavior of the spring and thus the force/torque measurement along other DOFs than the  $z$ -direction are unpredictable for the existing setup. As a result, we have to experimentally analyze it. Therefore, we move the TCP from a start pose  $\mathbf{x}_{\text{start}}$  to an end pose  $\mathbf{x}_{\text{end}}$  by applying independent joint control. Every 15 s, we move one millimeter further along the positive  $x$ -direction. We specify the parameters in the following way:

$$\mathbf{x}_{\text{start}} = \begin{pmatrix} 75 \text{ mm} \\ 52 \text{ mm} \\ 741 \text{ mm} \\ 0 \text{ rad} \\ 0 \text{ rad} \\ 0 \text{ rad} \end{pmatrix}, \quad \mathbf{x}_{\text{end}} = \begin{pmatrix} 87 \text{ mm} \\ 52 \text{ mm} \\ 741 \text{ mm} \\ 0 \text{ rad} \\ 0 \text{ rad} \\ 0 \text{ rad} \end{pmatrix}. \quad (4.37)$$

We set the force/torque offset at

$$\mathbf{x} = \left( 75 \text{ mm} \quad 52 \text{ mm} \quad 736 \text{ mm} \quad 0 \text{ rad} \quad 0 \text{ rad} \quad 0 \text{ rad} \right)^T. \quad (4.38)$$

Figure 4.16 shows the relationship between measured force  $F_x$  and  $F_z$ . The sequence of

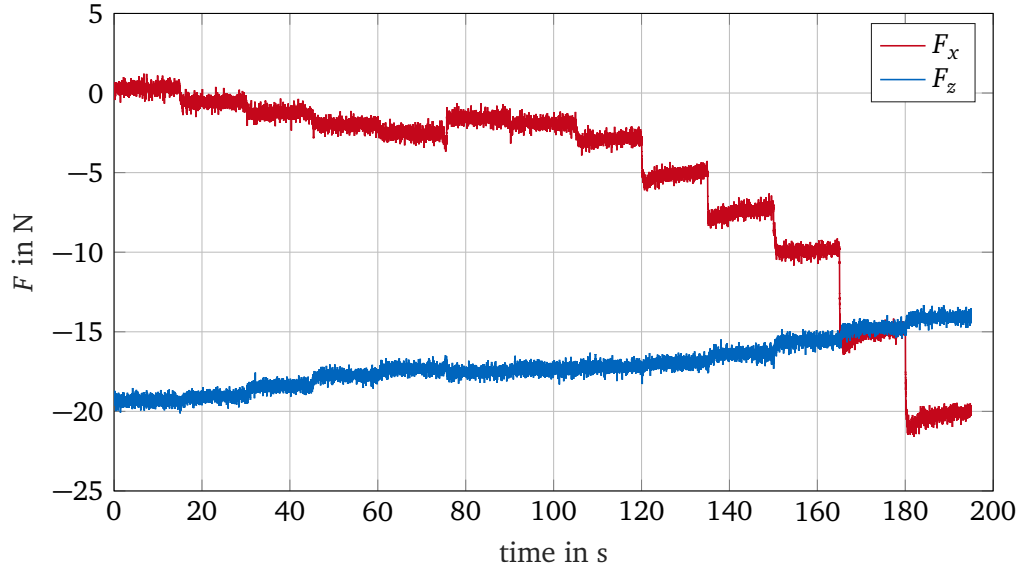


**Figure 4.16:** Measured forces  $F_x$  and  $F_z$  for increasing robot-environment interaction in  $x$ -direction

$F_x$  is strongly nonlinear and unpredictable. Besides, increasing  $F_x$  leads to a decrease in the prestressing of the spring as the spring bends. These effects make further testing in  $x$ -direction more difficult. Also keep in mind that the extension plate representing a barrier along the  $x$ -direction is mounted in an area of the Stewart platform's workspace, where the manipulator has a strongly nonlinear behavior and where control actions are not as accurate as in the tests in former sections.

#### Multiple Step Response Analysis along $x$ -Direction

The following test is performed in analogy to the multiple step response analysis in section 4.4.1. Again, we create target trajectories that include a switch from a non-contact to a contact task and vice versa as well as operation in a contact task. We choose:

$$\mathbf{x}_{\text{start},1} = \begin{pmatrix} 75 \text{ mm} \\ 52 \text{ mm} \\ 741 \text{ mm} \\ 0 \text{ rad} \\ 0 \text{ rad} \\ 0 \text{ rad} \end{pmatrix}, \quad \mathbf{x}_{\text{end},1} = \mathbf{x}_{\text{start},2} = \begin{pmatrix} 85 \text{ mm} \\ 52 \text{ mm} \\ 741 \text{ mm} \\ 0 \text{ rad} \\ 0 \text{ rad} \\ 0 \text{ rad} \end{pmatrix}, \quad (4.39)$$

$$\mathbf{x}_{\text{end},2} = \mathbf{x}_{\text{start},3} = \begin{pmatrix} 75 \text{ mm} \\ 52 \text{ mm} \\ 741 \text{ mm} \\ 0 \text{ rad} \\ 0 \text{ rad} \\ 0 \text{ rad} \end{pmatrix}.$$

We present these target poses to the system one after another and hold each one for 10 s. The force/torque offset is set at

$$\mathbf{x} = ( 75 \text{ mm} \quad 52 \text{ mm} \quad 736 \text{ mm} \quad 0 \text{ rad} \quad 0 \text{ rad} \quad 0 \text{ rad} )^T. \quad (4.40)$$

So, the first step moves the TCP from a non-contact task to a contact task, the next one takes place in a contact task and the last one leads back to a non-contact task. For Newton's method, we use the following arbitrary initial guess:

$$\mathbf{x}_0 = \begin{pmatrix} 74 \text{ mm} \\ 52 \text{ mm} \\ 741 \text{ mm} \\ 0 \text{ rad} \\ 0 \text{ rad} \\ 0 \text{ rad} \end{pmatrix}. \quad (4.41)$$

As we want to perform the analysis along the  $x$ -direction of the Stewart platform, we have to define the following compliance selection matrix for hybrid position/force control:

$$\mathbf{S} = \text{diag}(100000). \quad (4.42)$$

By measuring forces at the target poses and taking the average over multiple sample steps, we receive:

$$\mathbf{F}_{\text{start},1} = \begin{pmatrix} 0 \text{ N} \\ 0 \text{ N} \\ -17.32 \text{ N} \\ 0 \text{ Nm} \\ 0 \text{ Nm} \\ 0 \text{ Nm} \end{pmatrix}, \quad \mathbf{F}_{\text{end},1} = \mathbf{F}_{\text{start},2} = \begin{pmatrix} -7.86 \text{ N} \\ 0 \text{ N} \\ -13.58 \text{ N} \\ 0 \text{ Nm} \\ 0 \text{ Nm} \\ 0 \text{ Nm} \end{pmatrix}, \quad (4.43)$$

$$\mathbf{F}_{\text{end},2} = \mathbf{F}_{\text{start},3} = \begin{pmatrix} 0 \text{ N} \\ 0 \text{ N} \\ -17.32 \text{ N} \\ 0 \text{ Nm} \\ 0 \text{ Nm} \\ 0 \text{ Nm} \end{pmatrix}.$$

Note, that the values  $F_z$  are actually not used for control because of the above specification of the compliance selection matrix. Figure 4.17 shows the resulting actual positions and forces along the  $x$ - and  $z$ -direction of the Stewart platform. Position-based impedance control and independent joint control lead to equal dynamic behavior of the system, whereas the step responses of hybrid position/force control differ from the ones of independent joint control and position-based impedance control. Most of the differences result from the inaccurate behavior of the spring and thus inaccurate force measurement which leads to a bad specification of the target force/torque values in eq. (4.43). On top of that, the small metal plate in fig. 3.1 is not perfectly fixed because I only used Gaffer tape as a workaround which also brings some inaccuracy into the system. Figure 4.17c shows that the difficulty of switching from a contact task to a non-contact task is also existent in  $x$ -direction. All together, the graphs demonstrate that all developed control schemes also work along single other DOFs of the Stewart platform. However, exact statements cannot be made because of the bad experimental setup.

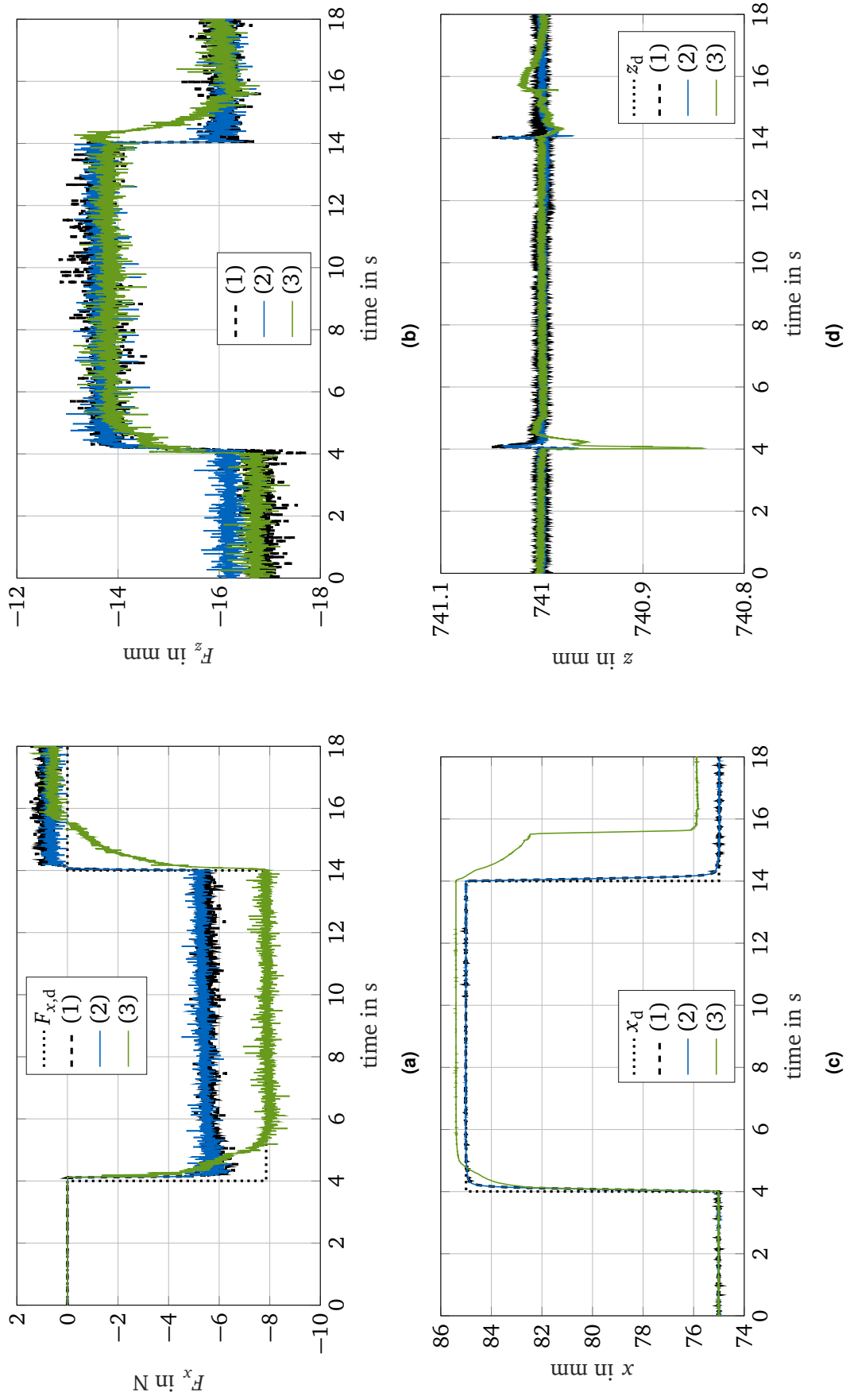


**Figure 4.17:** Comparison of (1) independent joint control, (2) position-based impedance control and (3) hybrid position/force control regarding a Heaviside step function in  $x$ -direction: (a)  $F_x$ , (b)  $F_z$ , (c)  $x$ , (d)  $z$

### Superposed Multiple Step Response Analysis along $x$ - and $z$ -Direction

In a final step, we combine control along the  $x$ -direction with control along the  $z$ -direction. Therefore, we apply once again a multiple step response analysis. We maintain the offset pose and the initial guess for Newton's method from the previous paragraph. However, as we have seen in the former test, directly comparing position-based impedance control and hybrid position/force control is difficult because of the bad experimental setup. Thus, instead of measuring forces at the target pose values, we separately define target pose and force/torque vectors. For the desired poses of the TCP, we set:

$$\begin{aligned}
 \mathbf{x}_{\text{start},1} &= \begin{pmatrix} 75 \text{ mm} \\ 52 \text{ mm} \\ 741 \text{ mm} \\ 0 \text{ rad} \\ 0 \text{ rad} \\ 0 \text{ rad} \end{pmatrix}, & \mathbf{x}_{\text{end},1} &= \begin{pmatrix} 85 \text{ mm} \\ 52 \text{ mm} \\ 742 \text{ mm} \\ 0 \text{ rad} \\ 0 \text{ rad} \\ 0 \text{ rad} \end{pmatrix} = \mathbf{x}_{\text{start},2}, \\
 \mathbf{x}_{\text{end},2} &= \begin{pmatrix} 87 \text{ mm} \\ 52 \text{ mm} \\ 743 \text{ mm} \\ 0 \text{ rad} \\ 0 \text{ rad} \\ 0 \text{ rad} \end{pmatrix} = \mathbf{x}_{\text{start},3}, & \mathbf{x}_{\text{end},3} &= \begin{pmatrix} 73 \text{ mm} \\ 52 \text{ mm} \\ 741 \text{ mm} \\ 0 \text{ rad} \\ 0 \text{ rad} \\ 0 \text{ rad} \end{pmatrix} = \mathbf{x}_{\text{start},4}.
 \end{aligned} \tag{4.44}$$

For hybrid position/force control, we define the compliance selection matrix in a way that both  $x$ -direction and  $z$ -direction are force-controlled in contact tasks:

$$\mathbf{S} = \text{diag}(101000) \tag{4.45}$$

Besides, we specify the following target force/torque values:

$$\begin{aligned}
 \mathbf{F}_{\text{start},1} &= \begin{pmatrix} 0 \text{ N} \\ 0 \text{ N} \\ -20 \text{ N} \\ 0 \text{ Nm} \\ 0 \text{ Nm} \\ 0 \text{ Nm} \end{pmatrix}, & \mathbf{F}_{\text{end},1} &= \begin{pmatrix} -8 \text{ N} \\ 0 \text{ N} \\ -25 \text{ N} \\ 0 \text{ Nm} \\ 0 \text{ Nm} \\ 0 \text{ Nm} \end{pmatrix} = \mathbf{F}_{\text{start},2}, \\
 \mathbf{F}_{\text{end},2} &= \begin{pmatrix} -15 \text{ N} \\ 0 \text{ N} \\ -32 \text{ N} \\ 0 \text{ Nm} \\ 0 \text{ Nm} \\ 0 \text{ Nm} \end{pmatrix} = \mathbf{F}_{\text{start},3}, & \mathbf{F}_{\text{end},3} &= \begin{pmatrix} 0 \text{ N} \\ 0 \text{ N} \\ -20 \text{ N} \\ 0 \text{ Nm} \\ 0 \text{ Nm} \\ 0 \text{ Nm} \end{pmatrix} = \mathbf{F}_{\text{start},4}.
 \end{aligned} \tag{4.46}$$

Both the step responses for independent joint control, position-based impedance control as well as hybrid position/force control are displayed in fig. 4.18. However, keep in mind that only independent joint control and position-based impedance control follow the same target trajectories, while hybrid position/force control receives different target input signals. Overall, the graphs confirm that the control schemes also work for superposed control along multiple DOFs. However, again, hybrid position force control has problems switching from a contact task to a non-contact task, both along  $x$ - and  $z$ -direction.



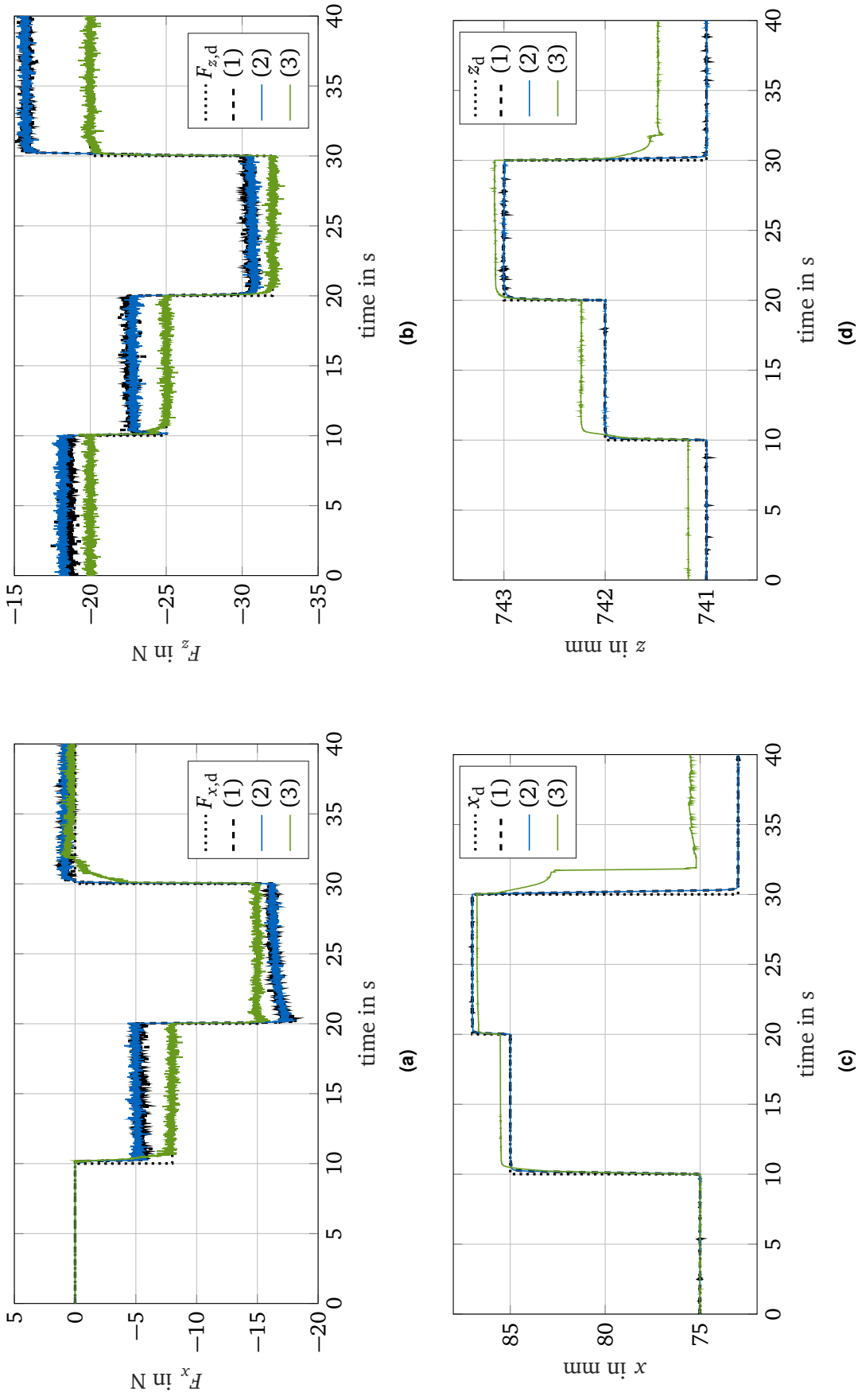


**Figure 4.18:** Comparison of (1) independent joint control, (2) position-based impedance control and (3) hybrid position/force control regarding a Heaviside step function in  $x$ - and  $z$ -direction: (a)  $F_x$ , (b)  $F_z$ , (c)  $x$ , (d)  $z$



## Chapter 5

# Comparison of Compliant Motion Control Schemes

In the previous chapter, we ran multiple tests in order to study and better understand position-based impedance control as well as hybrid position/force control. We now sum up all important results by comparing both control schemes. First of all, in section 5.1 we look at the approaches from a theoretical point of view. Then, in section 5.2 we consider implementation aspects and computational costs. Finally, in section 5.3 we focus on their influence on the system's behavior. All findings are summarized in table 5.1 including references to corresponding explanations. The table helps to compare hybrid position/force control with position-based impedance control by means of multiple criteria.

### 5.1 Theoretical Comparison

One major theoretical difference between hybrid position/force control and position-based impedance control is that the former one belongs to direct force control, while the latter one is classified into the category of indirect force control. Thus, in hybrid position/force control, both the Stewart platform's position as well as the interaction forces between the TCP and its environment are directly controlled due to explicit closure of a force feedback loop. On the other hand, in position-based impedance control, control of force or motion alone is considered inadequate and thus the dynamical relationship between contact forces and motion parameters is controlled. As a result, in position-based impedance control all DOFs are controlled by the same controller, while in hybrid position/force control, we distinguish DOFs which are position- and force-controlled by either a pure position or a pure force controller. In a contact task, the user can directly specify whether a DOF is position- or force-controlled by defining a compliance selection matrix. The hybrid position/force control approach is furthermore based on the assumption that the manipulator is kinematically coupled to its environment, but does not dynamically interact with it. As a result, the set of position constraints restricting the robot's motion has to be orthogonal to the set of force constraints. Thus, the mechanical work exchanged by the manipulator and its environment is always zero, whereas for position-based impedance control it is generally unequal to zero. Another big difference is that for position-based impedance control, we have to specify a target pose trajectory for every DOF whereas for hybrid position/force control, we need both a target pose as well as a target force trajectory. This leads to the fact that hybrid position/force control is preferred to position-based impedance control whenever a concrete force/torque value shall be reached. The control parameters to be tuned for hybrid position control are the parameters of its position, force and velocity controller and for position-based impedance control the parameters of the position and velocity controller of the independent joint control as well as the mass/inertia, damping and stiffness matrices which define the target admit-

tance behavior. The physical interpretation of position-based impedance control explained in fig. 3.8 illustrates that the control scheme requires some knowledge about the environment if we want to achieve a specific approach to  $\mathbf{x}_{\text{stat}}$ , whereas for hybrid position/force control, the data from a force/torque sensor is enough. Besides, different safety functions are required. While for hybrid position/force control, we have to ensure that the forward kinematics algorithm does not become ill-conditioned, we have to forbid a controller output equal to NaN in the case of position-based impedance control as section 4.3.1 showed that this output may occur for certain combinations of the parameters  $\mathbf{M}$ ,  $\mathbf{D}$ ,  $\mathbf{K}$ .

## 5.2 Implementation and Computational Costs

The hybrid position/force controller itself consists of a pure position as well as a pure force controller and a velocity controller, arranged in a PPI-cascade (fig. 3.5). Further components of hybrid position/force control are the data processing steps described in section 3.2, the calculation of the position and force selection matrices, a position and force trajectory generation module, the implementation of forward kinematics due to Newton's method as well as safety functions (fig. 3.6). Position-based impedance control is made up of an independent joint controller, a position trajectory generation module, the implementation of inverse kinematics, data processing as well as safety functions and the implementation of the target admittance behavior within a force feedback compensator (fig. 3.7). As a result, based on an already existing independent joint controller, the implementation effort is much lower for position-based impedance control than for hybrid position/force control. Furthermore, computational costs are also lower for position-based impedance control as the control scheme does not require forward kinematics. For a parallel robot like the Stewart platform, forward kinematics cannot be computed analytically and are thus solved numerically, usually using Newton's method which leads to high computational costs because multiple iterations have to be executed in each sample step. However, this is only true for a parallel robot. For a serial robot, inverse kinematics is the crucial part that has to be solved numerically.

## 5.3 Differences in Behavior

In hybrid position/force control, both position and interaction forces between the TCP and its environment are directly controlled based on the specification of the user-defined compliance selection matrix. Thus, the stationary pose values of  $\mathbf{x}_{\text{stat}}$  along the position-controlled DOFs as well as the stationary force values of  $\mathbf{F}_{\text{stat}}$  along the force-controlled DOFs are reached. As reaching those values is the primary aim of the control concept, hybrid position/force control behaves rather stiff with reference to robot-environment interaction. On the other hand, in position-based impedance control, the dynamical relationship between contact forces and motion parameters is controlled. As the inner control loop of position-based impedance control is a position control, the stationary pose values of  $\mathbf{x}_{\text{stat}}$  are reached quite exactly. However, as noted in section 2.2.1, it only achieves high positioning accuracy when using a stiff target admittance. Section 4.3.1 also showed that a compliant robot-environment interaction behavior leads to less positioning accuracy. Thus, tuning a position-based impedance control is always a trade-off between positioning accuracy and compliance of the robot. Furthermore, the control approach does not allow to directly influence the interaction force/torque values between the TCP and its environment. Instead, contact forces and torques arise due to the admittance behavior of the manipulator and the characteristics of the environment.

Both compliant motion control schemes generally achieve good performance when following a target trajectory. Nevertheless, the major problem regarding hybrid position/force control is that it has difficulties when switching from a contact to a non-contact task as described in section 4.2.2. On the other hand it can better handle problems where multiple trajectory following tasks are superposed, e.g. the circle in the  $xy$ -plane combined with the sine wave in  $z$ -direction in section 4.4.1. Furthermore, the different control parameters of both schemes allow to construct particular forms of step responses. A variation of the force and position controller parameter in hybrid position/force control basically does not change the shape of the step response, but it allows to vary settling time, rapidity of the system response and to avoid overshooting. By an adjustment of the mass/inertia, damping and stiffness matrix of position-based impedance control however, the shape of the step response can be modified more in detail, while a variation of the position control parameter of the independent joint control within position-based impedance control produces the same effects as for hybrid position/force control.

Overall, the tests confirmed our theoretical interpretation of the position-based impedance control as a mass-springer-damper system illustrated in fig. 3.8 which makes it relatively easy to tune its control parameters as we are familiar with the behavior of mass-spring-damper systems. Hybrid position/force control can be descriptively explained with the help of C-surfaces, knowing that DOFs along the C-surface's tangents are position-controlled and DOFs along the C-surface's normals are force-controlled. The window-example in section 2.2.3 helps to better illustrate this approach.

To sum up, both position-based impedance control and hybrid position/force control have their benefits and drawbacks. Which one to choose depends on the specific use case and requirements that have to be met. For a parallel robot, position-based impedance control is preferred to hybrid position/force control in terms of computational costs. Thus, in very time-critical applications, it might be safer to use position-based impedance control. Additionally, when an existing position controller shall be extended by a compliant motion control method or when many switches between contact tasks and non-contact tasks are to be assumed, one would probably choose position-based impedance control. Moreover, whenever a manipulator shall be able to move compliantly within a specified region of attraction, again position-based impedance control would be the more reasonable choice. As a result, it is especially suitable for medical applications and human-robot-interaction tasks. On the other hand, whenever a specific force/torque value shall be reached by the TCP of a robot or when many target trajectories are superposed, hybrid position/force control may perform better. This makes it a reasonable approach for e.g. machine tools.

**Table 5.1:** Comparison of hybrid position/force control with position-based impedance control

critierion	hybrid position/force control	position-based impedance control
classification (fig. 2.1)	direct force control	indirect force control
assumption (section 2.2)	pure control of force or motion alone is adequate	pure control of force or motion alone is inadequate
required modules (fig. 3.6, fig. 3.7)	hybrid position/force controller, trajectory generation, data processing, forward kinematics, calculation of selection matrices, safety functions	independent joint controller, trajectory generation, data processing, inverse kinematics, force feedback compensator, safety functions
force/torque sensor (fig. 3.5, fig. 3.7)	required	required
required controllers (fig. 3.5, fig. 3.7)	position, force and velocity controller	independent joint controller (position and velocity controller), force feedback compensator
control mode (fig. 3.5, fig. 3.7)	workspace control for position and force controller, joint space control for velocity controller	independent joint controller in joint space, force feedback compensator in workspace
control parameters (fig. 3.5, fig. 3.7)	$K_{P,v}, K_{I,v}, K_{P,p}, K_{P,F}$	$K_{P,v}, K_{I,v}, K_{P,p}, \mathbf{M}, \mathbf{D}, \mathbf{K}$
safety functions (section 2.3.2, section 3.3, section 3.4)	$\dot{b}_{\max}, i_{\max}$ , leg length and cardan joint angle limits, task overrun, force/torque limits, avoiding ill-conditioned forward kinematics algorithm	$\dot{b}_{\max}, i_{\max}$ , leg length and cardan joint angle limits, task overrun, force/torque limits, avoiding NaN
target trajectories (fig. 3.5, fig. 3.7)	$\mathbf{x}_d, \mathbf{F}_d$ , both specified in workspace	$\mathbf{x}_d$ , specified in workspace
implementation effort (fig. 3.5, fig. 3.7)	rather high	very low
knowledge about environment (section 3.4)	not required	required to tune $\mathbf{M}, \mathbf{D}, \mathbf{K}$ to achieve a specific approach to $\mathbf{x}_{\text{stat}}$
computational costs (section 4.4.2)	rather high	rather low
$\mathbf{x}_{\text{stat}}$ (chapter 4)	reaches $\mathbf{x}_d$ along position-controlled DOFs	reaches a region around $\mathbf{x}_d$ and compliantly moves in the calculated direction
$\mathbf{F}_{\text{stat}}$ (chapter 4)	reaches $\mathbf{F}_d$ along force-controlled DOFs	cannot be influenced directly
target tracking (section 4.2.2, section 4.4.1)	good performance also for superposed trajectories, but difficulties when switching from a contact to a non-contact task	good performance
compliance	stiff	rather compliant
interpretation (section 3.3, section 3.4)	C-surfaces	mass-spring-damper system
industrial applications	machine tools	medical applications, human-robot-interaction

## Chapter 6

# Conclusion and Outlook

### 6.1 Conclusion

The aim of this thesis was to design control schemes for two representatives of compliant motion control, namely hybrid position/force control and an impedance control approach. In this regard, an appropriate impedance control scheme should be chosen and both control schemes should be implemented, tested, validated and compared on the Stewart platform at the Chair of Applied Mechanics.

Therefore, we developed an overview of compliant motion control at the beginning of the thesis in section 2.2. This helped us to decide to choose position-based impedance control within all possible impedance control schemes because it can be easily built upon the existing independent joint control. Furthermore, we summed up the characteristics of a parallel robot, including its kinematics, in section 2.1 and presented the Chair's Stewart platform with all its components and functionalities in section 2.3.

Based on this knowledge, we designed an appropriate hybrid position/force control scheme in section 3.3 and a position-based impedance control scheme in section 3.4 and implemented them on the Stewart platform. We also considered necessary data processing of the force/torque sensor signal in section 3.2 and extended the experimental setup in section 3.1 to be able to test the implemented control schemes also along the robot's  $x$ -direction. We modeled the compliant environment by a mass-spring system shown in fig. 2.10, fig. 2.11 and fig. 3.1 which can exert forces against two different metal plates along the  $x$ - and  $z$ -direction of the Stewart platform.

Then, we ran multiple tests using step response analysis and a specific test trajectory we had developed in section 3.5. The experiments helped us to study the influence of the controller parameters on the system behavior in section 4.2.1 and section 4.3 and rate the performance of the control schemes accomplishing different control tasks in section 4.4.1 as well as comparing their computational costs in section 4.4.2. Because of the characteristics of the experimental setup, we performed all tests along the  $z$ -direction of the Stewart platform. However, we could validate both control schemes in section 4.4.3 by showing that they basically also work along the robot's  $x$ -direction and for superposed control tasks. To sum up, the results of the experiments could confirm our theoretical interpretation of the position-based impedance control as a mass-spring-damper system illustrated in fig. 3.8. Besides, we found out that the hybrid position/force control has some difficulties switching from a contact task to a non-contact task, explained in section 4.2.2 and that the computational costs using hybrid position/force control are larger than those applying position-based impedance control because of the forward kinematics algorithm, shown in section 4.4.2.

Finally, in chapter 5, we used all results to compare hybrid position/force control and position-based impedance control in terms of their characteristics, implementations and computa-

tional costs as well as their influence on the system behavior. We explained the benefits and drawbacks of both position-based impedance control and hybrid position/force control and concluded that deciding which concept to prefer depends on the specific use case and requirements that have to be met. Nevertheless, we were able to come up with some decision guidance for some characteristic requirements. Position-based impedance control is suitable for control tasks which consist of many switches between contact tasks and non-contact tasks, which desire an existing position controller to be extended by a compliant motion control method or which require compliant movement within a specified region of attraction, e.g. needed in medical applications and human-robot-interaction tasks. On the other hand, whenever the Stewart platform has to follow a certain force/torque trajectory, for example as a machine tool, it is reasonable to apply hybrid position/force control to directly control force and torque values. In very time-critical applications, it might be safer to use position-based impedance control for parallel robots because of its lower computational costs.

## 6.2 Outlook

All together, we successfully designed and implemented hybrid position/force control as well as position-based impedance control on the Chair's Stewart platform. However, testing gave some hints for further improvements. In subsequent student theses, it would be reasonable to further investigate the following aspects:

- Firstly, an extended experimental setup may be developed in order to be able to properly test robot-environment interaction control along any DOF of the Stewart platform and to repeat the studies in section 4.4.3 without any unpredictable effects in the measurement data.
- Another interesting point would be to put effort on developing a universal method to overcome the problem discussed in section 4.2.2, appearing whenever switching from a contact task to a non-contact task using hybrid position/force control.
- Besides, the tuning of the control parameters, which has been done experimentally in the context of this thesis, could be seen from a more theoretical point of view, e.g. by aiming at finding optimal parameters.
- It may be interesting to investigate the effects of using different parameter values for different DOFs of the Stewart platform, for example for the mass/inertia, damping and stiffness matrices in position-based impedance control.
- On top of that, more advanced control schemes may be implemented and examined, for example hybrid impedance control [2].
- Finally, the findings gathered withing this work can be further studied and applied on the Real-time Substructuring approach in the context of research for Christina Insam's dissertation, both for position-based impedance control [4] and hybrid position/force control [21].



## Bibliography

- [1] Albu-Schäffer, A., Haddadin, S., Ott, C., Stemmer, A., Wimböck, T., and Hirzinger, G. “The DLR lightweight robot: design and control concepts for robots in human environments”. In: *Industrial Robot: an international journal* 34.5 (2007), pp. 376–385.
- [2] Anderson, R. J. and Spong, M. W. “Hybrid impedance control of robotic manipulators”. In: *IEEE Journal on Robotics and Automation* 4.5 (1988), pp. 549–556.
- [3] Arevalo, J. C. and Garcia, E. “Impedance control for legged robots: An insight into the concepts involved”. In: *IEEE Transactions on Systems, Man, and Cybernetics, Part C (Applications and Reviews)* 42.6 (2012), pp. 1400–1411.
- [4] Boge, T. and Ma, O. “Using advanced industrial robotics for spacecraft rendezvous and docking simulation”. In: *2011 IEEE international conference on robotics and automation*. IEEE. 2011, pp. 1–4.
- [5] Calanca, A., Muradore, R., and Fiorini, P. “A review of algorithms for compliant control of stiff and fixed-compliance robots”. In: *IEEE/ASME Transactions on Mechatronics* 21.2 (2016), pp. 613–624.
- [6] Craig, J. J. and Raibert, M. H. “A systematic method of hybrid position/force control of a manipulator”. In: *Computer Software and Applications Conference, 1979. Proceedings. COMPSAC 79. The IEEE Computer Society’s Third International*. IEEE. 1979, pp. 446–451.
- [7] Fritz Schunk GmbH. *Montage- und Bedienungsanleitung für 6 Achsen Kraft- / Momentensensor Type FTS*. Lauffen/Neckar, Dec. 1992.
- [8] Hogan, N. “Impedance control: An approach to manipulation: Part I-Theory”. In: *Journal of Dynamic Systems, Measurement and Control, Transactions of the ASME* 107.1 (1985), pp. 1–7.
- [9] Hogan, N. “Impedance control: An approach to manipulation: Part II-Implementation”. In: *Journal of Dynamic Systems, Measurement and Control, Transactions of the ASME* 107.1 (1985), pp. 8–16.
- [10] Hogan, N. “Impedance control: An approach to manipulation: Part III-Applications”. In: *Journal of Dynamic Systems, Measurement and Control, Transactions of the ASME* 107.1 (1985), pp. 17–24.
- [11] Insam, C., Bartl, A., and Rixen, D. J. *A STEP TOWARDS TESTING OF FOOT PROSTHESES USING REAL-TIME SUBSTRUCTURING (RTS)*. Tech. rep. Chair of Applied Mechanics, Faculty of Mechanical Engineering, Technical University of Munich, 2018.
- [12] Lawrence, D. A. “Impedance control stability properties in common implementations”. In: *Robotics and Automation, 1988. Proceedings., 1988 IEEE International Conference on*. IEEE. 1988, pp. 1185–1190.
- [13] Liu, Y.-C., Jin, M.-H., and Liu, H. “Joint torque-based Cartesian impedance control with friction compensations”. In: *Journal of Southeast University (English Edition)* 24.4 (2008), pp. 492–497.

- [14] Lu, Z. and Goldenberg, A. A. “Robust impedance control and force regulation: Theory and experiments”. In: *The International journal of robotics research* 14.3 (1995), pp. 225–254.
- [15] Lunze, J. “Regelungstechnik 1 - Systemtheoretische Grundlagen, Analyse und Entwurf einschleifiger Regelungen”. In: vol. 11. Springer Vieweg, 2016. Chap. 13.1.3 Kaskadenregelung, pp. 587–589.
- [16] Mason, M. T. “Compliance and force control for computer controlled manipulators”. In: *IEEE Transactions on Systems, Man, and Cybernetics* 11.6 (1981), pp. 418–432.
- [17] Miomir, V., Dragoljub, S., Yury, E., and Dusko, K. “Dynamics And Robust Control Of Robot-environment Interaction”. In: vol. 2. World Scientific, 2009. Chap. 1 Control of Robots in Contact Tasks: A Survey, pp. 1–76.
- [18] Müller, T.-C. “Entwicklung einer entkoppelten Einzelgelenkregelung für einen Hexapoden”. Semesterarbeit. Chair of Applied Mechanics, Faculty of Mechanical Engineering, Technical University of Munich, 2017.
- [19] Paynter, H. M. *Analysis and Design of Engineering Systems - Class Notes for M.I.T. Course 2.751*. The M.I.T. Press, Cambridge, Massachusetts, 1961.
- [20] Raibert, M. H. and Craig, J. J. “Hybrid position/force control of manipulators”. In: *Journal of Dynamic Systems, Measurement, and Control* 103.2 (1981), pp. 126–133.
- [21] Reinhorn, A., Sivaselvan, M., Liang, Y., and Shao, X. “Real-time dynamic hybrid testing of structural systems”. In: *13th World Conference on Earthquake Engineering, Vancouver, Canada*. 1644. 2004.
- [22] Riebe, S and Ulbrich, H. “Modelling and online computation of the dynamics of a parallel kinematic with six degrees-of-freedom”. In: *Archive of Applied Mechanics* 72.11-12 (2003), pp. 817–829.
- [23] Riebe, S. “Aktive Schwingungsisolierung und Bahnregelung von Hexapodsystemen”. PhD thesis. Chair of Applied Mechanics, Faculty of Mechanical Engineering, Technical University of Munich, 2005.
- [24] Siciliano, B. and Khatib, O. *Springer handbook of robotics*. Springer, 2016.
- [25] Sygulla, F., Wittmann, R., Seiwald, P., Hildebrandt, A.-C., Wahrmann, D., and Rixen, D. “Hybrid Position/Force Control for Biped Robot Stabilization with Integrated Center of Mass Dynamics”. In: *IEEE RAS International Conference on Humanoid Robots*. 2017.
- [26] Treis, M. “Dynamikmodellierung eines Hexapods”. Semesterarbeit. Chair of Applied Mechanics, Faculty of Mechanical Engineering, Technical University of Munich, 2018.
- [27] Winkler, A. “Sensorgeführte Bewegungen stationärer Roboter”. Habilitation. Technical University Chemnitz, 2014.
- [28] Wurm, S. “Wiederinbetriebnahme und Weiterentwicklung des AM Hexapod-Systems”. Semesterarbeit. Chair of Applied Mechanics, Faculty of Mechanical Engineering, Technical University of Munich, 2011.
- [29] Zeng, G. and Hemami, A. “An overview of robot force control”. In: *Robotica* 15.5 (1997), pp. 473–482.
- [30] Zhong, G., Deng, H., Xin, G., and Wang, H. “Dynamic hybrid control of a hexapod walking robot: Experimental verification”. In: *IEEE Transactions on Industrial Electronics* 63.8 (2016), pp. 5001–5011.

## Disclaimer

I hereby declare that this thesis is entirely the result of my own work except where otherwise indicated. I have only used the resources given in the list of references.

Garching, March 18, 2019

---

(Signature)